Urban Search and Rescue Robot

Group 20

Charlie Perera (1312528)

Jan Specht (1416924)

Thomas de Oliveira (1419972)

Mark Safford (1411064)

Emily Carman (1431487)

Eashana Chotai (1328512)

Bálint Vidos (1309358)

Table of Contents

1.0 Robot Map

Each number corresponds to the section number in the table of contents.

Figure 1 Robotic Map

1.1 RoboCup Competition Tasks

The tasks involved in the RoboCup Rescue League can be divided into three main categories as follows:

- Mobility and Manoeuvrability
    - Traverse over different surfaces.
    - Climb over difficult terrain such as stairs and debris.

- Sensing Capabilities
    - The use of multiple sensors to gather data and decipher information about the robot's environment such as the following:
        - Creating a 2D and/or 3D map of the test environment.
        - Automatically detect things such as QR codes, hazmat labels and fire extinguishers.
        - Automatically detect and highlight motion.
        - Record verbal audio data.
        - Sense CO2 concentration.

- Arm Dexterity
    - Use of a manipulator to move small plastic pipes.
    - Dexterity tasks include:
        - Move, rotate and insert plastic pipes.
        - Open push doors with the arm.
        - Turn door lever handles.
        - Manipulate 2kg wooden blocks.

2.0 Powertrain

2.1 Introduction to Powertrain

The powertrain of the main tracks of the robot consists of two identical powertrain configurations with each one powering one side of the robot's tracks. The powertrain is an area that was highlighted by the previous year's team as an area of potential weakness due to several reasons. Firstly, one of the brackets that holds the motors sheared and therefore upon receiving the robot the powertrain was entirely un-functional. Secondly, one of the drive shafts had bent which subsequently bent the motors' output shafts, therefore the motor was broken and unfixable hence the motor had to be scrapped. Alongside these issues and the fact that there was no evidence of any FEA being conducted on the original powertrain, it was deemed essential for the performance of the robot to investigate this and make improvements accordingly.

2.2 Powertrain Initial Design

First, an assembly of the current parts of the powertrain design was created and FEA simulations were conducted to understand how and why the powertrain of the previous year had failed. The assembly and mesh were created as shown in *Figure 2.*

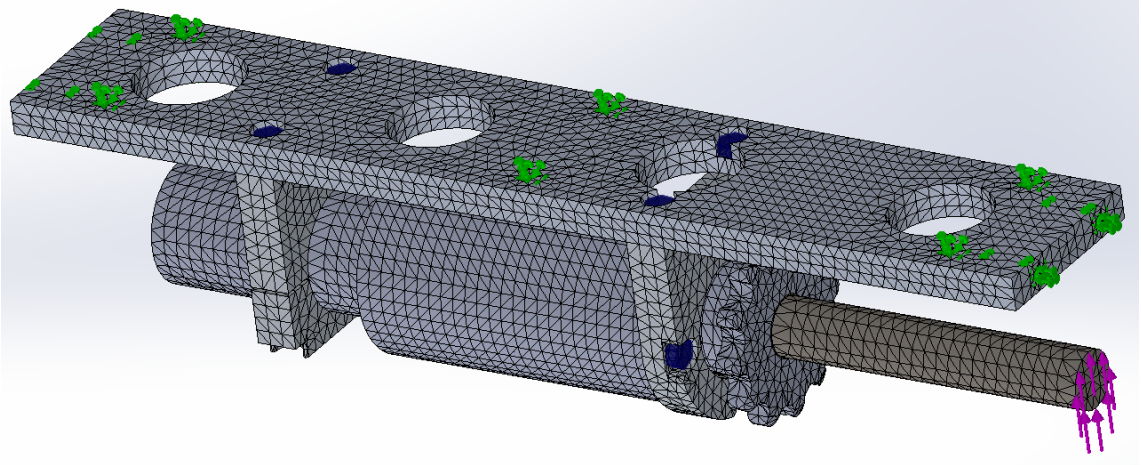

Figure 2: Powertrain assembly mesh, fixtures (green), bolts (blue) and force (purple)

The various bolt holes that would be attached to the chassis have been fixed (shown in green), the connections where the bolts between the parts in the assembly were set to their respective bolt sizes in real life, which was M5 (shown in blue), then a force was applied at the end of the drive shaft to simulate the gear chain pulling on the drive shaft (shown in purple). The force was set at 900N, as this is the highest radial load that the gearbox output shaft attached to the new, replacement motor can take, as stated in the data sheet (Maxon Motors, a, n.d.). This is the most the system would ever be able to support, as anything above this would result in motor

output shaft failure. As this was set at the end of the axle it means that the bending moment is actually be larger than that created by the drive chain in reality, as the chain meshes with the gear further along the shaft, nearer to the motor. This was set as a worst-case scenario.

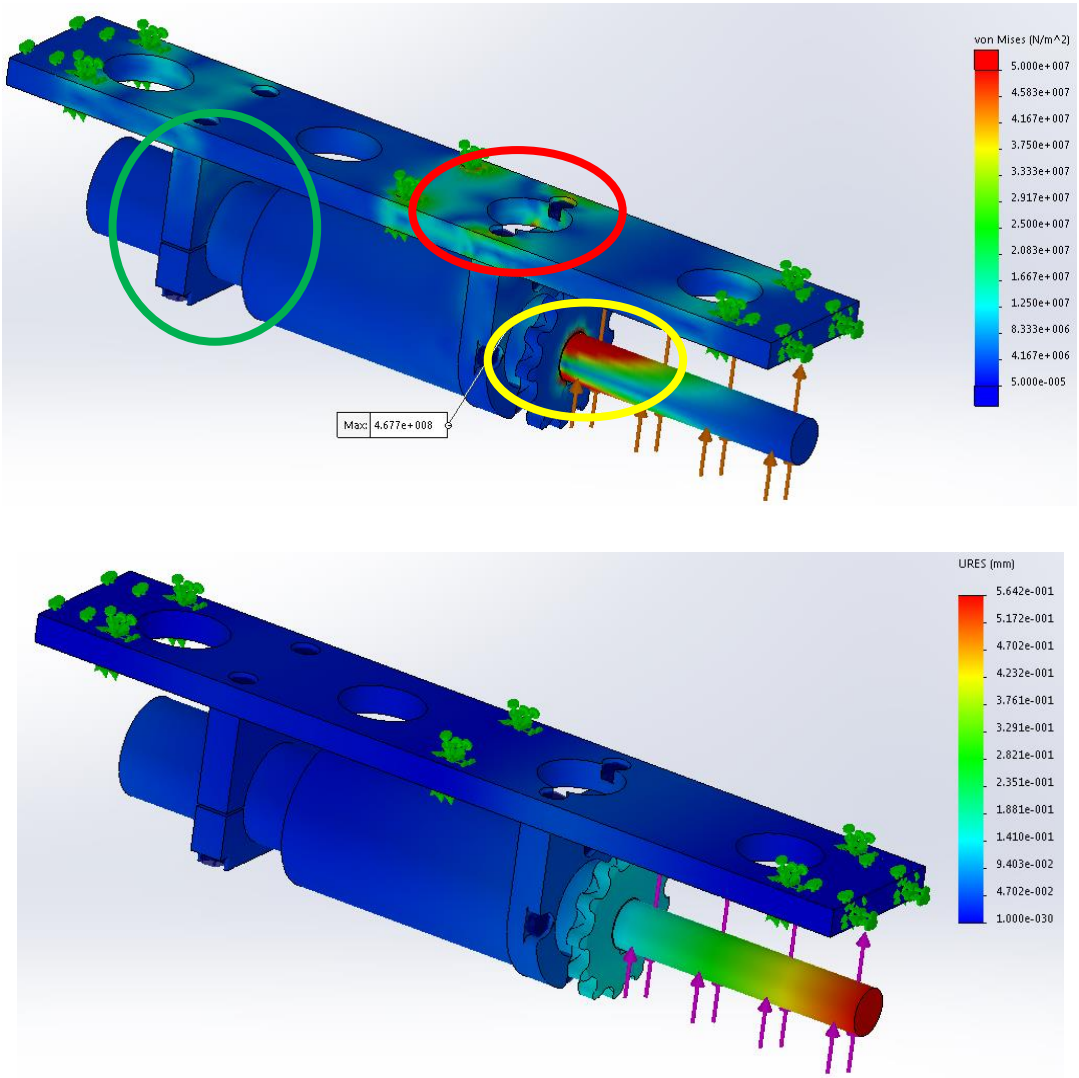

Figure 3: Original powertrain stress plot (top) and displacement plot (bottom)

The simulation was then run, and this resulted in the following stress and displacement plots, with the scale of the stress plot adjusted such that the red highlights not only the peak stress, but also values above 50MPa, in order to show the area experiencing high stress more clearly. Since the powertrain is made up of aluminium and steel parts, displacement is not of particular concern, due to the materials' properties, as can be seen from the respective plot. The maximum displacement is observed to be 0.5mm.. Because of this displacement was not considered further, as far as the powertrain is concerned.

The analysis of the original design resulted in three main areas of concern. Firstly, the area circled in red above appears to be of particular weakness, due to the light-weighted hole being

so close to the bolts that hold the bracket beneath it. This area was redesigned, and the material choice was revised for increased strength. Secondly, the part highlighted in green was problematic last year. Although it does not show up on simulations, this was still of high concern, because last year the bolt holding this part in place sheared, implying the motor was not held in place appropriately and may have caused further damage to the powertrain and the robot as a whole. Finally, the third and most important issue is the stress through the drive shaft and hence stress on the motor's output shaft. This was what caused the drive shaft to bend last year, incurring a cost of £800 that considering project budget needs to be avoided in future.

2.3 Powertrain Redesign

From here the powertrain was redesigned to improve on the issues highlighted above. The first part was the top housing that supports the rest of the powertrain. This was done through an iterative process by first testing the original design shown below and then making changes to find whether these result in stress reduction. This process was repeated until reached an acceptable result was obtained. Changes made include; material modification from aluminium to steel, increasing the thickness enough to reduce stress without increasing weight significantly, optimum positioning of bolt holes and widening of the higher stress part of the component. This lead to reducing the peak stress by an order of magnitude, from 1.12×10^7Pa to 5.45×10^6Pa and the yield strength of the new steel material was also an order of magnitude larger than the original aluminium. This all leads to the final part design having a safety factor of two orders of magnitude, as opposed to zero in the original design.

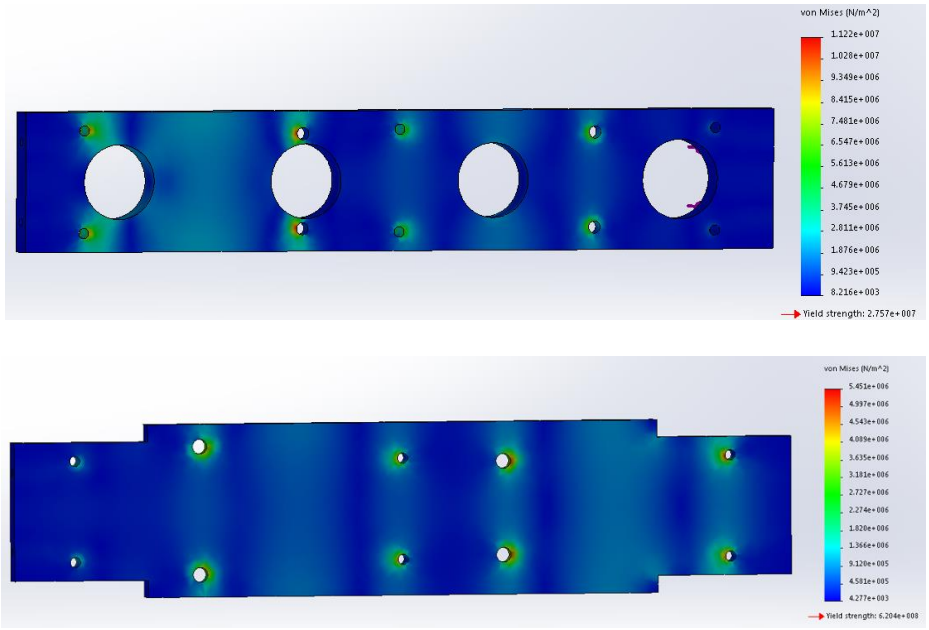

Figure 4: Top housing original (top) and improved (bottom)

The next improvement was made to the two parts that clamp together to hold the motor. For this an assembly was made of the two parts and various iterations were conducted again, this time increasing and adjusting the shape of the part and the positioning of the bolt holes for optimum stress distribution. Also, the clamp had to be redesigned because it needed to be able to hold the replacement motor used instead of the one that was broken last year, the replacement motor was a lot bigger than the old one and therefore it created a challenge to make the new part stronger with less available material space to work with. As can be seen below, the original design had a very high stress concentration on the bottom face, which could have led to fatigue failure over time. This is most likely the reason for part failure. It can be seen how the final design distributes the stress evenly over the entire part and the peak stress has been reduced by over 60% Thus the chance of shear failure has now been reduced.

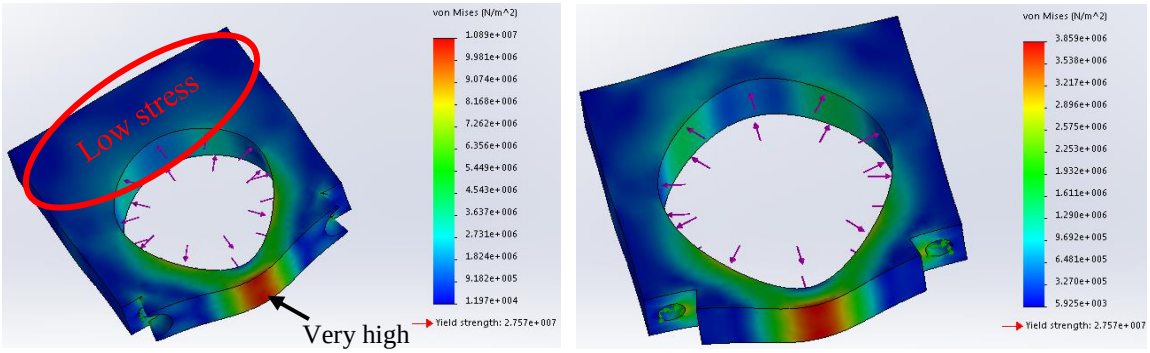

Figure 5: Clamp design original (left) and new (right)

From here small adjustments were made to the components within the whole powertrain assembly and a simulation run to see how this effects the displacements and stresses throughout the entire powertrain. This iterative process was then continued. The main changes made were thickening parts of the powertrain that experienced stress concentrations, to provide a larger area to dissipate stress. The bolt sizes holding the parts of the powertrain together were increased from M5 to M6, because in reality these bolts sheared during testing and therefore a thicker bolt can support more stress prior to shear failure. All these changes were tested to find the best option as shown below, with the same scale used in *Figure 3*, to display the results in a clearer manner. As can be seen from the plot, the stress was throughout the powertrain was reduced greatly, apart from the peak stress concentration on the drive shaft, located next to the motor output shaft.

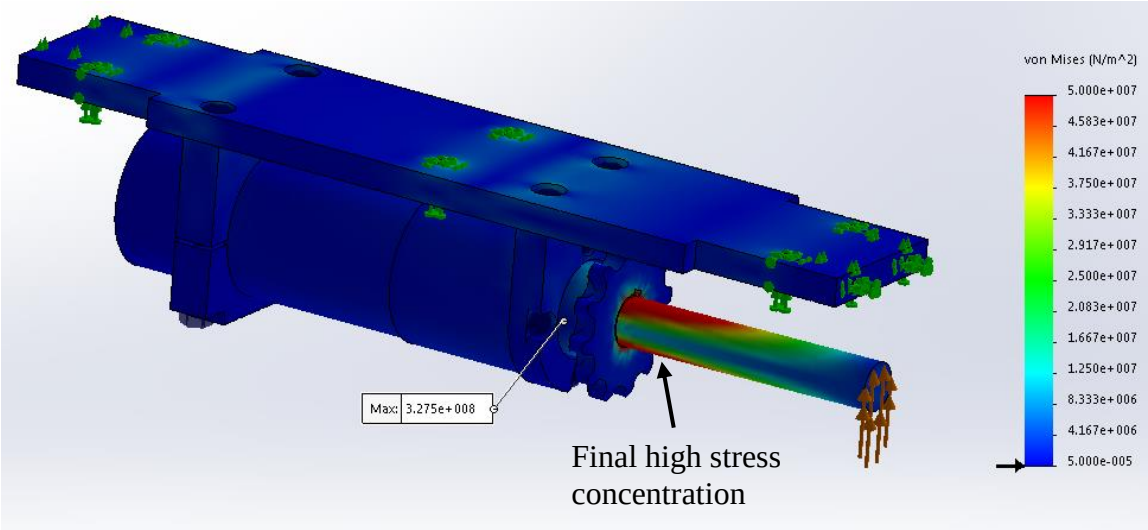

Figure 6: Improved powertrain still with high stress on the drive shaft

The last step was addressing the bending of the drive shaft and motor output shaft due to excessive forces experienced when the robot falls. Since it is not feasible to redesign the system for total avoidance of stresses a novel idea was implemented. A weakness was designed into the drive shaft by means of a small cut around its perimeter, as shown below. this is to direct stress away from the motor. Meaning that the driveshaft would snap off before causing unfixable damage to it. This was deemed as the most practical way of solving this issue. The principle is shown in the image below where, in the iso-clipping, the only area with the highest stresses is the area around the circumference of where the weakness is implemented.

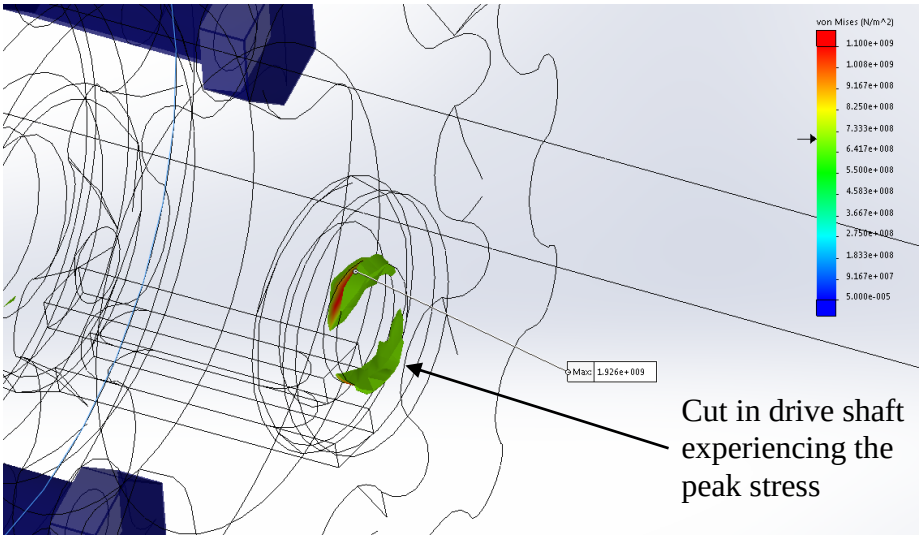

Figure 7: Peak stress concentration around the perimeter of the cut

Various different widths and diameters of cuts were tested at increasing force values from 500N to 900N. Shown below are the results from the selected best cut, which is a 2.5mm cut into the radius of the shaft, leaving a 6mm radius of uncut shaft material and the cut was 1mm wide along the shaft. The plots are iso-clipped to show the higher stress areas of the powertrain only.

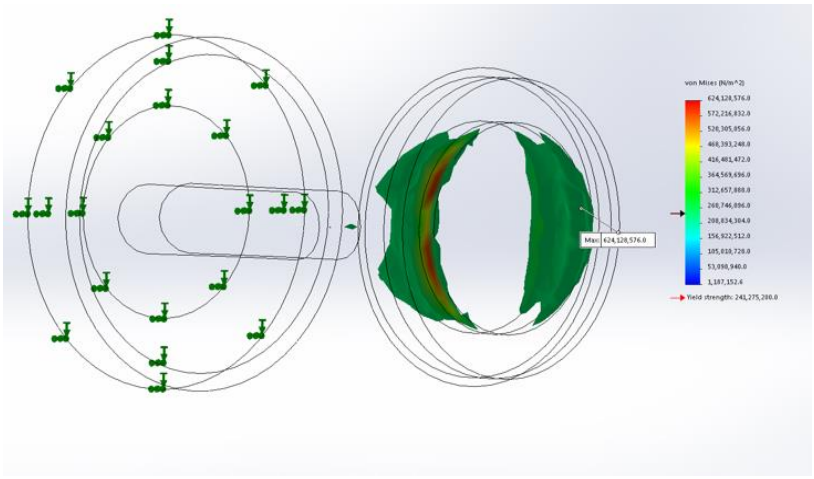

Figure 8: Peak stress iso-clipped plots 500N force

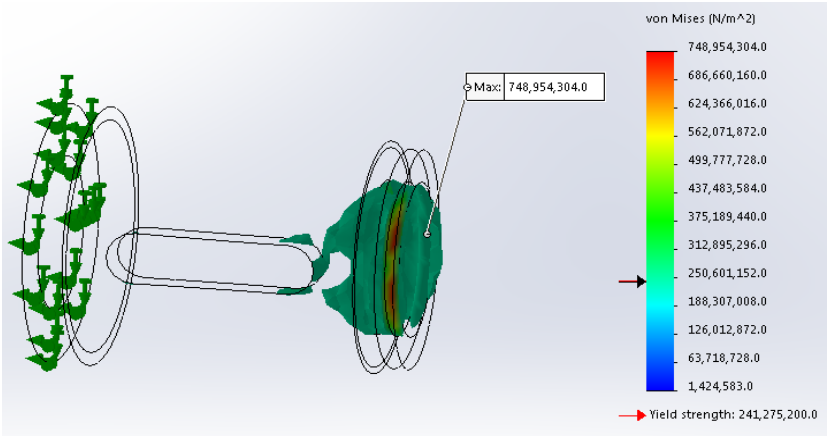

Figure 9: Peak stress iso-clipped plots 600N force

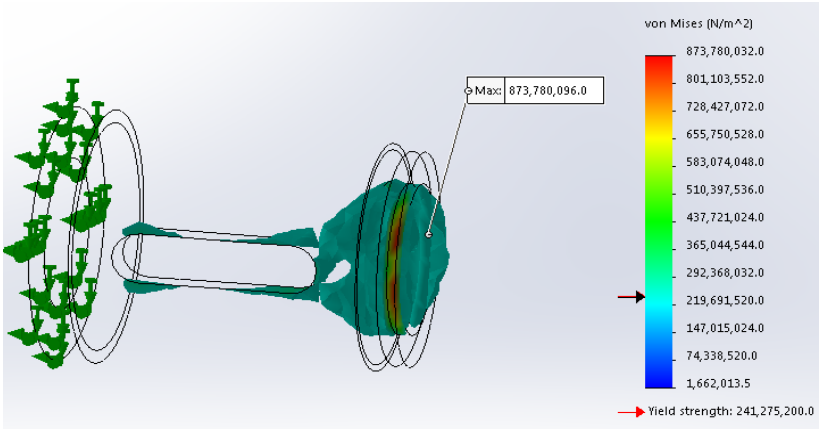

Figure 10: Peak stress iso-clipped plots 700N force

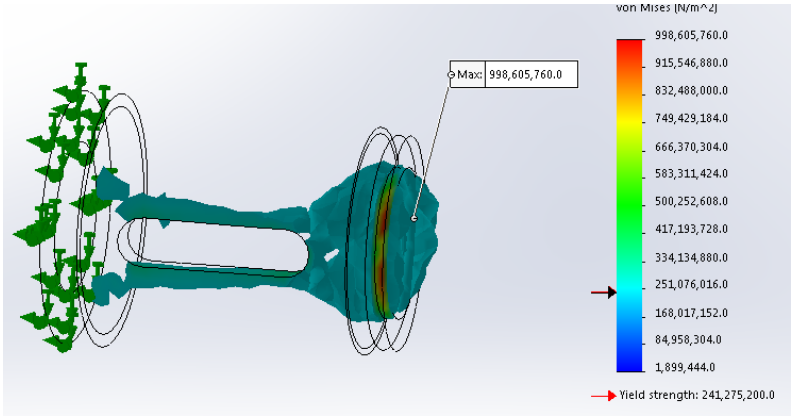

Figure 11: Peak stress iso-clipped plots 800N force

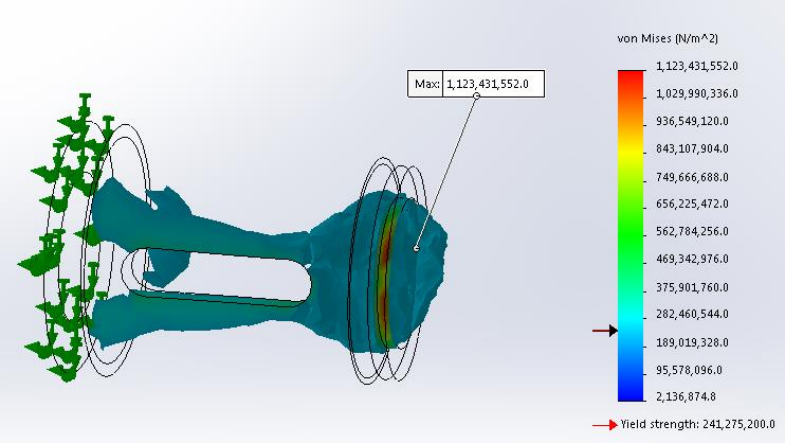

Figure 12: Peak stress iso-clipped plots 900N force

The reason this particular cut was selected was for several reasons. Below 500N several designs would still have stresses above the yield strength of the steel (240MPa), so therefore there would be a chance the shaft would fail under normal operating conditions. The second was , as can be seen from the images, as the force increases, the area of very high stress continues to be located around the weakness only, meaning that the cut in the shaft is operating as desired. Therefore, as from 500N to 900N the peak stress continues to rise but the peak is only experienced around the weakness therefore when the shaft does finally fail it will be where the designed weakness is located and therefore the motor will remain safe. The peak values of stress are so much higher than the yield strength that it would be expected that the shaft should break between 500N to 900N as required.

This model was then tested on the whole assembly, and when the scale is altered such that red is at the peak stress, as shown in *Figure 13*. It can be seen only the area in the cut on the shaft is experiencing stresses anywhere near this peak value, with other areas of the powertrain still being large but much lower than this peak, exactly as desired. A close up of the peak stress concentration also shown on the right below for visualisation.

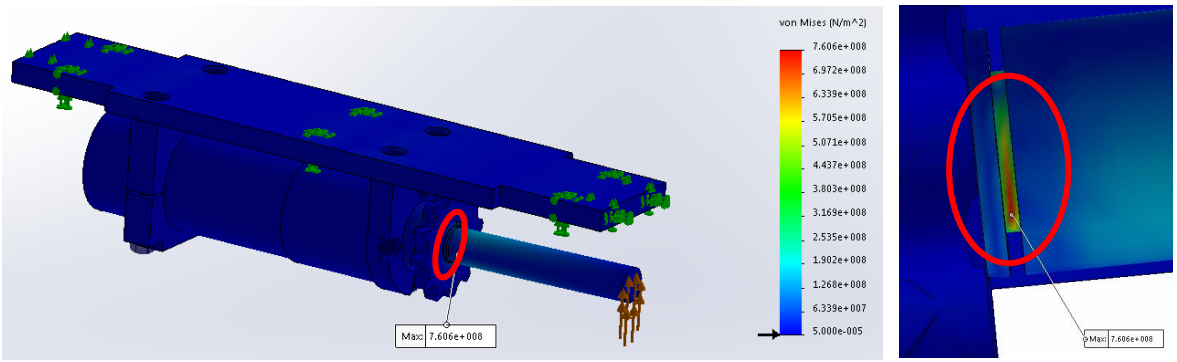

Figure 13: Stress plot of the redesigned powertrain (left) and a close up of the stress concentration (right)

The only final consideration that could cause concern with regards to the breakable shaft concept is the effects of fatigue on the powertrain.

To simulate this a fatigue test was created where a torque of 45Nm, the maximum recommended intermittent torque allowed through the planetary gear set attached to the motor, was set as the applied load. This load was then set such that it would be applied on and off, to simulate the load on the motor stopping and starting in real life. The results of this are shown below.

Firstly, as can be seen from *Figure 14*, the first part to fail from fatigue changes from the where the motor output shaft connects to the drive shaft down to where the weakness has been implemented. This is desired as now if the shaft does break from fatigue the shaft will break well away from the motor and therefore no damage will occur to the motor.

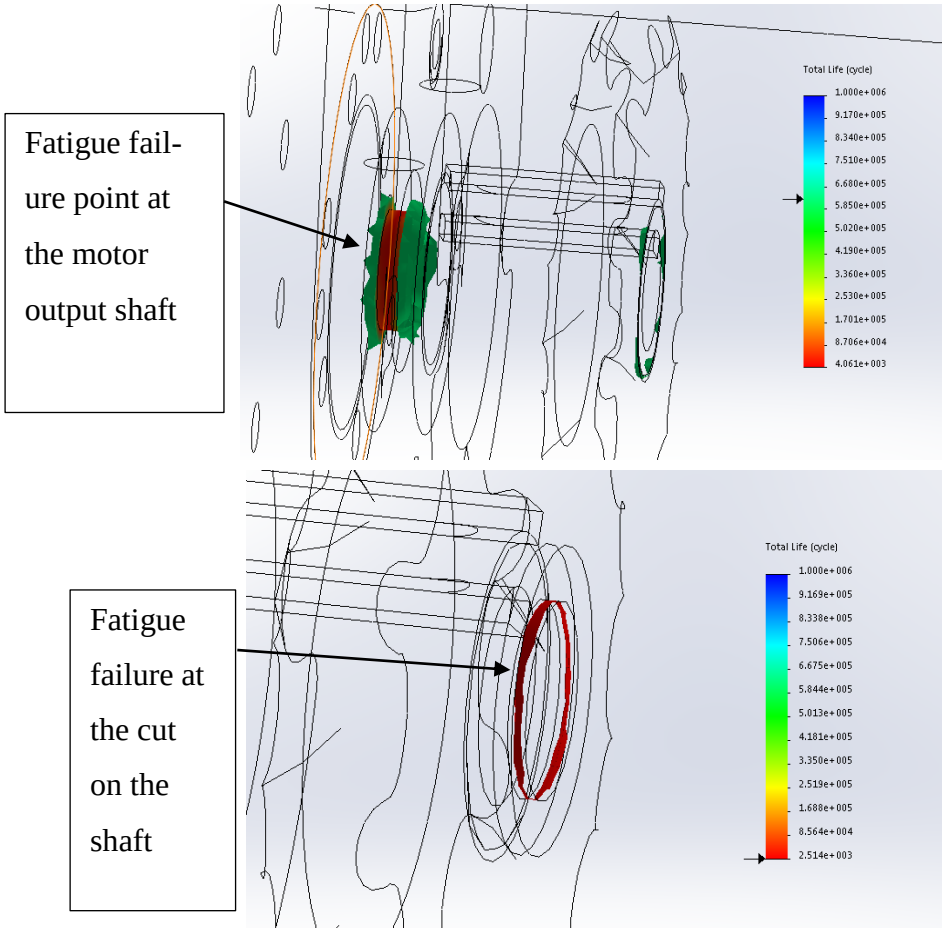

Figure 14: Powertrain fatigue life cycle results old design (top) and new (bottom)

The only downside is that the life cycle has decreased from 4,000 cycles down to 2,500, see *Figure 14*. This is to be expected, because inherently putting a weakness into the shaft will lead

to a shorter life cycle. In this case the reduction is acceptable, because in the life cycle of a search and rescue robot it would be more likely that other parts begin to fail before the 2,500 cycles of this shaft are completed. Therefore, this final study concluded the redesigning process and all the initial concerns raised have been addressed, alongside other general strength improvements to the system. Thus, when implemented into the robot, the powertrain should operate more reliably, without any issues.

Finally, the manufacturing process involved obtaining a quote and then subsequent ordering of the materials required from an outside supplier. From here the parts were milled via computer-controlled machines to their respective rough size using manufacturing machines in the WMG workshop. The machine operations were completed by the technicians working in WMG who are available to help with the production of parts for the student projects. From here some of the parts were hand finished to ensure the optimum fit and surface finish required for usage within robot.

For more detailed dimensions and information please find the technical drawings for the parts of the powertrain in 17.0 Technical Drawings.

3.0 Light Weighting

The robot should be able to compete at the RoboCup Competition where one of the requirements for entrants is a weight limit of 50kg. Currently the robot shell, cladding, tracks and flipper already come to 50kg. With the addition of the robotic arm, batteries and electronics this could potentially rise to 80kg. With the mechanical chassis being the heaviest component the light weighting of this will be looked into. Throughout the simulations 6000 series aluminium will be used, due to its strength and cost efficiency.

3.1 Light Weight Initial Design

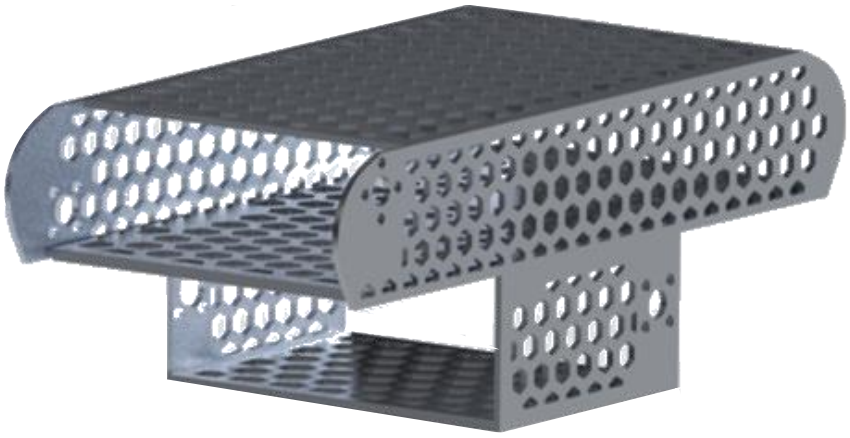

Figure 15. Initial honeycomb shell inherited from the WMR 2016/17 Team

The initial design of the chassis shown in *Figure 15* was inherited from the previous year, the hexagonal shapes were a last-minute light weighting addition.

3.2 Redesign 1 – Thinner Plates

Due to time constraints, the initial plan was to remake the parts using the same design, as these were available and the relevant technicians were already aware of the designs but making each panel thinner. See 17.0 Technical Drawings for detailed technical drawings of these. To assess the viability of this SolidWorks simulations were tested.

The following assumptions were made:

- The maximum compression allowed is 0.02m
- ATLAS weighs approximately 60kg
- All KE is converted to EPE

$$v_{impact}^2 = u^2 + 2as$$

$$v_{impact} = 2.62ms^{-1}$$

$$F = \frac{\frac{1}{2} m\, v^2}{d}$$

$$F = 10296.6\text{N}$$

This gives a maximum force of 10296.6N which is used in these simulations. For these simulations each panel has been halved in thickness, meaning the top and two side panels are 3mm thick and the central and lower shelves 5mm. These two plates were decided to be left thicker, as they will hold the electronics and have the batteries mounted onto.

In the first simulation the body shell is modelled by using rigid pins to connect the assembly together. The force of 10296.6N is loaded onto the base panel, as indicated by the purple arrows in *Figure 16*, and the stress, deformation and strain plots are examined. For ease of comparison between the options made the right-hand side panel will be isolated in the study.

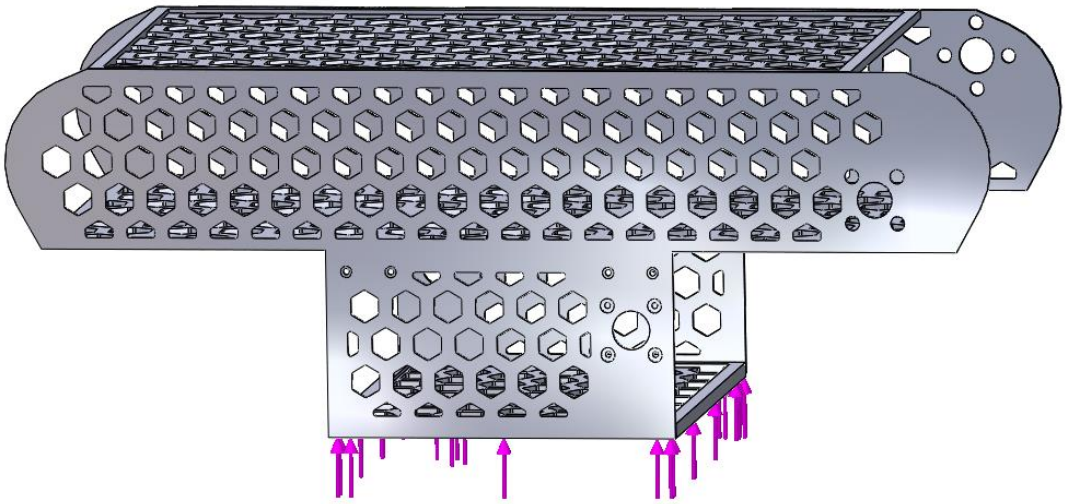

Figure 16. Drop test set up

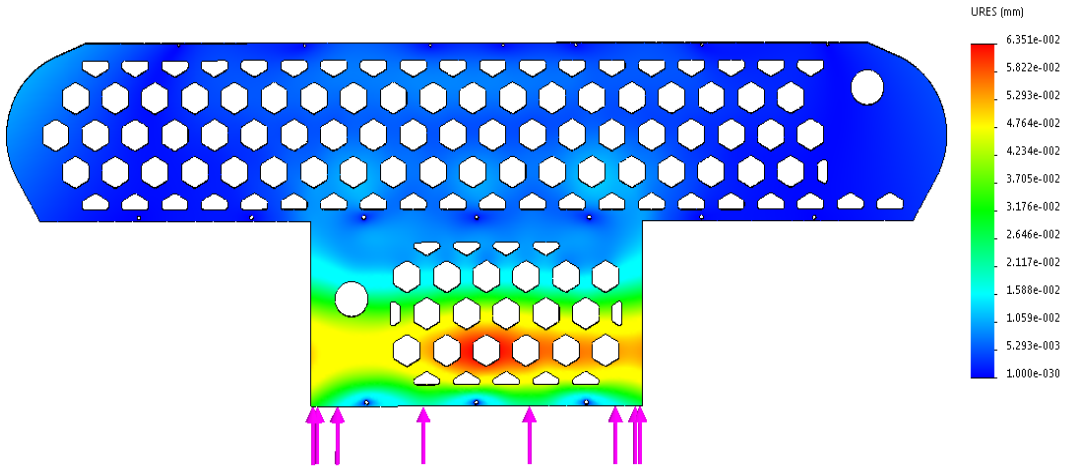

Figure 17. Displacement caused by 0.35m fall

Figure 17 shows the displacement that occurs when the maximum force is applied directly to the bottom plate of the robot. This is representing the robot being dropped or falling from the height of 0.35m. This results in a maximum displacement of 6.351×10^{-4}m which is well within the 0.02m tolerance that has been allowed for in designs.

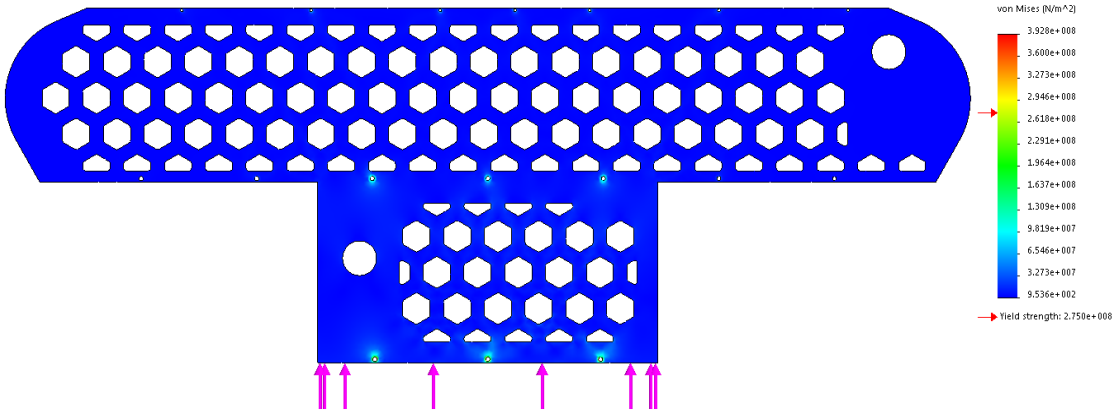

Figure 18. Stress caused by 0.35m fall

Figure 18 and *Figure 19* show the resultant stress on the chassis panel. As these figures show the majority of the panel is well within the tolerances of the aluminium. The highest stress, and that above the yield strength of the material occurs around the holes, but this is to be expected as fixtures incur contact. From these results it can be expected that ATLAS will remain intact after a 0.35m drop.

The second test set up was conducted with the force being applied directly to just the right-hand side to see if the thinner side panels can take the force directly.

Figure 19 shows a peak displacement of 0.028m near the wider curves of the panel, which is above the 0.02m design limit, but in physical testing this displacement should not be as high.

In practice there will be carbon fibre in between the two side panels along the curved face to act as further support therefore this will not be an issue in reality.

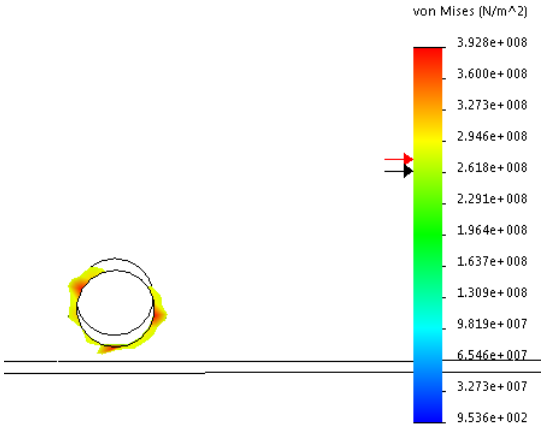

Figure 19. Iso-clipping of stress, showing that above 2.6e08 N/m^2

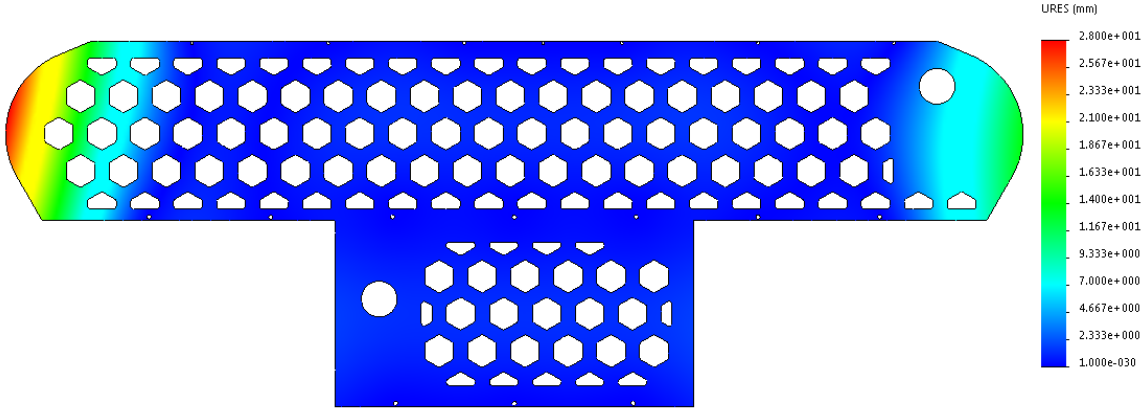

Figure 20. Displacement caused by 10296.6N side impact perpendicular to the panel

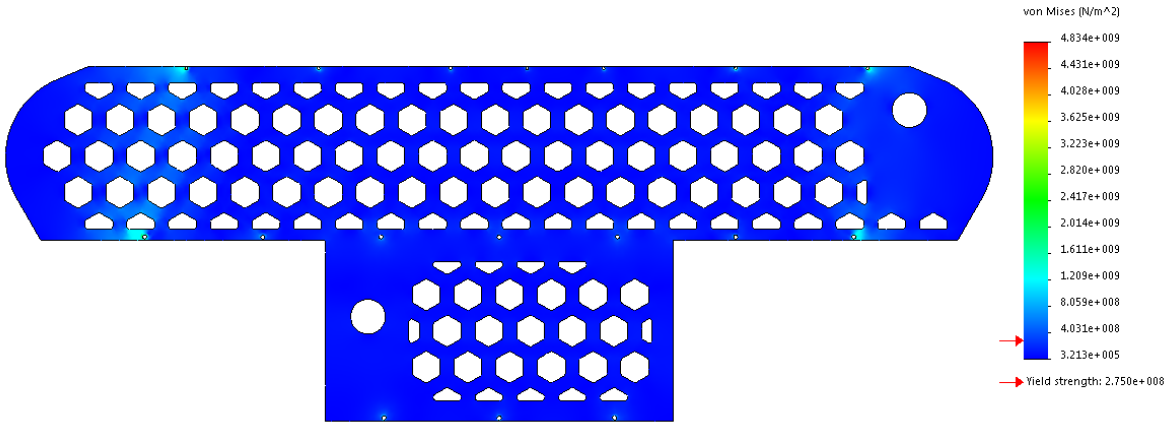

Figure 21. Stress caused by 10296.6N side impact perpendicular to the panel

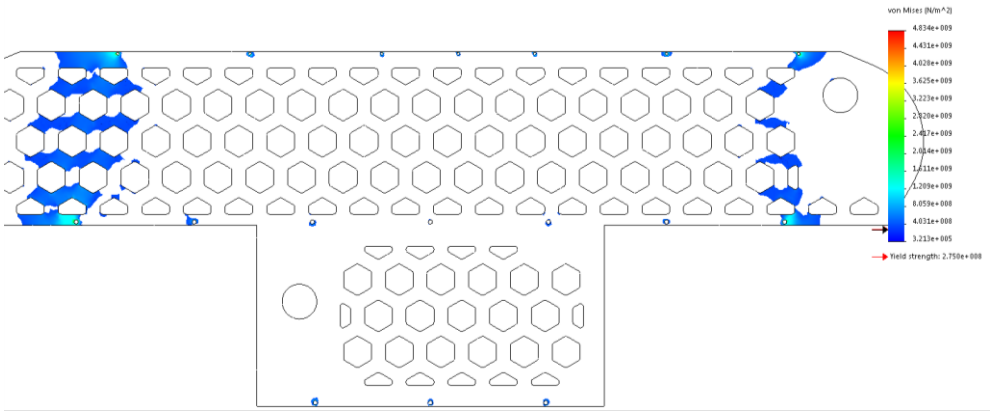

Figure 22. Iso-clipping of all stress above the yield strength

As with the previous results, *Figure 21* and *Figure 22* show the majority of the panel to be well within the materials tolerance, with the sections of high stress being the holes. In this case there are also some major parts of the panel, shown above in light blue, these could be anomalous or due to simulation constraints in fixing the planes together. However due to the pattern running across the sides of the panel it is possible that a crack could form along this and break the two curved sections off.

The final test was conducted to the rear corner of the robot, to simulate the robot falling whilst climbing, this is a likely issue as previous WMR teams have seen this. *Figure 23* shows the SolidWorks set up for this, with the 10296.6N force evenly distributed on the faces indicated by the purple arrows.

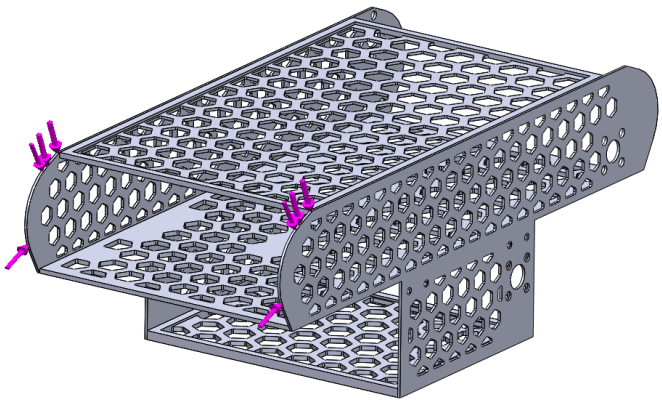

Figure 23. Force on end panel simulating a fall

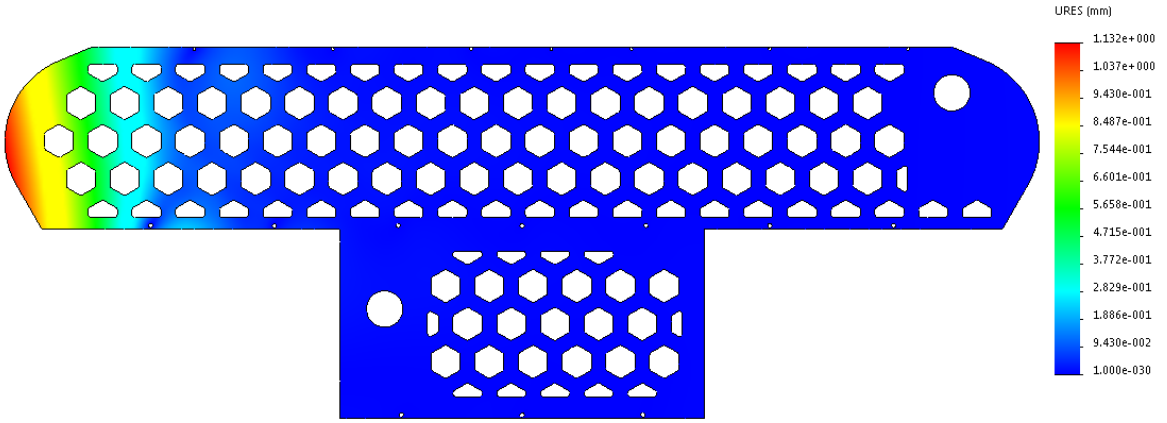

Figure 24. Displacement caused by the robot falling back on itself

The displacement shown in *Figure 24* has a max value of 1.132×10^{-3} m, well within the design limit, and this is concentrated at the back edge of the panel as is expected with the location of the force. In reality this test damaged the robot of the WMR 16/17 team, deforming a motor output shaft and so stopping any further movement of the robot. This simulation suggests it was not to do with the chassis strength, as even half thickness, the deformation is within tolerance.

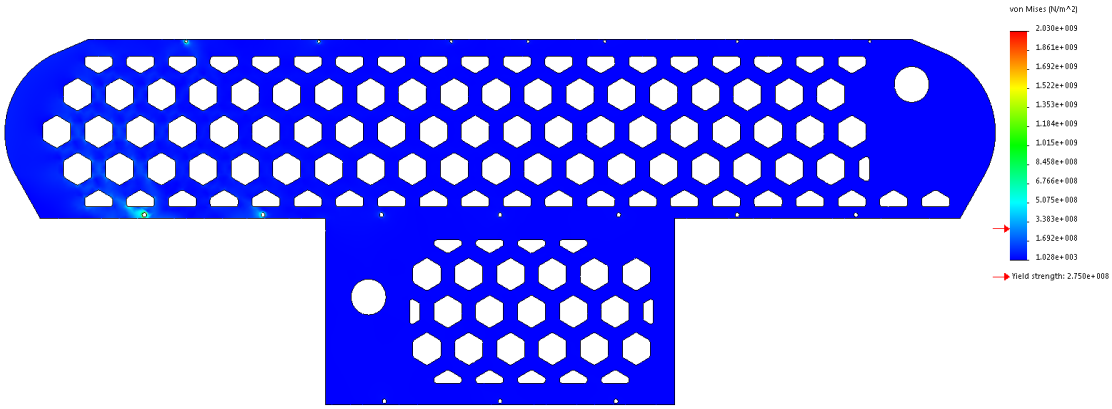

Figure 25. Stress caused by the robot falling back on itself

The stress simulation results shown in *Figure 25* and *Figure 26* again show the majority of the plate to be well below the limit and the points of interest being the holes. The lower left edge of the plate has the most stress around the holes, this is logical as it is where the plate will rotate around when the force is loaded on.

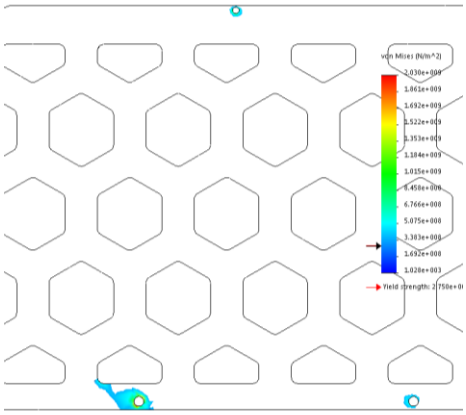

Figure 26. Iso-clipping showing stress above the yield strength

3.3 Redesign 2 – Larger Hexagonal Cut-Outs:

Figure 27 Larger hexagonal cut-out chassis assembly

Figure 27 shows a render of the SolidWorks assembly for this redesigned chassis, for further detailed technical drawings see 17.0 Technical Drawings. As with Redesign 1 the right hand side panel will be isolated for analysis and comparison, using the same input conditions.

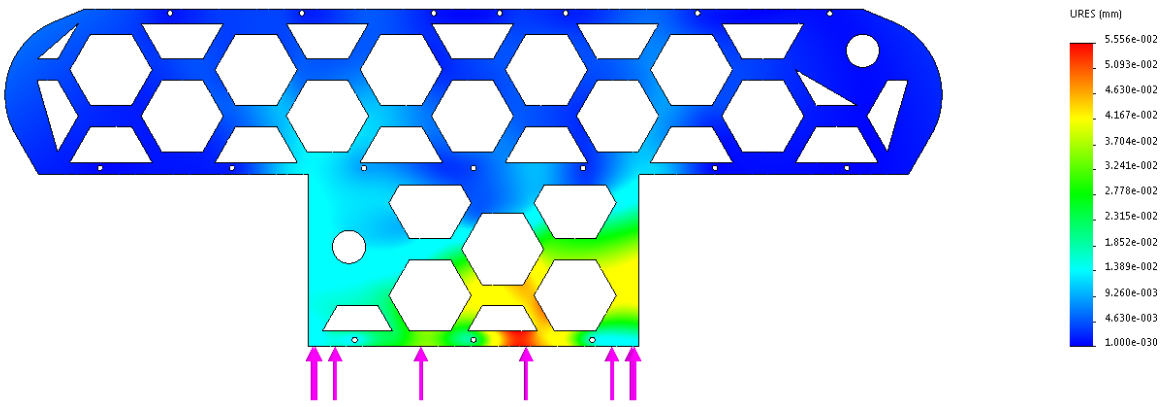

Figure 28. Displacement caused by the robot falling 0.35m onto base

Firstly, the drop test, from visual comparison with *Figure 28*, the spread of the higher displacements is smaller. The peak displacement in *Figure 28* is 5.556×10^{-2}m, 0.795×10^{-2}m less than in Redesign 1. However, the point of this displacement has moved lower down, towards the base of the chassis, this could cause more worries if the magnitude was any higher. In this case the peak is still well below the design limit and will cause no issues during the drop test.

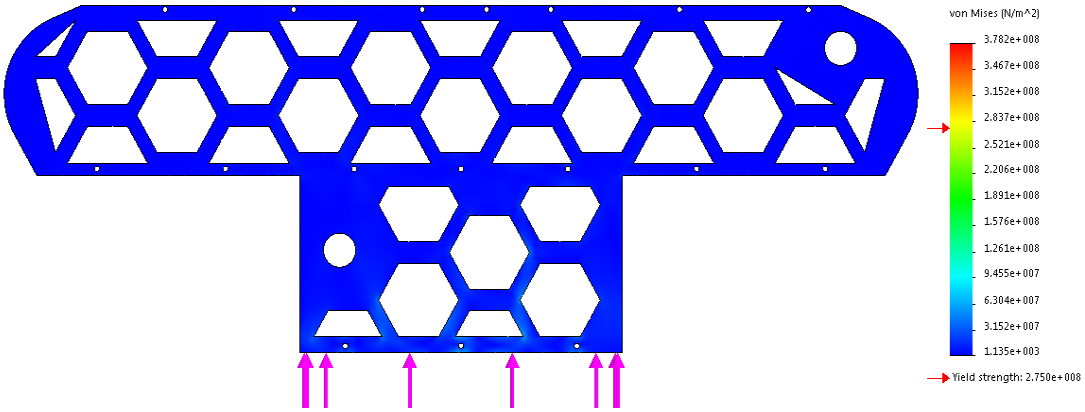

Figure 29. Stress caused by the robot falling 0.35m onto base

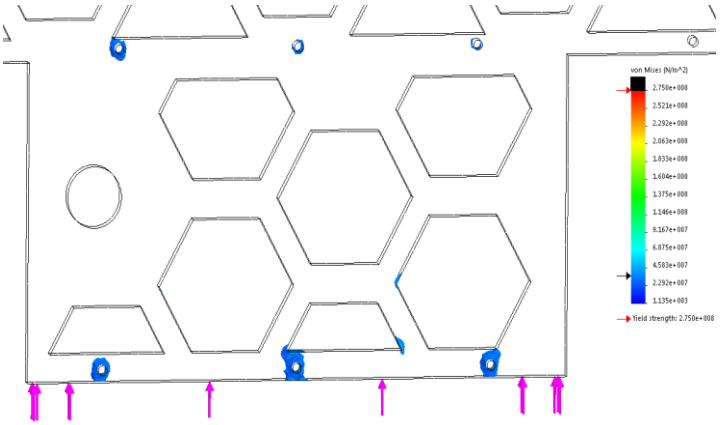

Figure 30. Iso-clipping showing areas of highest stress from drop test

Figure 29 and *Figure 30* show again that just the holes are of possible concern due to higher stresses, and in this case only a very small section of the middle base hole is above the yield strength.

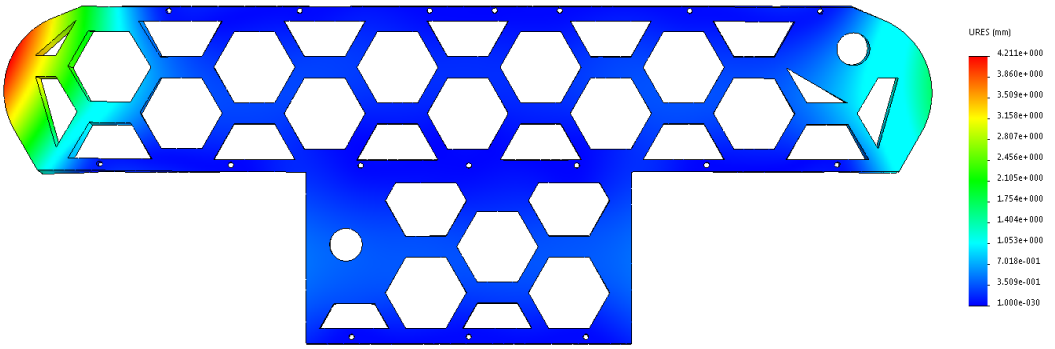

Figure 31. Displacement caused by 10296.6N force perpendicular to the panel

Secondly on the larger hexagonal plates, looking at the results caused by a perpendicular force to the panel. *Figure 31* shows the displacement caused by this force, with a maximum of 4.211×10^{-3}m this is far lower than the 28×10^{-3}m shown in *Figure 32* by the thinner design. The areas affected are the same, but again in reality these results should be lower due to the additional structural reinforcement the carbon fibre will add.

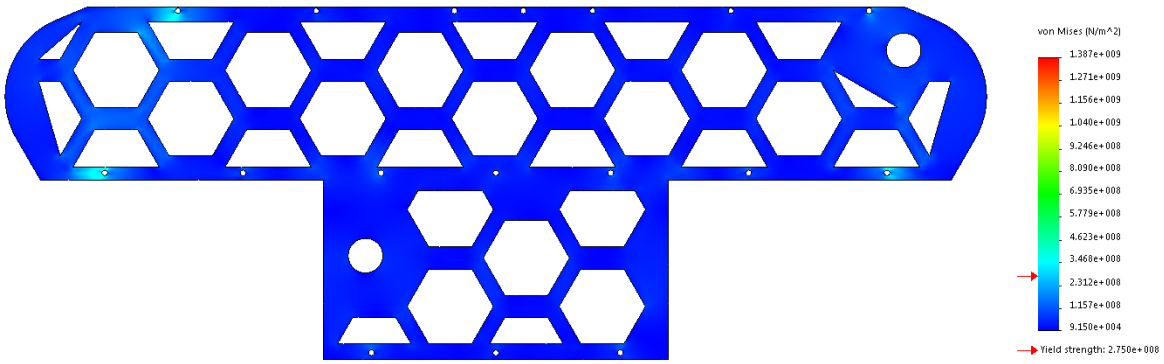

Figure 32. Stress caused by 10296.6N force perpendicular to the panel

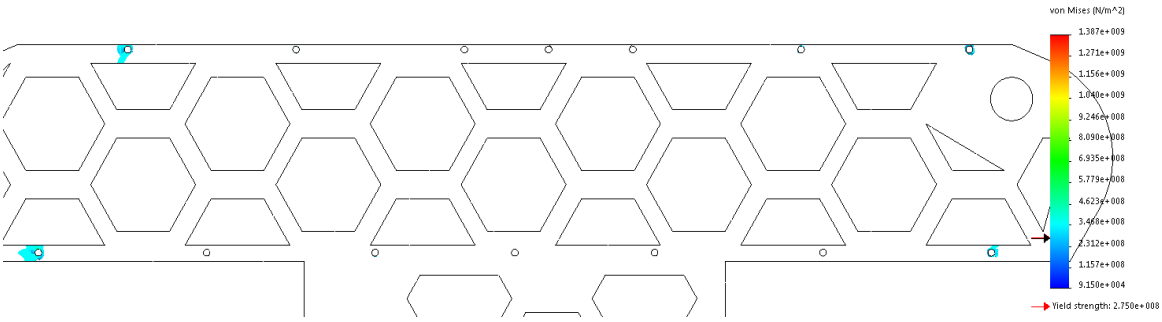

Figure 33. Iso-clipping showing stress above the yield strength for side impact

Figure 32 and *Figure 33* show the stress again continuing that almost all the panel is well below the tolerance. Comparing this to *Figure 22* shows the improvements that Redesign 2 has made. Above it can be seen that there is very little above the yield strength, showing this to be a far superior design to withstand any side impact.

Lastly the instance of the robot falling back and landing on its corner is considered. *Figure 34* shows a maximum 0.5871×10^{-3}m, again well within the design tolerance.

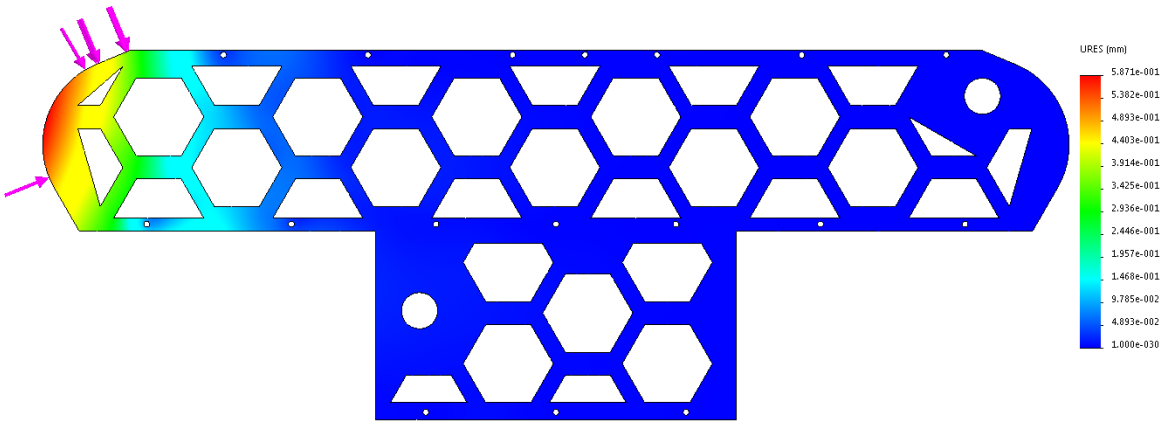

Figure 34. Displacement caused by the robot falling on its back corner

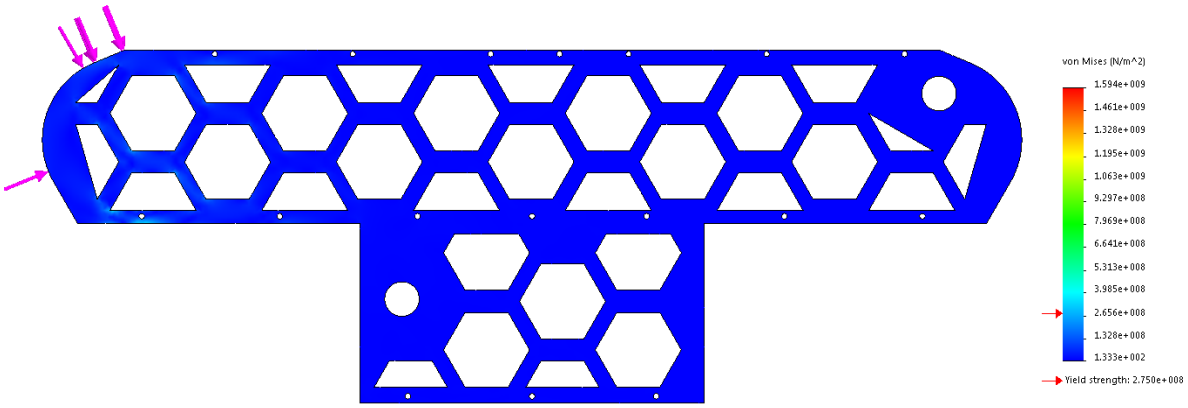

Figure 35. Stress caused by the robot falling on its back corner

Figure 35 and *Figure 36* show the areas of stress on the panel, as with the other simulations it is only the holes that cause potential issue. In this case they are on the side that will be put into compression as the robot lands on the corner. The peak stress is 1.594×10^9 Pa compared to 2.030×10^9 Pa in *Figure 25*, showing once again that, although small, improvements have been made on each simulation.

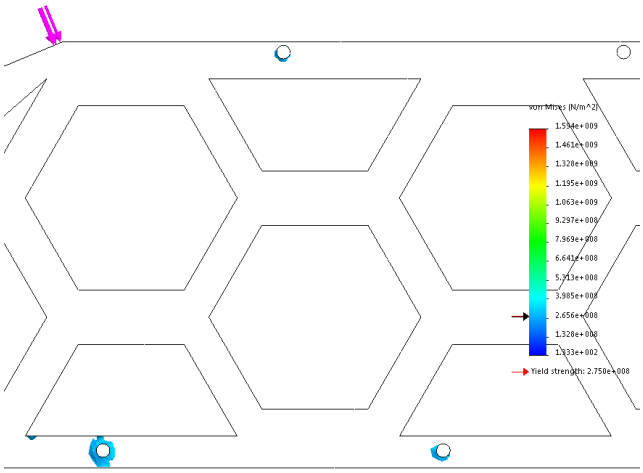

Figure 36. Iso-clipping showing areas stress above yield strength

3.4 Direct Comparison of Data

		Redesign 1	Redesign 2
Drop Test	**Max Disp (mm)**	0.06351	0.05556
	Max Stress (N/m^2)	3.928×10^9	3.782×10^9
Perpendicular Force	**Max Disp (mm)**	28	4.211
	Max Stress (N/m^2)	4.834×10^9	1.387×10^9
Back Fall	**Max Disp (mm)**	1.132	0.5871
	Max Stress (N/m^2)	2.030×10^9	1.594×10^9

Table 1 Table comparing maximum values for each redesign

From *Table 1* it can be seen that Redesign 2 has lower values for each simulation, notably in the perpendicular side force test with sevenfold less displacement and fourfold less stress. This test is also the only case, in Redesign 1, which fails to meet the design criteria of 0.2m for the maximum displacement.

3.5 Redesign Option 3 – Carbon Fibre Shell and Cladding Merged

After a successful meeting with GRP for sponsorship of the carbon fibre for cladding on 7th February the possibility was suggested by Dr Peter Wilson that the shell and cladding could be combined and made out of reinforced recycled carbon fibre. Due to the timing and complexity of this meeting in the projects lifecycle this will not be feasible this year but is something that can be done in future years.

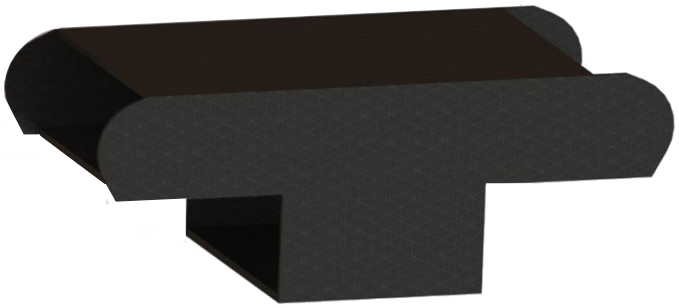

Figure 37. Render of a fully carbon fibre chassis

The combination of the two to be made from carbon fibre would not only leave a sleek exterior, as shown in *Figure 37*, but also make a huge weight saving for the robot, this will combine the research themes of both High Value Manufacturing (HVM) Catapult and GRP, two of the projects current sponsors. It will also bring innovation and new technology to the robot.

The manufacture of this will be done in house by members of the team, and Dr Wilson in the GRP laboratories, allowing for complete quality control of the manufactured part.

4.0 Battery Mounting Implementation

4.1 Battery Mounting Concept 1

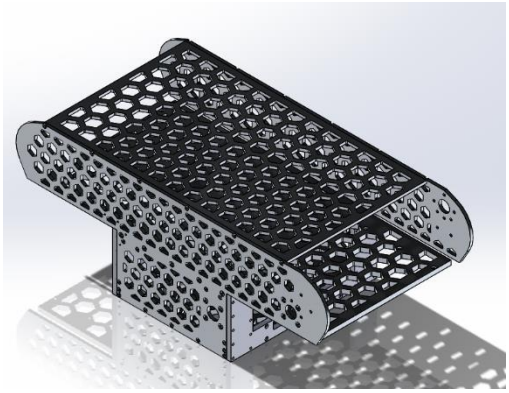

Figure 38 Original assembled chassis design.

It was felt that change would need to be made to original aluminium chassis shown in *Figure 38* in order to allow the batteries to be mounted, as well as gain easy access to the electronics. There was also a significant waste of space as there was no component in top section previously. This will help lower the COG as batteries were originally to be mounted in the top of robot, as seen in *Figure 39.*

A design possibility was to modify cladding and chassis to allow batteries to be placed in the bottom section without moving flipper motors. This would involve mounting batteries as shown in *Figure 40*, which would require the chassis to be modified to allow access to the batteries. This modification is shown in *Figure 41*.

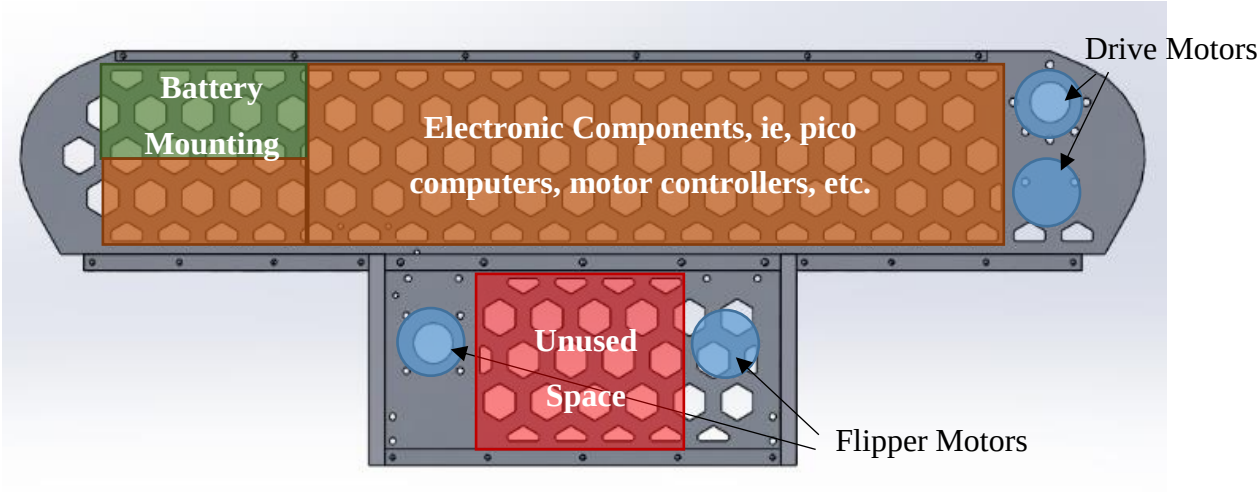

Figure 39 Original intention for mounting of components within robot.

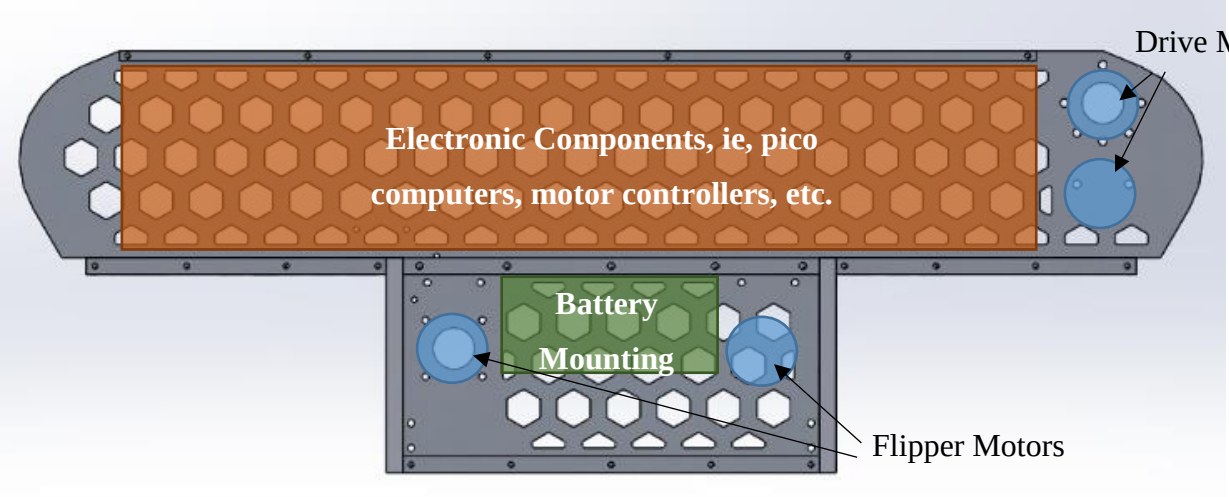

Figure 40 Redesigned configuration of components.

The main issue with this idea is the potential difficulty of removing batteries in the case of a collision. However, it was deemed that this was a risk that would also occur when mounting batteries at rear of robot, which could potentially be a worse scenario due to the inability to remove both batteries rather than potentially just one. It was deemed that the advantage of being able to use more space and improve the handling characteristics of the robot outweigh any potential risks involved with this.

Furthermore, the cladding will be designed so that access to the battery will be easy and will not be hindered by any parts in order to allow for batteries to be removed as quickly as possible.

Items to check:

- Ability of Middle Plate to deal with mounting of batteries under worst case scenario (drop or fall).
- Ability of side panels now containing holes to accommodate battery insertion and extraction to deal with worst case scenario loads (drop or fall).
- Can parts be modified if initial idea fails so that batteries can be accommodated in this way?

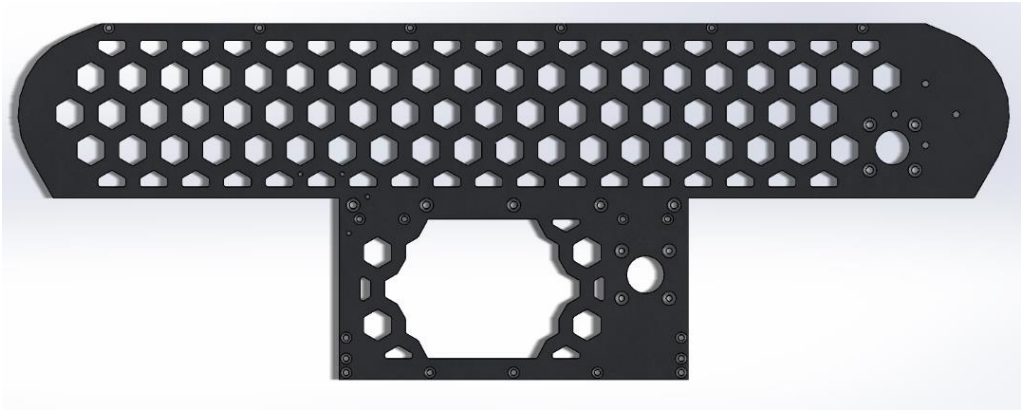

Figure 41 Cut out design, hole cut to maximise amount of remaining material and retain the hexagonal shape to ensure strength of component

4.2 FEA on Side Panel - Viability

Fixtures and forces considered:

- Fixed geometry connection with connection to top middle and bottom plate.
- Force from externally mounted drive wheel, track and mounting, weight approx. 500g.
- Force from internally mounted drive motor and 1:1 gear connection, weight approx. 3kg.
- Force from internally mounted flipper motor bearing, potential to have weight approx. 500g.

Under resting load conditions, both designs have similar characteristics, both showing maximum stresses of around 6% the yield strength of the 6000 series aluminium alloy chosen (6061).

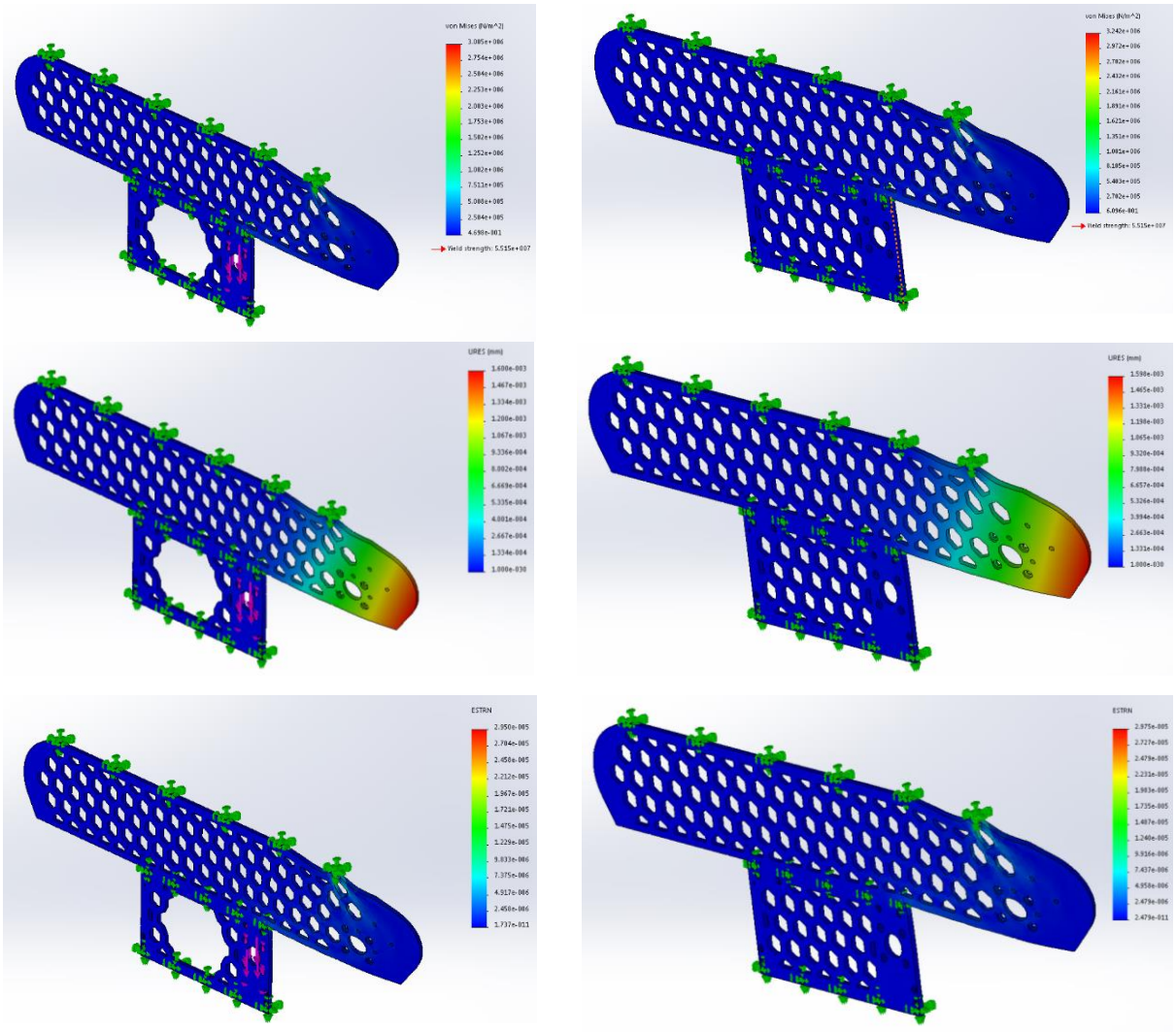

Figure 42 Comparison of stress (top pair), displacement (middle pair) and strain (bottom pair) for cut out design (all left) and original design (all right) under regular non-crash

Test shows that modified design is very similar to original, conducting further tests to determine whether further modifications need to be made in order to withstand crash conditions. All results in *Figure 42*.

4.3 Crash Scenarios

There is a need to test some worst case crash scenarios, with Atlas being able to survive a fall from 0.35m, while landing in any orientation, such as:

- Robot falling on front and rear end.
- Robot falling on its top
- Robot landing on bottom

All while containing the same loads from parts.

Using simple mechanical theory and ignoring air resistance, the velocity at impact can be calculated as follows:

$$v_{impact}^2 = u^2 + 2as \tag{1}$$

$$v_{impact} = \sqrt{0^2 + 2 * 9.81 * 0.35}$$

$$v_{impact} = 2.62ms^{-1}$$

Assumptions made were:

- The maximum compression allowed is 0.02m
- Atlas weighs approximately 60kg with all parts loaded.
- All KE is converted to Elastic Potential Energy

This gives:

$$F = \frac{Net\ work}{Compression\ distance} = \frac{\frac{1}{2} m\ v^2}{d} \tag{2}$$

$$F = \frac{\frac{1}{2} * 60 * 2.62^2}{0.02}$$

$$F = 10296.6\text{N}$$

For this, an assembly was made of one side of the robot, connected to the three horizontal plates by a rigid pin connector, while all appropriate loads were applied to the correct points, such as the mounting for the battery and two flipper motors onto the middle plate, drive motor on the side panel as before and the mass of the bearing acting on the side panel. The fixtures for the free ends of the middle panels are modelled as pins also. This will likely give a higher value for peak stress than the true value. All of the start conditions are shown in *Figure 43*.

4.4 Testing of Battery Mounting

4.4.1 Test 1

Impact test on corner, set up time dependant simulation with sudden spike of force acting on component in order to simulate impact. First test is shown in *Figure 43*, on rear end, to simulate landing on the end where the drive motors are mounted. Unfortunately, was not able to simulate contact with top, middle and base plates due to time and computing constraints, so simulated as fixed hinges, which will lead to higher forces than will be the actual case, due to the parts inability to flex along with the entire rest of the frame.

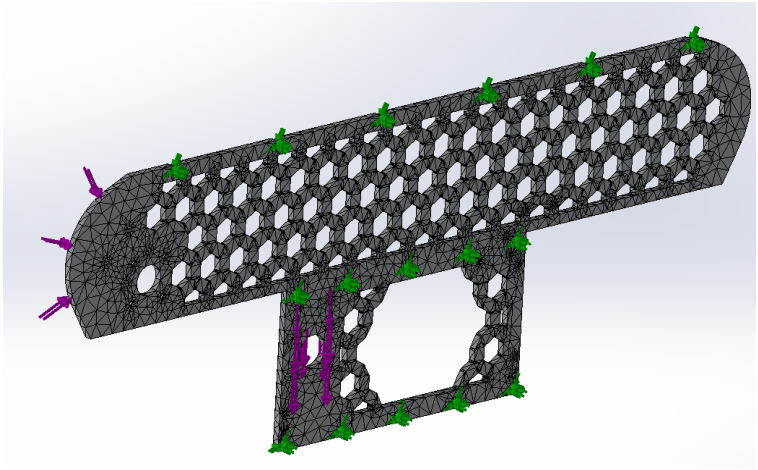

Figure 43 Mesh, fixings (green) and loads (purple) for redesigned part during crash test

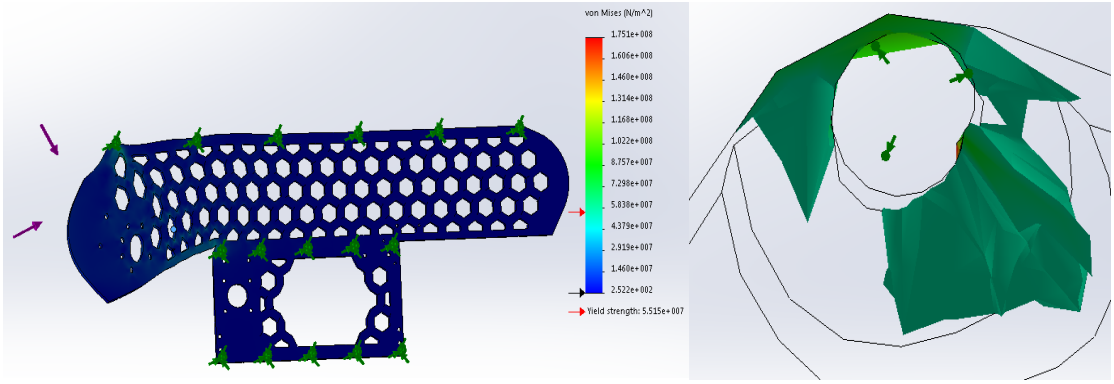

Figure 44 Deformed stress plot (left) and concentration around top left hole (right) for left side impact.

Figure 44 shows the simulation on the rear end of the part. It can be seen that all stress above yield is situated around closest the hole connection to the force. In reality this stress would not be as high as stated and as can be seen, the majority of the issue is at a very small point, making it seem unreliable. It can be deemed that Atlas is still likely to be able to survive a fall of this

magnitude and be able to be redeployed with no repairs required. As can be seen, the vast majority of the part is blue, indicating very small stress values around the majority of the part.

In any case, increasing the size of the holes will reduce the stresses and mean that stronger bolts can be used in order to ensure the parts do not shear apart during a fall.

On the front end results are similar as shown in *Figure 45*, although, some minor reinforcement is required on some of the hexagonal cut-outs around the force in order to reduce the chances of stress failure. The same issues with screw placement are also seen.

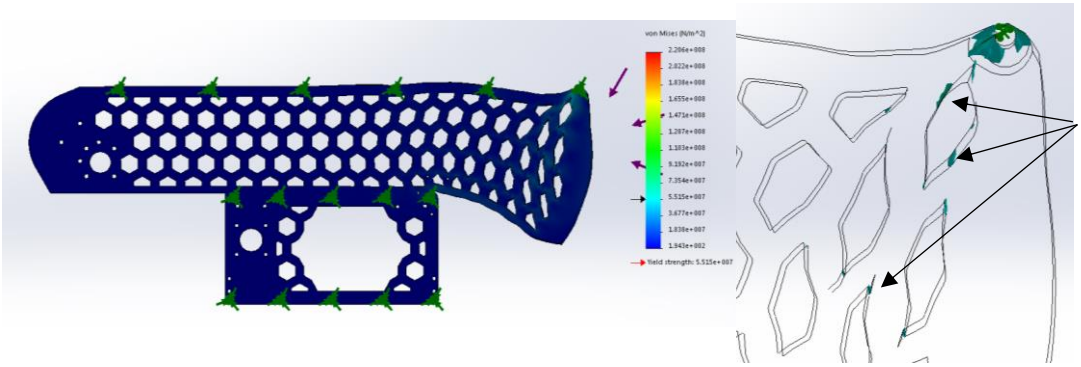

Figure 45 Deformed stress plot (left) and stress concentrations around top right hole for right side impact.

4.4.2 Test 2

A similar result is seen in the test on the top of the part *Figure 46*, with the vast majority of stress above the yield strength seen on the inside of the holes, an area around the holes, in very small concentrations, leading us to believe that they are anomalous, and the result seen in the vast majority of the part, in which there is very little stress is likely to be a more realistic case.

Again, increasing the hole size will reduce the stress and decrease the chance of the parts shearing. It can be noted that the hexagonal structure seems to cope well with the load applied to its top edge and the main body of the side panel sees little stress despite large deflection values, showing that it is good design for absorbing the impact of a crash.

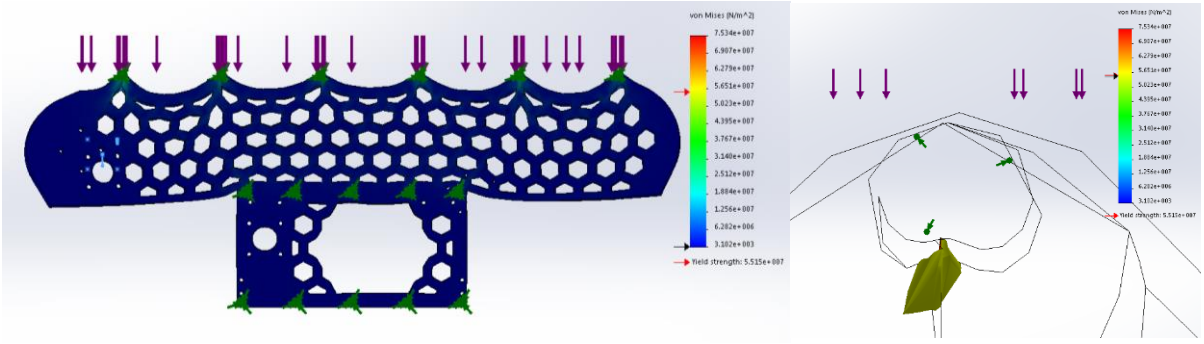

Figure 46 Deformed stress plot (left) and concentration around connecting hole (right) for top crash test.

4.4.3 Test 3

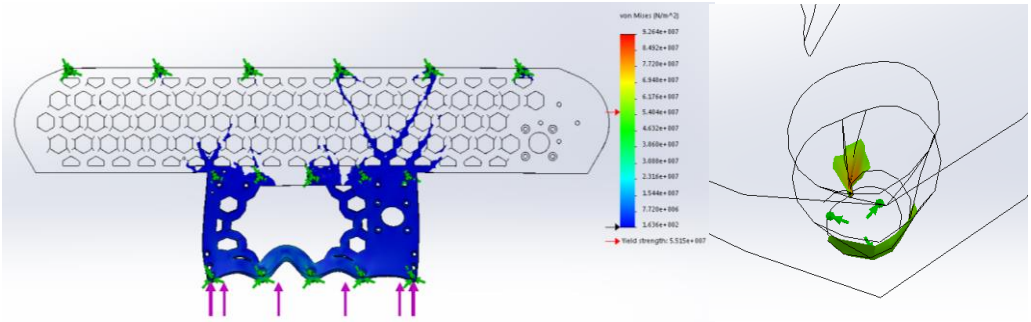

Figure 47 Deformed stress plot (left) and concentration around central hole (right) for bottom impact test. Clear area in right plot indicates no extra stress outside regular conditions.

Figure 47 shows the drop test acting on the bottom of the side plate. As with other designs, the stress concentrations are around the screwed connection to other plates. There is no stress acting on much of the top half of the panel, while the majority of the bottom part sees no major stress concentrations.

4.5 Alterations

Since the issue of strain arising in holes occurs a lot within this design, it makes sense to think of alternative solutions to the problem, in order to reduce the effect that the excessive strain would have.

Using welds to link the top plate and bottom plate to the two side panels will improve the connection in the sense that it will reduce the stress concentrations caused by the screwed connections and will likely be stronger than using these screwed connections due to the fact that the weld would run along the entire length of the connection and any force acting on one part would be distributed along the entire length of the connection, as opposed to simply the locations in which the screws are placed.

Overall however, Can be confident that the chassis will survive a 35 cm fall with no modifications once the entrance for the battery is implemented with no other modifications required beyond removing the area for the battery mounting.

4.6 Battery Housing and Mounting

The batteries are to be placed in a 3D printed housing which will allow it to be mounted in the robot and also to allow rapid deployment and removal if required through the use of a hanging cage mounted to the bottom of the middle plate within the robot. *Figure 48* shows the battery housing, battery cage, and assembled system, without any of the attachments such as gripping handle, battery wiring boards and battery connection points.

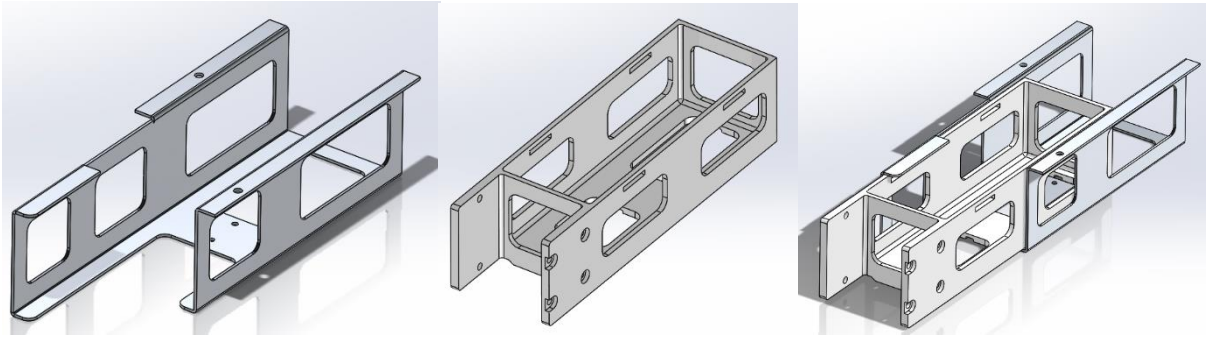

Figure 48 Left: mounting cage, middle: 3D printed battery housing and right: assembled

The battery mounting and cages were already available in the workshop. On the bottom of each is a connection that allows the power supply from the battery to be quickly hooked up and disconnected from the robots electrical systems. The battery itself is wired into a board that provides a link the connection. The 3D printed part also contains a grab handle in order to easily remove the part.

In order to test whether the aluminium could be replaced with 3D printed material if required, they were compared with a load of 2 kg to simulate the battery and all other mounted parts and extra in order to give a safety margin. This comparison is shown in *Figure 49*.

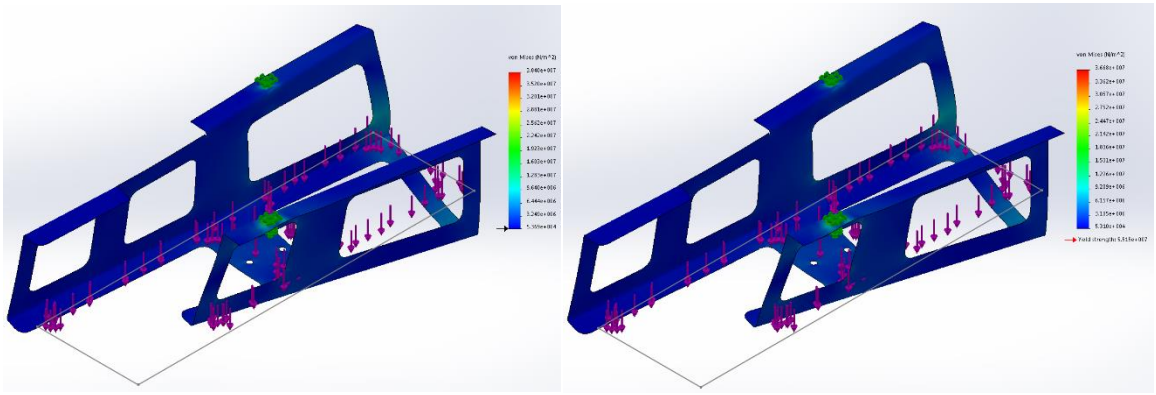

Figure 49 Left: ABS cage, Yield Strength 3 x107MPa, Right: Aluminium Cage, Yield Strength 5.515 x107MPa

As can be seen, the ABS cage sees a similar level of stress to the aluminium. However, the difference in yield stress points to ABS design being likely to not be strong enough to hold the load of the battery. The concentrations area gain around the connection holes indicating that the addition of new mounting holes would improve the parts ability to tolerate the stress. However, for the time being it is believed to be best to stick with the aluminium parts, although in future this could be a design consideration that could be looked at.

4.7 Manufacture

Once all designs were complete, the manufacture was discussed with the technicians. Since this is a modification to an existing part, it was decided to simply mill out the required material and then hand finish in order to remove the danger of cuts from any poorly milled material. As well as this, new holes are to be drilled into the central plate inside the robot, in order to allow for the mounting of the batteries themselves.

4.8 Recommendations and Future Possibilities

On the whole, welding the plates together would give the best results, although the main limitation would be that access to the middle plate and removal of parts would be limited.

Overall however, removing the section in order to include the battery has little change on the effectiveness of the design of the side panel. Further exploration will be done into optimised light weighting of the design which may not be implemented on this iteration of the design due to time constraints, although the implementation of a fully optimised light weighted design would greatly aid the performance of the robot.

The ideal case would be a single light weighted outer chassis frame with possibility for modular attachment of RP parts for the electronics tray and aluminium holders for the two motors and batteries. This would maximise the possible use of space within the robot and could lead to dramatic weight reductions.

There is also a distinct possibility of adding 3D printed battery mounting cages in future, to allow the part to be quickly modified or replaced in the case of any requirements to do so. It may also be useful to look at a method that would allow both batteries to be removed from the same side of the robot in case of collisions and blockages of one of the side doors.

In conclusion, the recommendation is to cut the hole in the side panels in order to accommodate the batteries and also to weld, at the very least, the top and bottom plates to the side, in order

to improve the designs strength at impact by creating a single chassis frame, if this is not possible with time constraints, increasing the size of the bolts holding the plates together should reduce stress concentrations sufficiently upon any impact.

5.0 Cladding Design Portfolio Section

5.1 Introduction and redesign

The cladding of the robot was selected as an area of potential weakness and has a large potential for improvement. Therefore, it has subsequently been redesigned for several reasons. Firstly, the cladding was rushed by the previous year's team due to time restrictions; meaning that no simulation or testing was conducted. Therefore, there is no evidence that the cladding is satisfactory for the requirements and it is essential to ensure each part of the robot is validated through simulations and testing whenever possible. Another large concern was how much the robot weighs and there was the possibility of a reduction in weight by altering the cladding. Firstly, a material change was decided and carbon fibre was selected from an array of possible materials with the choice due to; a reduced density in comparison with the original material aluminium, the density being $1800kg/m^3$ for the carbon fibre and $2700kg/m^3$ for aluminium, but also due to the properties of carbon fibre it will be possible to make the new cladding thinner than the original, providing further reductions in weight. This is shown in *Figure 50.*

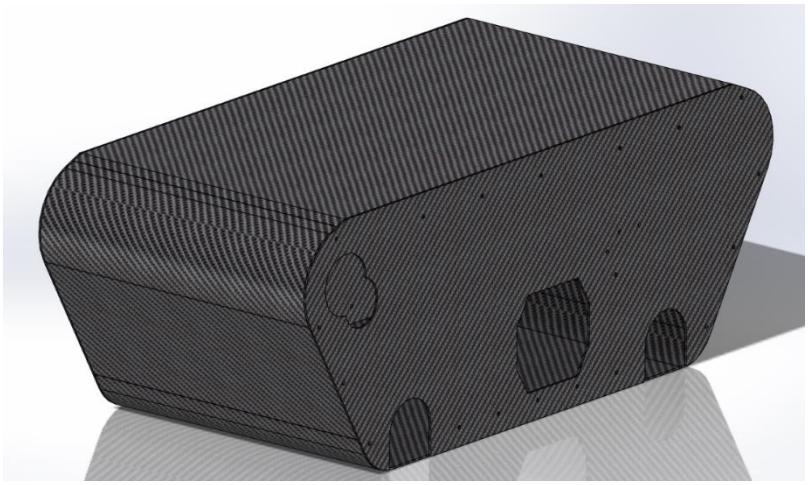

Figure 50: Carbon Fibre Cladding Assembly

A convenient hatch design has also been implemented into the two side panel cladding parts to allow access to the batteries, shown in orange in *Figure 51*. This is an essential feature from a safety point of view because it will allow for easy access and removal of the batteries in the event of an emergency. The section of carbon fibre cut out from the side panel to create the hatch, will be attached with a hinge, and locked with a sliding bolt to allow for easy opening and closing of the battery hatch. To ensure no water or dirt enters the robot through this, rubber seals will be put around the door to ensure ingress protection, as this is a concern regarding implementing these changes.

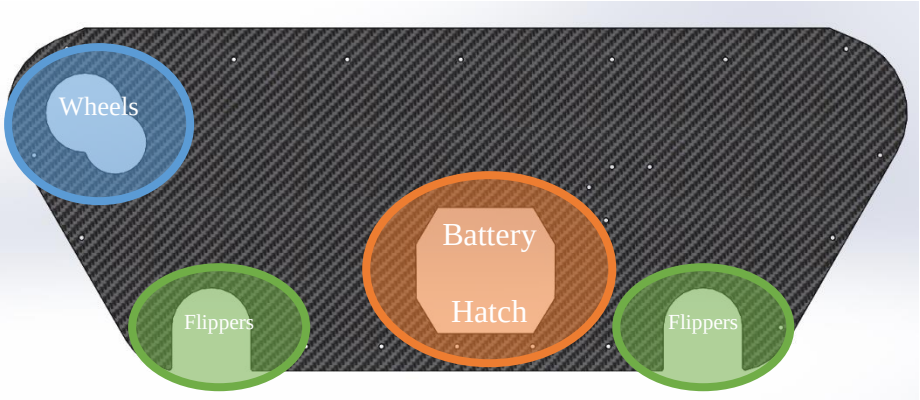

Figure 51: Side panel, with side hatch

The only downside of the carbon fibre in comparison with the aluminium is the heat transfer properties, so to compensate for this fans will mounted onto the carbon fibre cladding to encourage air flow over the electronic components keeping them as cool as possible. To do this fans will be attached to the hatch section that has been cut out of each side of the carbon fibre side panels. One fan will pull air through whilst the other pushes to encourage as much flow of air as possible.

Furthermore, another area highlighted as a potential weakness with the old cladding as a whole was the dust and water ingress protection, so to compensate for this rubber seals will hold together the top and side panels as shown in *Figure 52*. This will connect these three parts together as one piece therefore reducing chances of ingress, as this is the most likely areas for water to get in, for example rain fall. Then the front and back panels will be attached separately to allow for easy access and adjustment of the motors and electronic components.

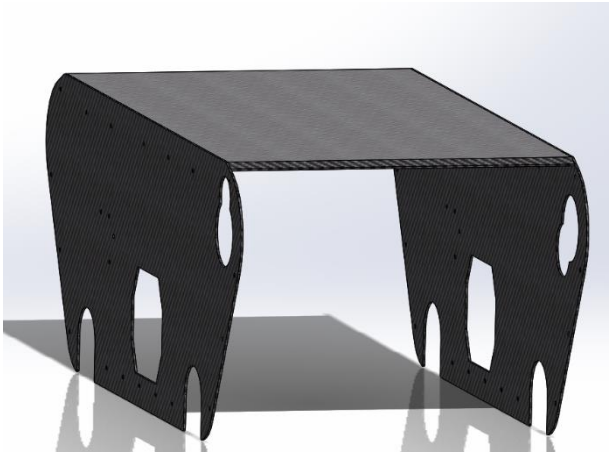

Figure 52: Top and side parts to be sealed together

5.2 Test 1: Side Impact

From here some simulations needed to be conducted to ensure the changes made to the cladding were appropriate. The majority of the testing was conducted on the side panels as this is the part that has been altered the most and would potentially be the weakest due to the various cuts and large number of bolt holes. First, a simulation was run on the side panels, simulating a side on impact, for example the robot slipping off a ledge on its side. For all the cladding FEA simulations the following parameters were set:

- The bolt holes to attach the cladding onto the robot were fixed.
- An impact force of 10,300N was put through the cladding, which in Section 4.4 was calculated as a worst case scenario of a force through the robot from a 35cm fall.
- The material was set as carbon fibre as this is what the cladding would be made out of.

The part was then meshed, with the test set up and mesh shown in *Figure 53*.

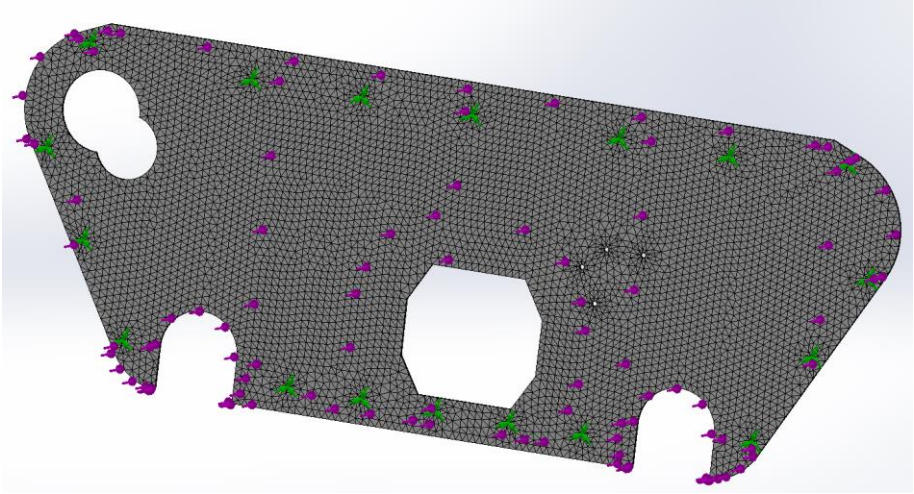

Figure 53: Meshed side panel, fixtures (green) and force (purple)

From here the tests were run and the results of the side impact test are shown below, as it can be seen the highest stress experienced, 386kPa, was significantly lower than the yield strength of the carbon fibre, 180MPa. With a maximum displacement of 7×10^{-5}mm. Therefore, in the event of this impact happening the cladding should be safe from any potential damage and therefore the delicate internals of the robot should be safe.

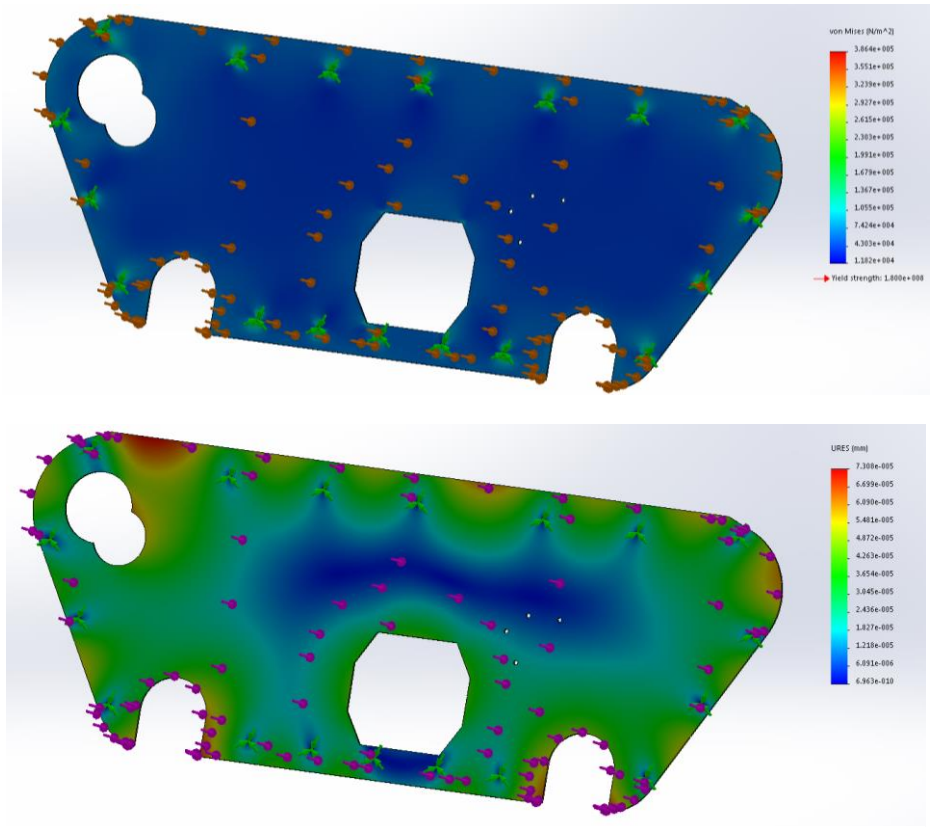

Figure 54: Side Impact Results

5.3 Test 2: Front Impact

The second test conducted was a front impact, for example if the robot falls down some stairs. In this case the highest stress experienced is 2.38MPa, slightly over the yield strength of the carbon fibre however when this is investigated more, it can be seen in the iso-clipping image in *Figure 55* that only a very small fraction of the material is experiencing a stress over the yield stress. Namely the small area surrounding two of the bolt holes, this could be a concern due to the composite nature of carbon fibre, being a structure of woven fibres, there could be a chance of the carbon fibre ultimately crumbing due to these high stress concentrations around the bolt holes. Especially considering drilling holes into carbon fibre creates inherent weakness due to the properties of the material being made up from layers held together by resin. However, this can be deemed as acceptable for several reasons. Firstly, the cladding will be fitted such that there is a slight room for flex which is something that unable be simulated in SolidWorks FEA, so the bolt holes being rigidly fixed will have led to these stress concentrations building up more. Secondly this is a worst-case scenario, so this small excess stress is potentially unavoidable and finally it would only result in a small crack in the cladding which can be simply replaced if it is large enough and will not result in damage to the internal components that it is protecting.

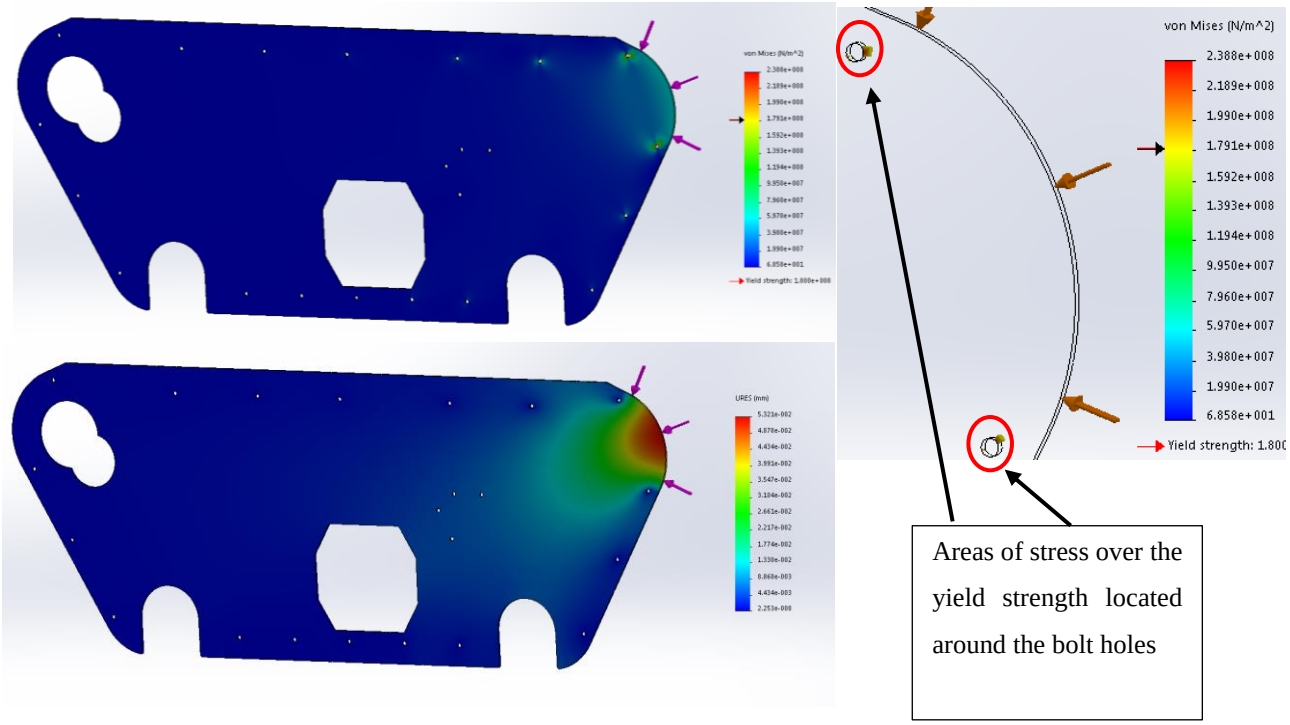

Figure 55: Front impact results

5.4 Test 3: Bottom Impact

Next was a potential impact from below the robot, for example if the robot falls down a step onto the bottom surface of the robot. In this case it would be very unlikely for the robot to fall flat on the bottom and would more likely be at an angle, therefore onto either of the side panels. The results for this test are shown in *Figure 56*, where it can be seen again the stress is below the yield stress of the carbon fibre. The stress throughout the panel is very low through the main body of the cladding and the higher stress concentrations are around the bolt holes again, meaning that the only major consideration is the chance of a fatigue failure around the bolt holes from multiple impacts over time. However, this is not too concerning as ultimately the cladding can be replaced and at this stress level it would take a large amount of impacts to lead to a fatigue failure.

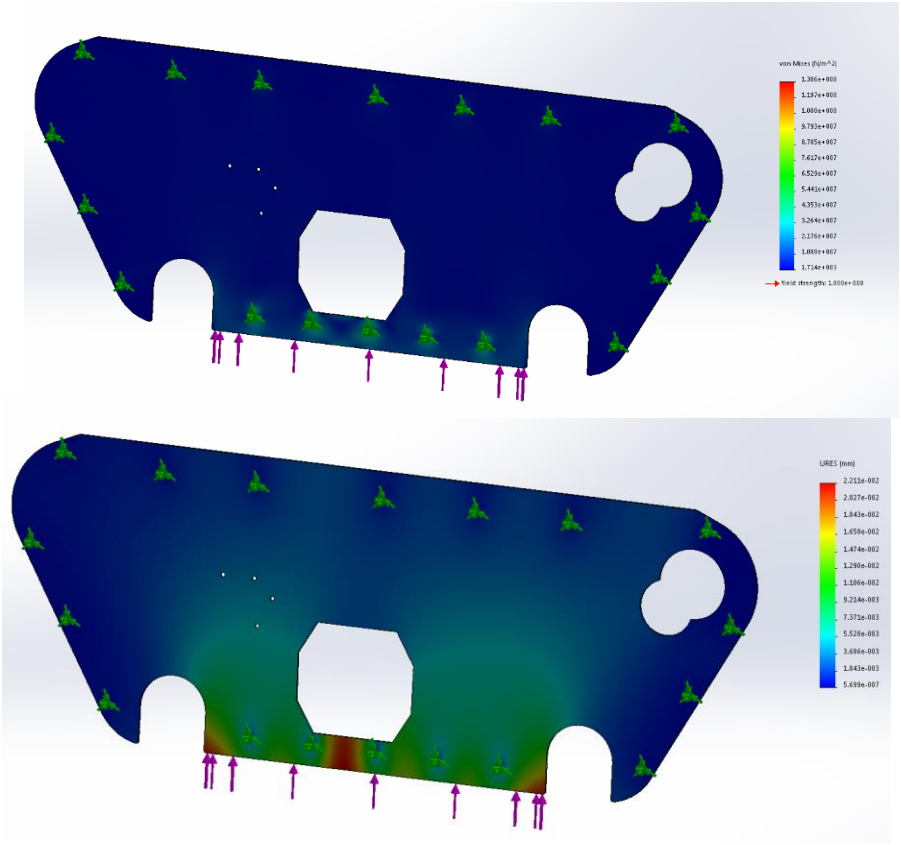

Figure 56: Bottom Impact results

5.5 Test 4: Top Impact

This test simulates the possibility of the robot tumbling over and landing on the roof, this could easily occur in a rescue scenario as the surfaces are often very uneven and hence it is still important that the robot survives in this case. The force was once again 10,300N because the robot may not land flat on the roof because the arm would knock the robot one way and the worst case scenario should be considered. The results are shown in *Figure 57* where it is seen that again the stress through the parts is less than the yield stress meaning that this impact should not cause any concern regarding any breakages.

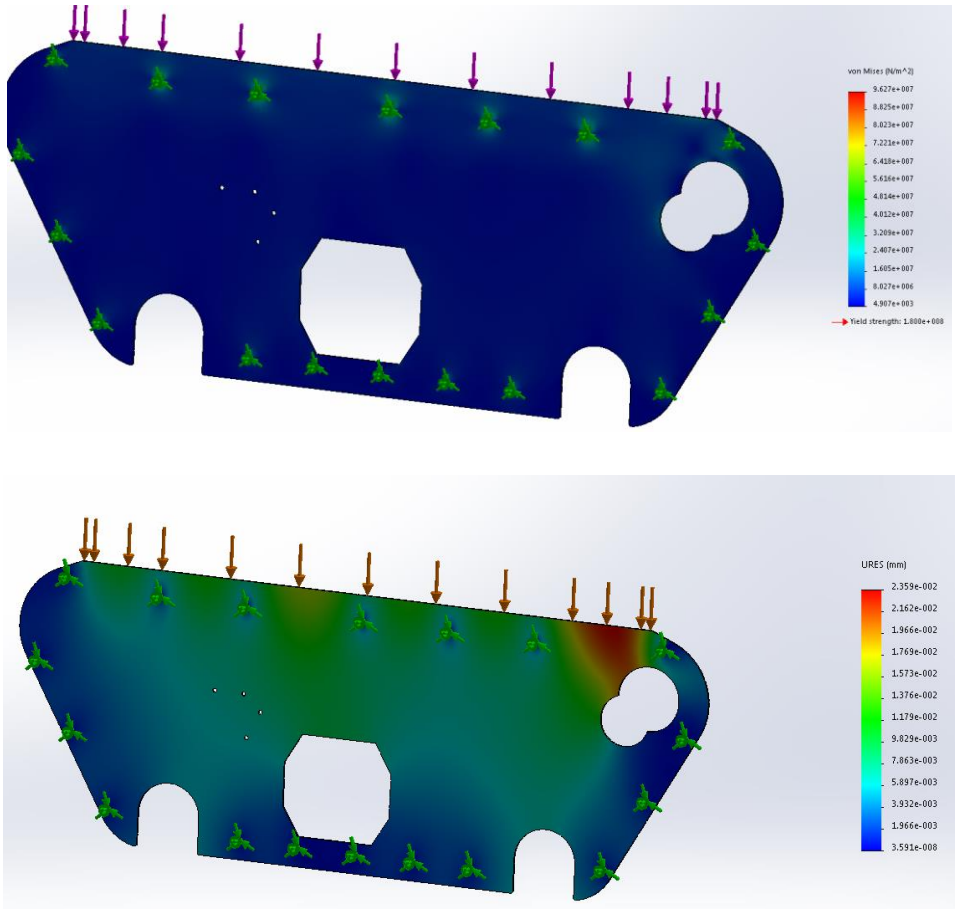

Figure 57: Top impact results

5.6 Test 5: Rear Impact

The final test conducted on the side panels was from the rear, this could occur when the robot is climbing up some stairs or is traversing over a large rock. Following the same previous test set ups the following results were obtained. Where the results followed a very similar trend as the results of Test 2, where the highest stresses were slightly above the yield strength, with a peak stress of 3.22MPa. However, when the results were iso-clipped to only show above the yield strength it became clear that the areas experiencing this were very small, as highlighted in red on the right in *Figure 58*. So, for the same reasons as discussed in Test 2, this can be deemed acceptable.

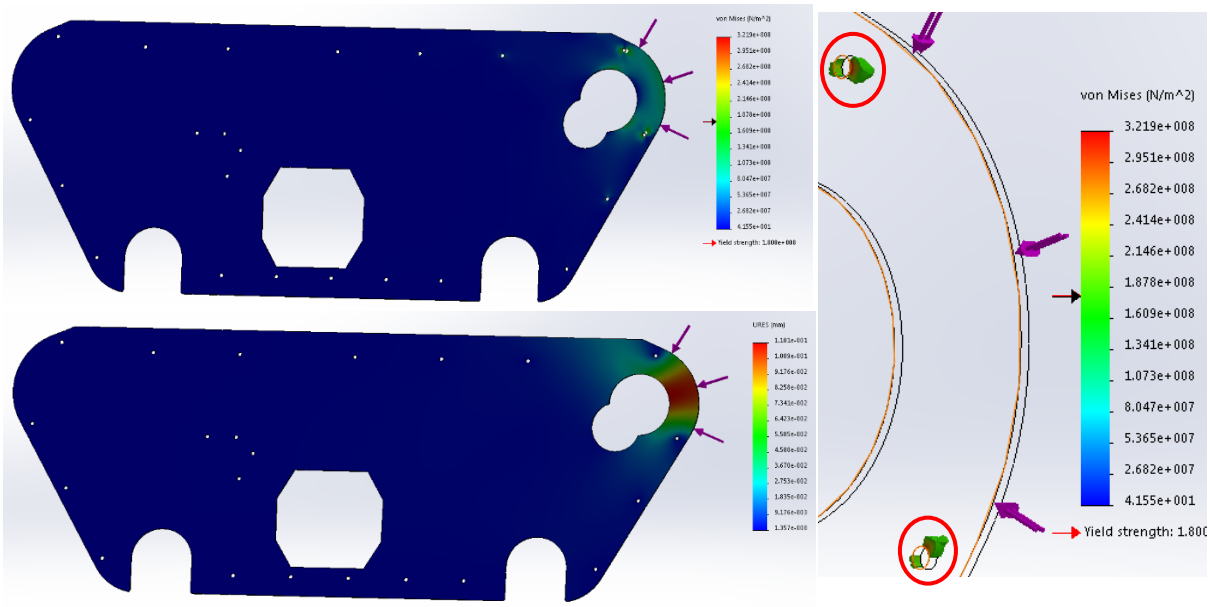

Figure 58: Rear impact results

5.7 Test 6: Assembly of side and top panel side impact

Finally, a test was conducted on the assembly of the side panels and roof panel, a side impact was selected because this was most likely to happen under real life testing as it would most likely tip over this way. All the bolt holes were fixed and again a force of 10,300N passes through one of the side panels, as shown alongside the mesh in *Figure 59*.

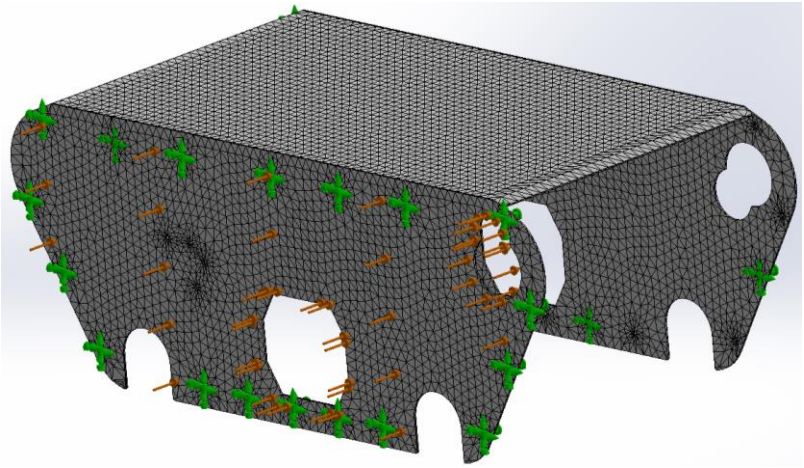

Figure 59: Assembly mesh, fixtures (green) and force (orange)

The simulation was run and the results followed similar trends as above, where the stress was higher than the yield stress of the carbon fibre, however this was deemed acceptable because

as seen in the iso-clipping the actual area experiencing this was very small again and was located around the bolt holes. Meaning ultimately a small crack could occur under worse case scenarios. A final point to be made would be that the cladding would be fitted onto the aluminium chassis in real life which would absorb a large portion of the forces and therefore reduce the peak stresses experienced. This was too computationally demanding to simulate so unfortunately this could not be simulated with the available computers. As for the displacements, shown in *Figure 60*, although the centre of the side panel displaces 1.3mm, this is deemed tolerable as it will simply flex and return to the original position. However, this would unlikely ever happened as mentioned the cladding is attached directly to the aluminium chassis panels, so the part be supported more leading to less flex and the possibility of breakages would be lower.

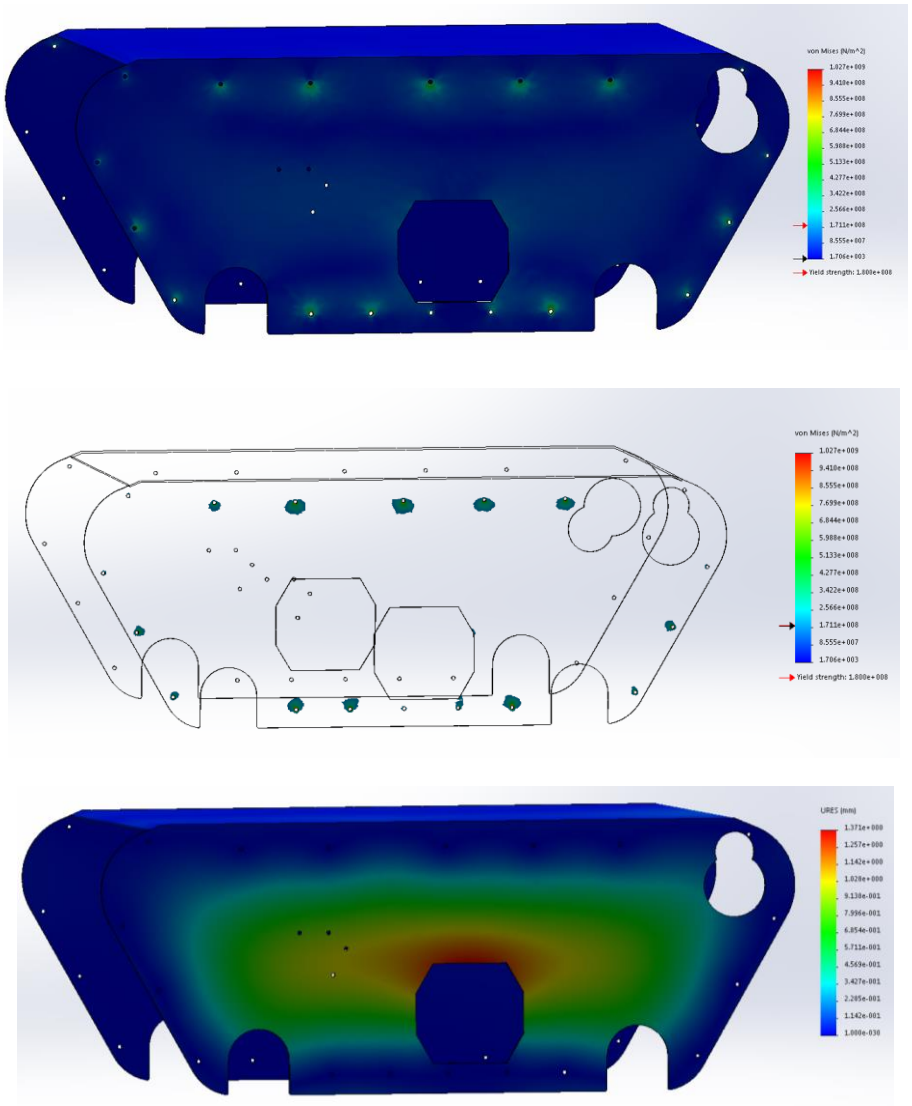

Figure 60: Assembly side impact results

5.8 Manufacturing

The manufacturing of the carbon fibre cladding panels will involve the team physically making the carbon fibre themselves in the GRP workshop within Warwick campus, with the assistance, guidance and tuition of a specialist in the manufacturing and use of carbon fibre for similar applications. The carbon fibre will be manufactured to the desired thickness for the application and then any further refined cuts from the panels, such as the battery hatch will be water jetted by Aquajet.

5.9 Physical Testing and Assembly

The design has been shown to be functional from extensive FEA testing and the only concern was the local stress concentrations around the bolt holes, but this is to be expected as this is where the cladding will be held in place and naturally stress will build up here. However, this is an incredibly important aspect considering the most critical decision when using carbon fibre is the correct choice of fasteners. This being due to the nature of the interwoven fibres, with no resin holding the fibres together around the holes, meaning that the wrong type of fastener could lead to crumbling and flaking of the cladding. So due to the composite nature of carbon fibre issues may arise that are not possible to be shown or simulated by computer simulations.

To solve this issue, some real-life testing of the components will be conducted once the parts are manufactured, firstly regarding the number of fasteners used to connect the cladding to the chassis, with emphasis being put on trying to reduce the number of fasteners used whilst also ensuring that the cladding is held onto the chassis tightly.

Then secondly, another more innovative option to be investigated first will be to find fasteners that do not require bolt holes to be cut into the panel in the first place, that also distribute the loads experienced by the fasteners across the whole panel. For example, a fastener that is specifically designed for being used with carbon fibre such as the selection of bighead fasteners shown in *Figure 61*. This type of fastener works by bonding the fastener to the panel with an adhesive meaning no bolt holes would need to be drilled and the weaknesses that would be introduced by drilling holes would be negated. By conducting some testing, investigating both of these options a solution should be found that reduces the chances of the carbon fibre breaking.

Figure 61: Fasteners for carbon fibre (Anon., n.d.)

Also, to reduce the build-up of stress concentrations in the first place, when the robot is being built the cladding will be fitted such that there is a small tolerance allowing the cladding to flex slightly rather than being completely rigidly held in place, reducing the build-up of stress concentrations. The worst-case scenario would lead to very small cracks forming around the holes, but this would not lead to any damage of the internals.

5.10 Conclusion of Cladding Design

To conclude the cladding has been redesigned to be more functional, by having better ingress protection, lighter, due to the reduction of weight from the material choice and the redesigning. Finally, it is more functional by having a hinge system for easy access and removal of the batteries.

Finally, it is noted for further information regarding the technical dimensions of the cladding, a sample technical drawing is shown below in 17.2 Technical Drawings. Here a drawing for the right side panel can be found, this part is the same shape as the left panel due to the parts being symmetrical. It is noted that the bolt holes to attach the cladding to the robot are still included on the technical drawing in case they are required to be made for the assembly of the robot.

6.0 Arm Design

The arm design is an iteration of a design made for the Champion Robot, around 10 years ago. This original arm design and construction can be seen in *Figure 62* and *Figure 63*. This took many years of constant improvement to finalise. This made the redesigning process complicated and coupled with its age it was decided that a new arm would need to be made. A simpler, more modular design allowed parts to be replaced when needed.

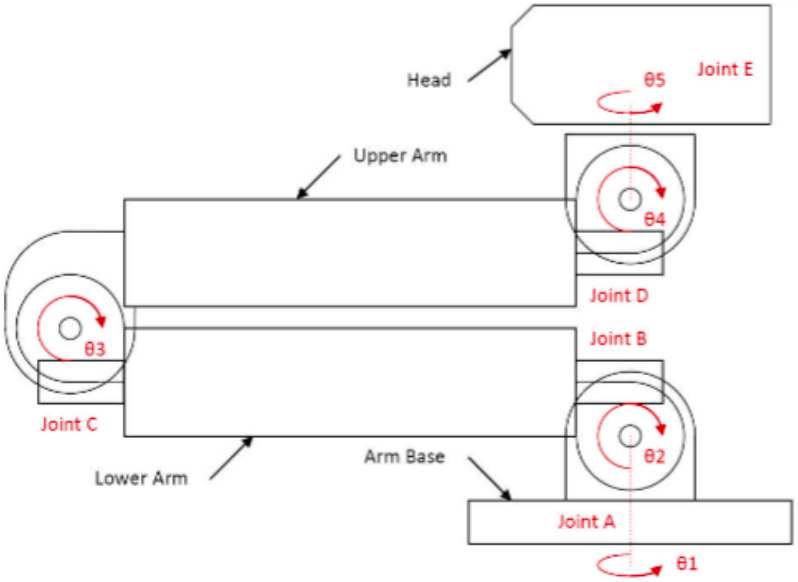

Figure 62 Champion robot arm design shown with 5 rotary joints, (Rushforth, 2017)

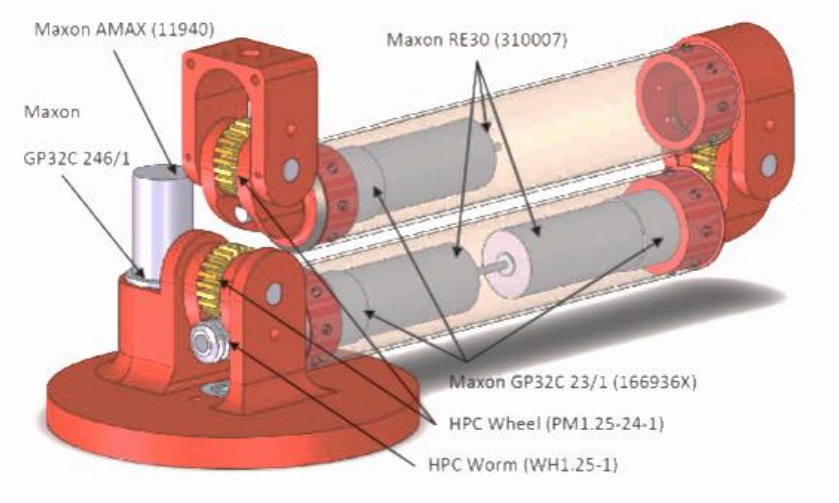

Figure 63 Image showing arm construction, (Rushforth, 2017)

The first change that was decided on was to change the material that the tube was made from. The original design was carbon fibre. This was very lightweight but struggled to deal with the forces acting on it at the base of the arm, and so had been reinforced after a few usage cycles to ensure the design stayed together. The dimensions for the two tube designs are shown in *Figure 64*.

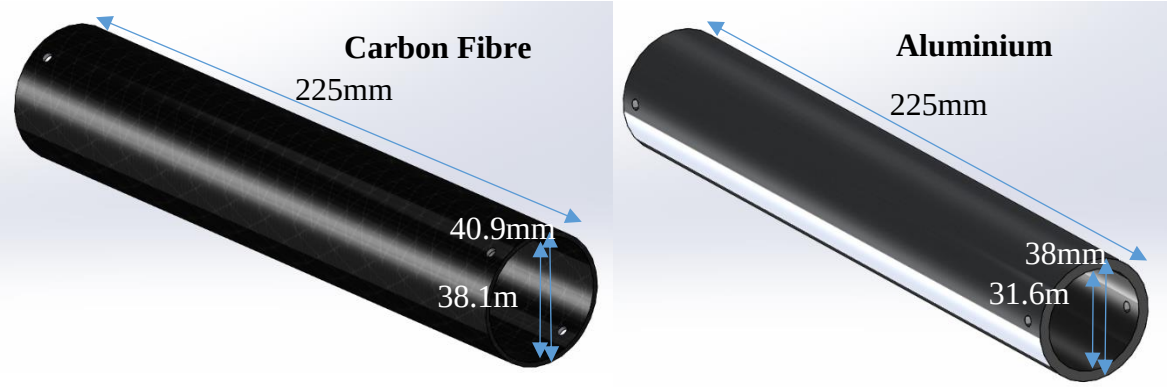

Figure 64 Size comparison of carbon fibre and aluminium tube.

The decision was made to change the design to use aluminium tubes, made from 6061 Alloy, in order to provide better strength to withstand the forces on them, while still maintaining a fairly lightweight structure.

MATERIAL	VOLUME	MASS	YIELD STRENGTH
CARBON FIBRE	39089 mm^3	78.2g	2760MPa
ALUMINIUM	78716 mm^3	212.5g	260MPa

Table 2 Comparison of mass of Aluminium and Carbon Fibre tube (Aalco, n.d.) (Matweb, n.d.)

Despite a significant weight increase and loss of strength, the change to aluminium means that the part is significantly cheaper than the carbon fibre version, meaning been able to buy a significant amount of extra aluminium tubing so that parts can be replaced if there are any breakages or other issues relating to the tubes. It also means that the tubes can be made longer or shorter if necessary in order to fit the usage requirement of the arm. The cost of this tube was very small relative to what it would have cost to produce carbon fibre tubes. As well as this, there is the possibility of recycling the aluminium tubes when they reach the end of their working life, something which would not have been able to be done as effectively if carbon fibre was used.

6.1 Base Joint and Base Modifications.

The next step was to look at the base of the arm and how the designs could be modified to make them simpler, lighter and more modular. It was decided to keep the two connecting joints that joined the base to the moveable section of the arm, as this would allow us to reuse the complex gear mechanism that allowed a motor to move that part of the arm. This meant that many positions of the base plate remained the same.

The original design shown in *Figure 65* was also used to mount a router to the robot, and also numerous connections for parts on the arm. This was removed to save weight, and also allowed for the excess material to be removed on the top half of the base plate to further save weight.

Router and connections to be removed and placed inside robot, in order to allow for reduction of weight, meaning top half of base will need to be redesigned.

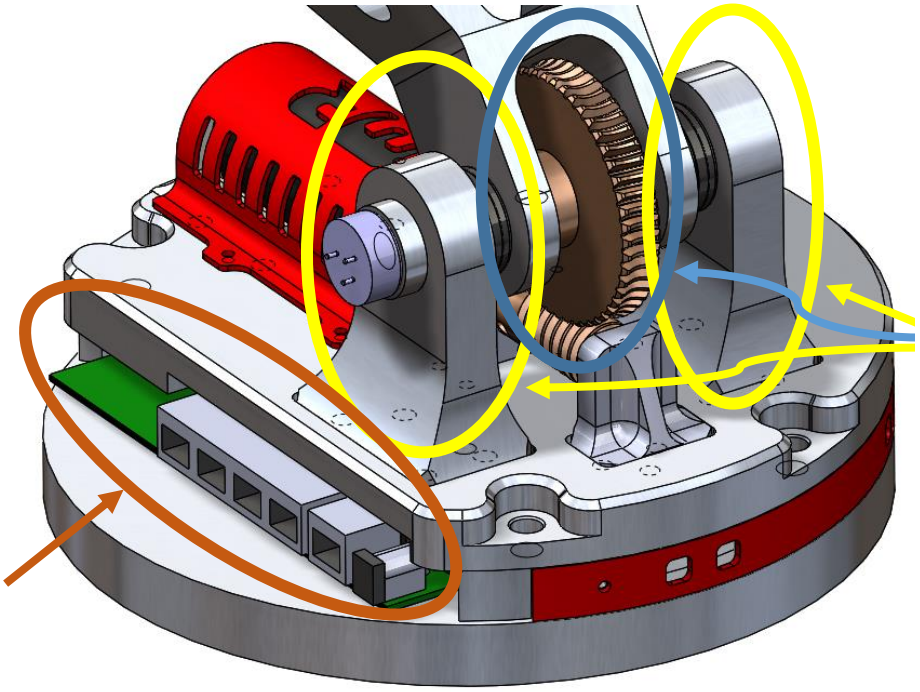

Base connections (yellow) to be kept as allows for minimum changes to gear system (blue) used to move arm, since we do not have budget to replace whole system.

Figure 65 Explanation of changes made to old base design.

By doing this, all of the bearings and the keyway used to join the arm to the base (which are all expensive parts that were still in ideal working order) could be kept. This reduces the cost and means that when parts do fail they can be individually replaced. This system with the motor driving a gear has been proven to work so it makes sense to reuse it. This will also mean that the connection of the base joint to the base can be modified in all other parts other than the connector.

This part is complicated to manufacture, and since it would be needed to change the top connections to the aluminium tubes in order to accommodate the new size of tube. It was also thought that this part should be split into two simpler parts that will be simple and quick to manufacture and will also have longer connections to the arm tubes, in order to improve contact fit.

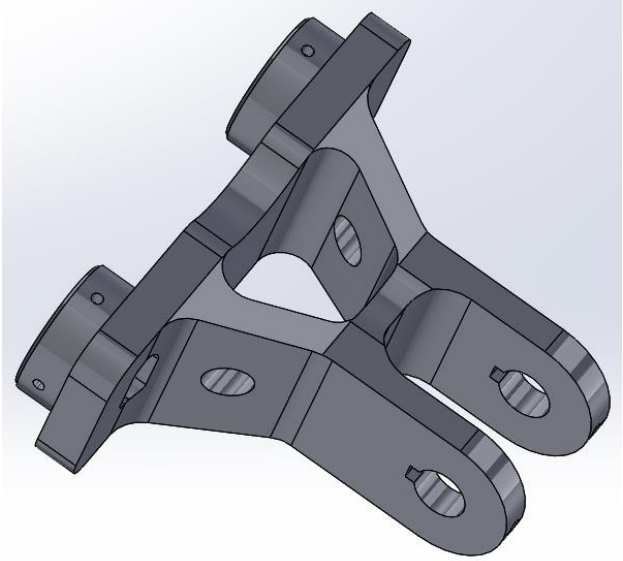

Figure 66 Old base connection design

The whole design modification was designed to fit the philosophy of a simpler more modular design. This design modification is shown in *Figure 67*.

Connection has been made longer in order to provide improved contact fit. Initially have been designed slightly wider than aluminium tube so that fit can be machined manually.

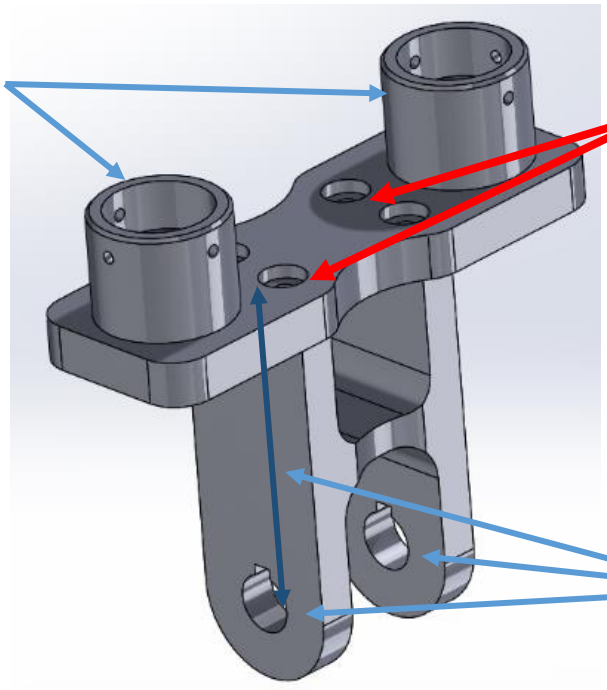

The two parts have been simplified in design and are held together with 4 M4 bolts in order to provide secure strong connection

Connection to base parts remains the same, as does the distance between the centres of the keyed holes to the end of the cross plate meaning that the length of the arm remains the same height as before.

Figure 67 New design for base connection.

FEA was used to compare this parts performance under loads to those seen in the original design. To simulate this, the part was assembled with the two connections to the base plate, and joined with pins, as seen in *Figure 68*. A force was applied to the top of the part to simulate the weight of the rest of the arm with load being carried and a small amount of extra weight, this equated to 30N.

A torque was also applied at the base of the joint, where it is connected to the base. This equates to 16 Nm, which is the torque produced by the arm under a worst case scenario of fully extended at a 90 degree angle with carried load.

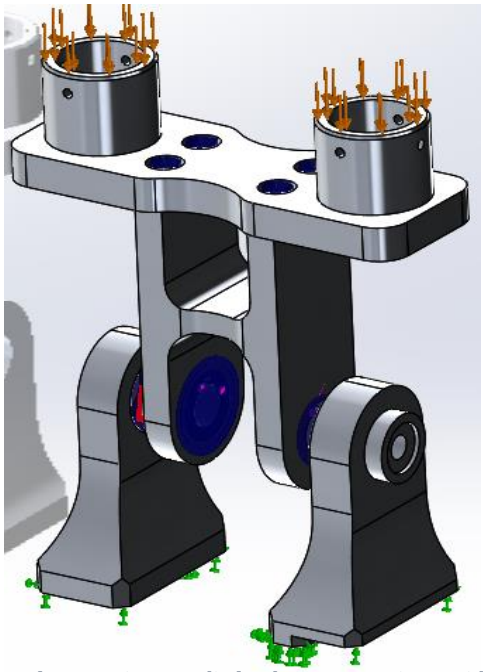

Figure 68 Illustration of loads and connections applied to base connections, with green signifying a fixed connection, blue connecting pins and orange load.

This load was applied to both parts so that the loads and displacements could be directly compared. The results for this are shown in *Figure 69.*

As can be seen from the results, the newly designed part shows significantly higher maximum stress than the original design, with an increase of 338%. However, this is still only 8% of the yield strength of the Aluminium alloys tensile yield stress. This shows that the previous design used an excessive amount of material for the application, and this can be seen with the weight reduction, with the design weighing 70 grams less in theory than the original.

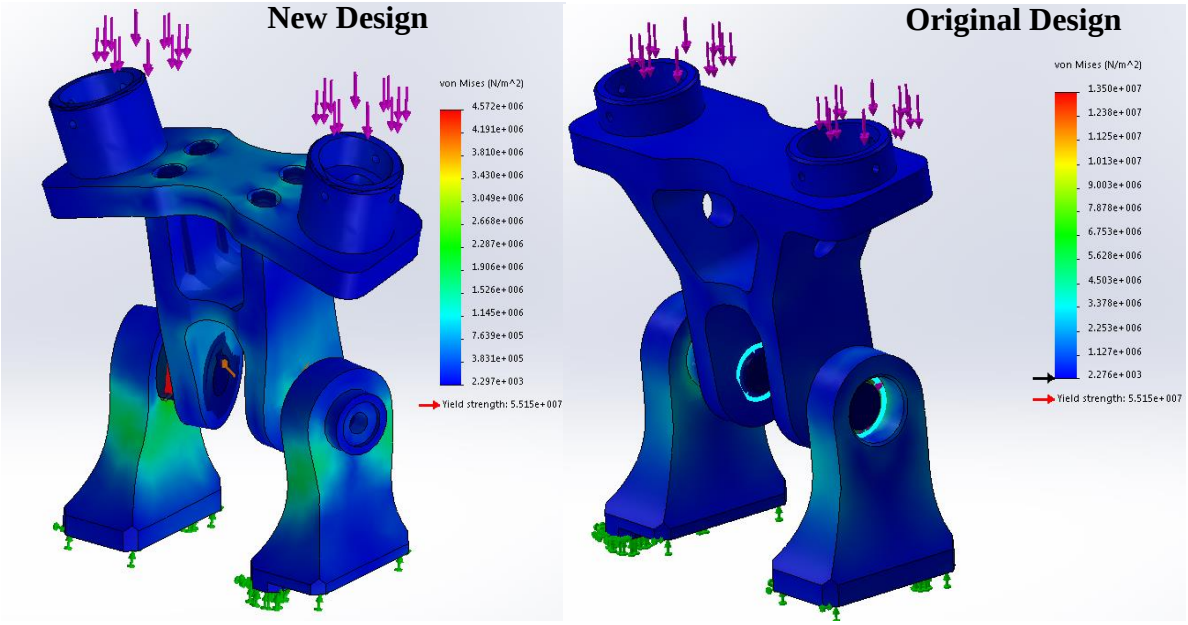

Figure 69 Stress plots for base connection parts.

The stress concentration across the majority of the base connections increased, suggesting this could be an area that is improved in the future. The main source of stress in both cases is around the pin connection, as is illustrated in *Figure 70*.

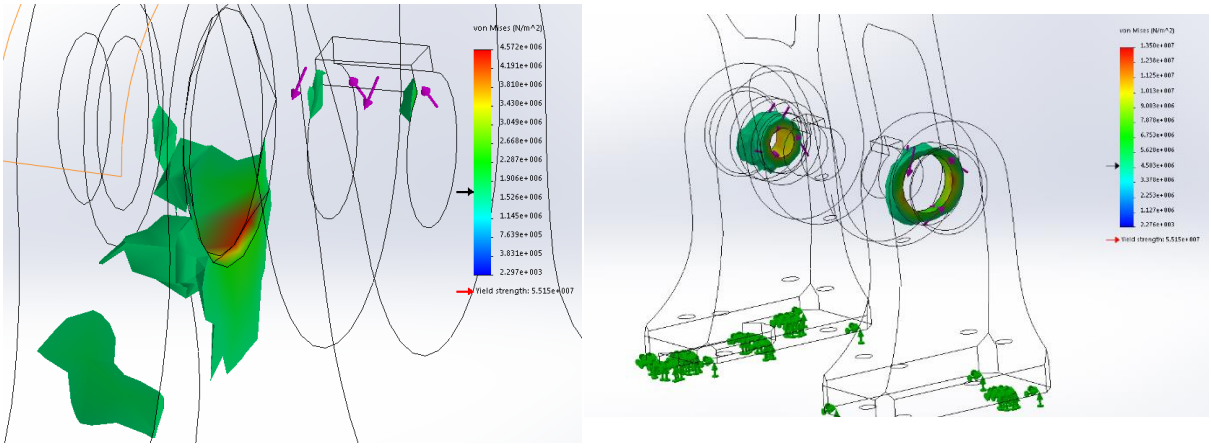

Figure 70 Stresses around connecting pin for both the new (left) and original (right) design.

Therefore, this is an area that could be looked into in the future, as the design for this part is fairly simple and there are numerous changes that can be made in order to ensure reduced stress response.

As previously discussed, the part of the base portion of the arm has been modified in order to remove weight from the robot as a whole once the arm is mounted. The part does not take large amounts of stress, so it was deemed that large amounts of material could be removed, leaving

just what was required to mount the part to the robot, and to mount the arm itself, and the motor and gear required to move it. This also means that the bearing and gear used to rotate the arm, mounted below this top part of the base plate, providing a serious cost saving as it was originally a very expensive part to buy. This original upper base plate part is shown in *Figure 71*.

This led to the design shown below in *Figure 72*, for the mounting plate for the arm. During the design process it was seen that the screw heads connecting parts would not be able to sit below the surface of the material and so give a close fit between the two base plate parts. Therefore, all of the indents designed for the parts to fit were raised by 7mm, in order to allow for the heads of screws to fit in recesses, while maintaining the same positions for parts.

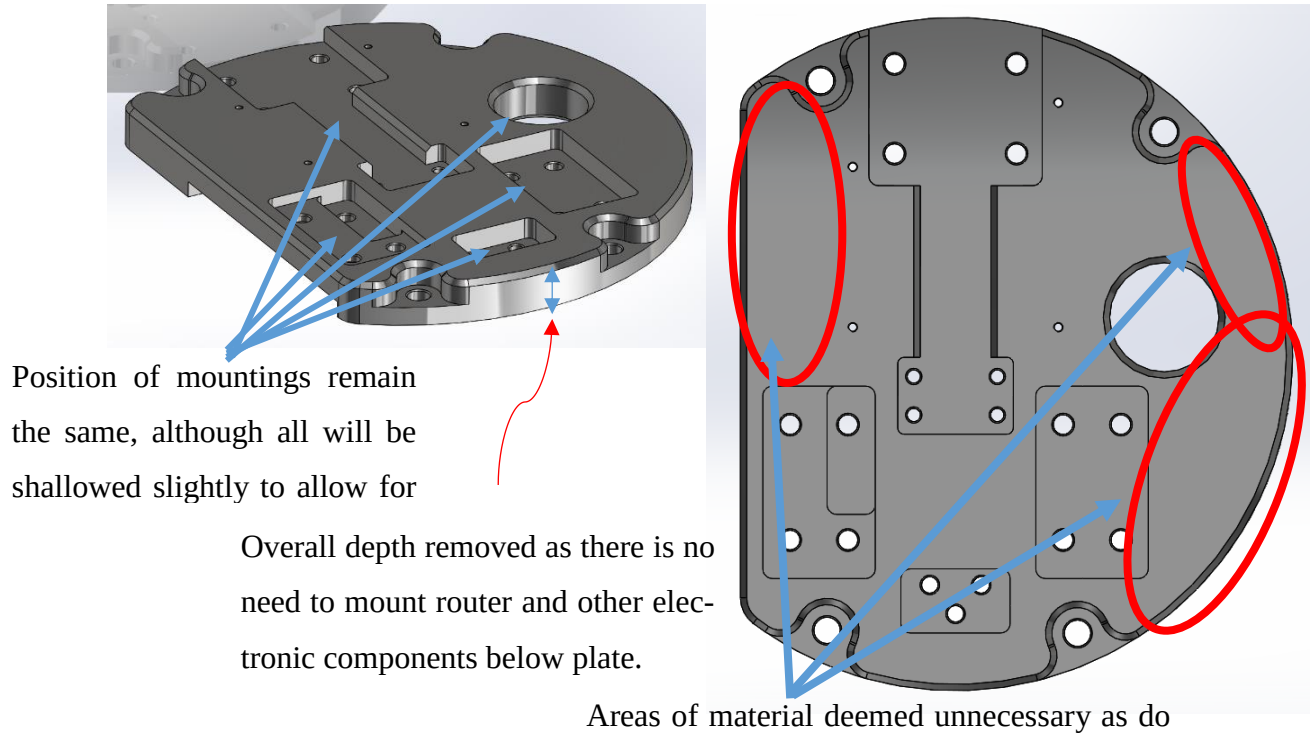

Figure 71 Illustration of changes to be made to base plate.

Overall, the redesign of the base of the arm has been done to save costs and make replacement of parts easier. The recycled parts of the base will mean that having a design that is usable and proven to work.

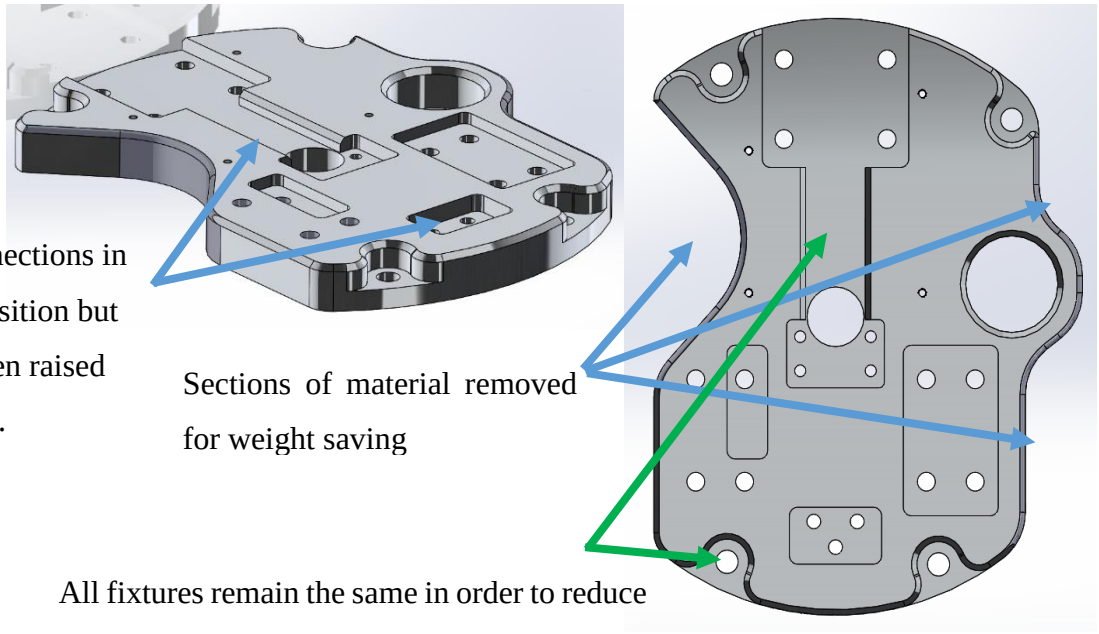

Figure 72 Changes made to base plate after redesign.

Rapid Prototype Connection Parts.

All of the 3D printed connections on the top of the arm and at the elbow had to be modified in order to accommodate the new Aluminium tube parts. Considering the old parts were quite old, this allowed more modern Rapid Prototyping techniques to be used, giving us the ability to make the part from a stronger and lighter material, therefore improving the weight of the arm as a whole.

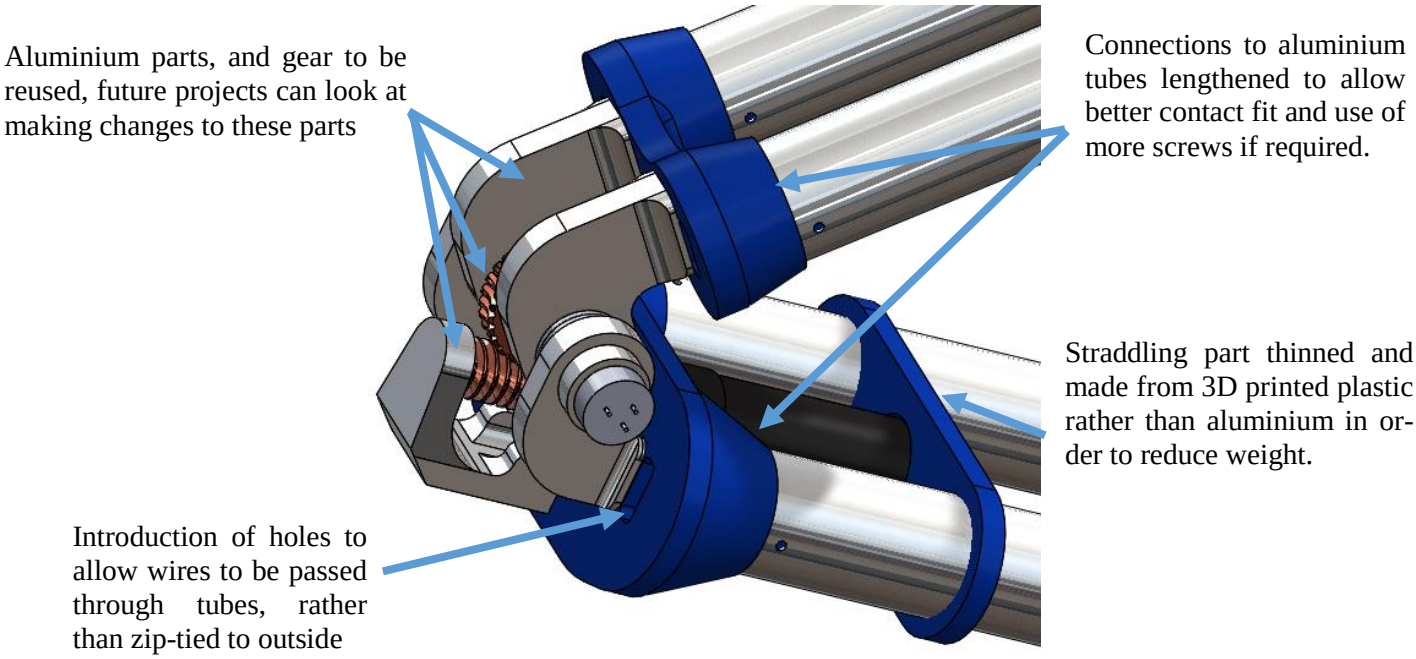

Figure 73 Illustration of design intent for arm elbow.

Many of these parts had very few changes made, as they were designed to fit the components used in the previous arm, some of which were being recycled. The main change was to lengthen and narrow the connections to the Aluminium tubes. The straddling part used to hold the elbow motor in place has also been changed to 3D printed material from Aluminium and had some slight shape changes, and made thinner in order to provide some minor weight savings.

The assembled view of the elbow can be seen in *Figure 73*. A small amount of FEA was carried out to ensure that the new plastic material could handle the load from the top of the arm under a worst case scenario of approximately 3 kg of mass at head and taking into account the added weight from using aluminium instead of carbon fibre. This is shown in *Figure 74*.

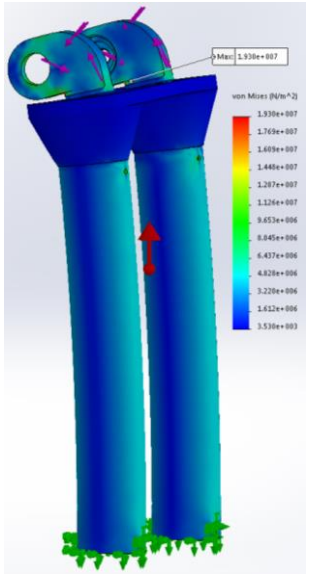

Figure 74 Stress plot for lower arm tubes, 3D printed connection and elbow connections

As can be seen, the majority of the stress concentrations are on the aluminium elbow connectors, rather than on the ABS 3D printed part itself. In fact, the stress concentration on the 3D printed part is virtually non-existent, relative to the yield strength of the material of 30MPa. The maximum stress seen is around 35% of the yield stress of the aluminium alloy chosen, and so is not an issue under even the most extreme expected working loads.

6.2 Arm Head

Figure 75 Image of original arm head.

The biggest change in the arm design from the previous one, shown in *Figure 76*, was the redesign of the head of the arm, in order to fit an end effector and camera to the arm, and allow for precise control.

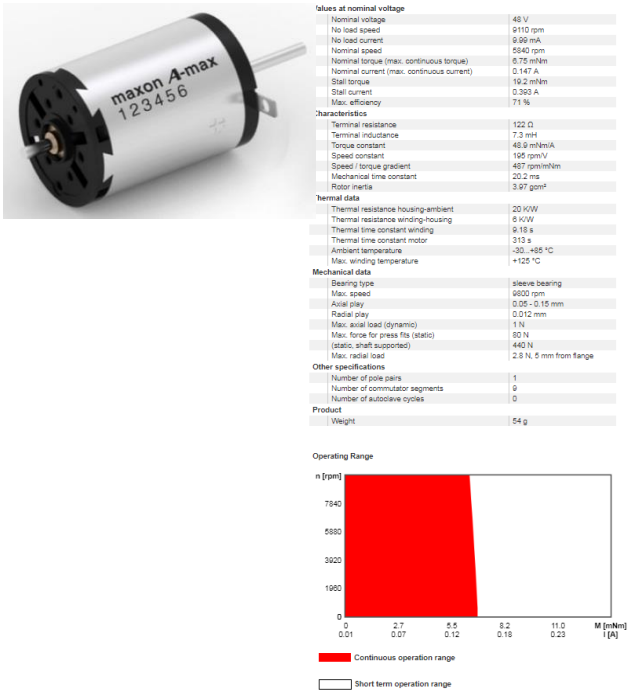

Figure 76 Data sheet and image of motor used for moving the

The main issue encountered was the fact that the two small motors used to tilt and rotate the head were not in ideal working condition. The actuator used to control the end effector was able to be used, and the camera was to be replaced with a new one capable of a much better picture quality. Therefore, the parts had to be designed to fit a set of small Maxon motors, details of which are shown in *Figure 77*.

Since there were many spares, it was thought that these would be ideal to use in the case of breakage, as it would mean that replacements would not have to be bought. It was decided to use two motors to provide the up and down tilting required to allow precise positioning, and one to provide the rotational ability of the head of the arm.

It was also required to make the head lighter than previous designs in order to save weight, and so the entirety of the new parts, other than end effector would be made from ABS 3D printed material.

The connection of the head was the first part to be analysed, due to the simplicity of forces acting on it. The equivalent of a 2kg load was applied to the top of the part, while the furthest end was modelled as fixed, to simulate the arm being at a 90 degree angle with the heaviest possible load being carried.

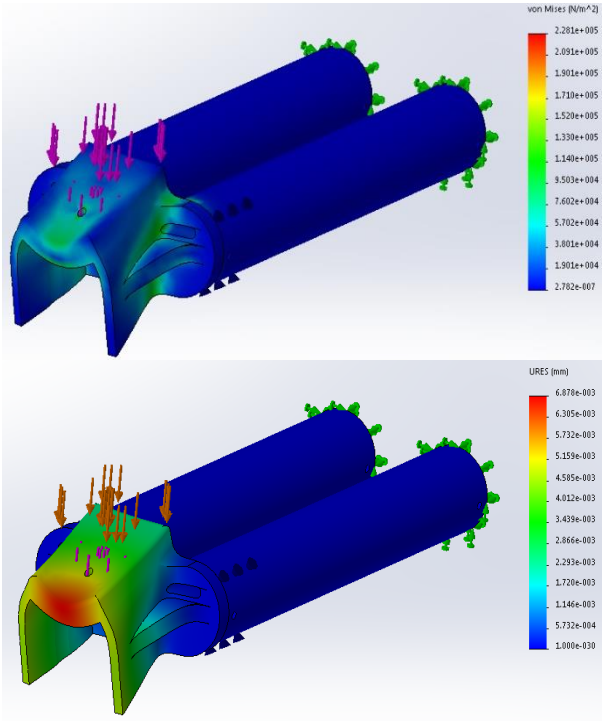

Figure 77 Stress plot (top) and displacement (bottom) of original head connection design

The initial design was built as an upside down bucket, where the motor could be screwed into the bottom, and then a rotating platform attached just above it. *Figure 77* shows the initial test.

The highest stress seen is less than 1% the yield stress of the material, meaning there is no real area for concern with this part. However, in order to reduce the bowing of the centre of the mounting with the motor, which could lead to alignment problems, an increased cross area was added, as shown in *Figure 78*. This reduces the displacement to simply the bending of the part as a whole, rather than the curving of the centre of the mount.

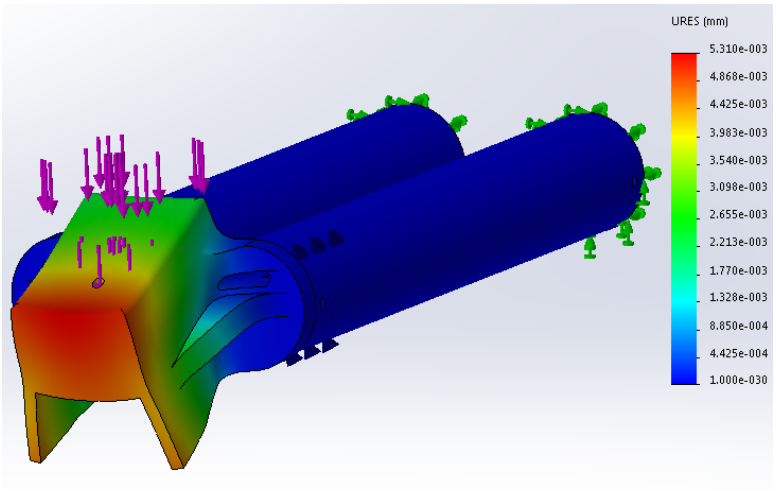

Figure 78 Displacement plot for redesigned head connection.

The final part designed was the top mount, required to mount the camera end effector, and so be able to take the 2kg load. The initial load applied was equivalent to around 10 kg acting on the head, well above what will likely be required in order to ensure the part does not fail when caught under extreme conditions. The initial design was conceived to be a simple thin bucket, as seen in *Figure 79*.

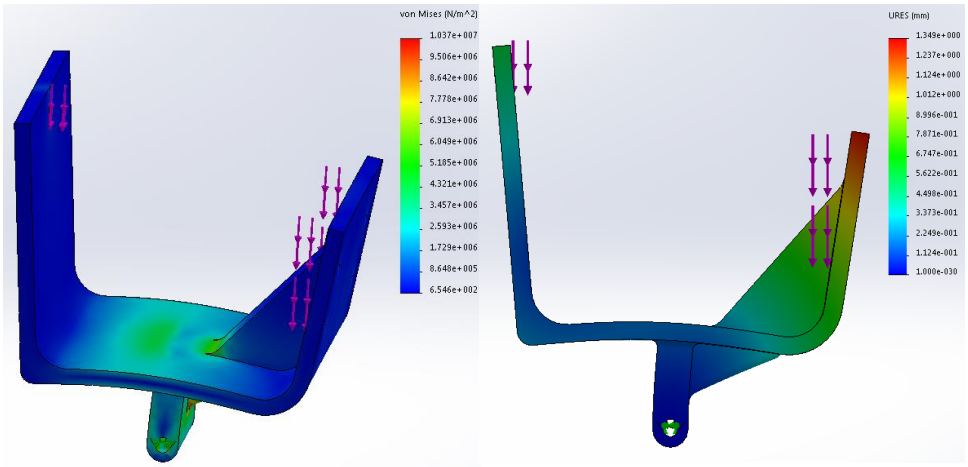

Figure 79 Displacement plot for redesigned head connection.

The maximum stress is around a third of the yield stress meaning the design should be suitable for use. However, the displacement shows that the area where the camera and end effector are mounted, are curving away from each other, leading to possible problems aligning the end

effector due to the camera possibly not being able to see it, since the displacements seen are fairly large.

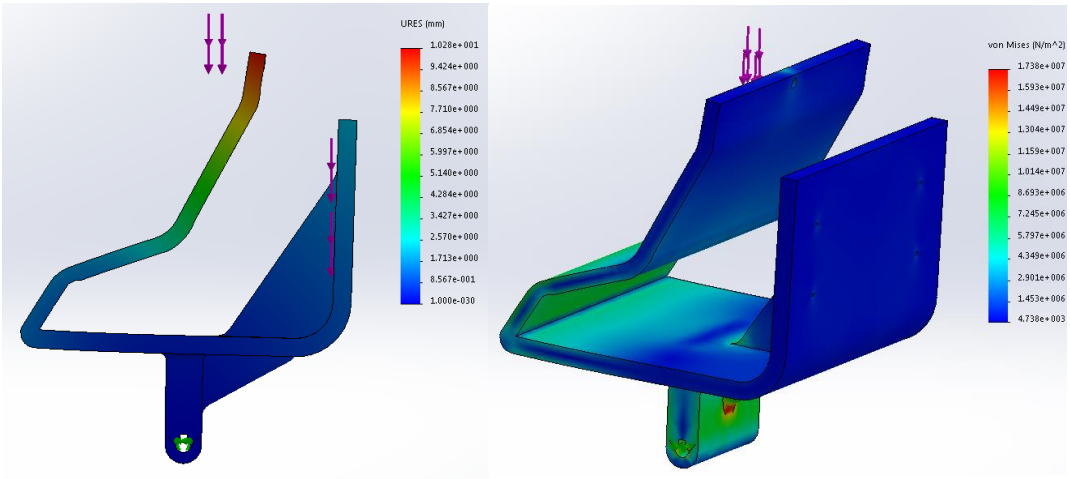

Figure 80 Displacement (left) and stress (right) in redesigned head top.

Therefore, it was decided to mount the camera above the centre line of the part, in order to cause this to displace less, and to reinforce the end effector side more, to minimise the deflection on the part with the camera.

This led to the design shown in *Figure 81*, which was designed to allow some damping for the camera with the design of its mounting. However, this led to excessive displacement of this connector which could have led to very shaky camera motion, so it was thought to add connections between the front and back of the part. Also, reinforcement has been added to the strut at the base of the part, in order to reduce the stress concentration seen there.

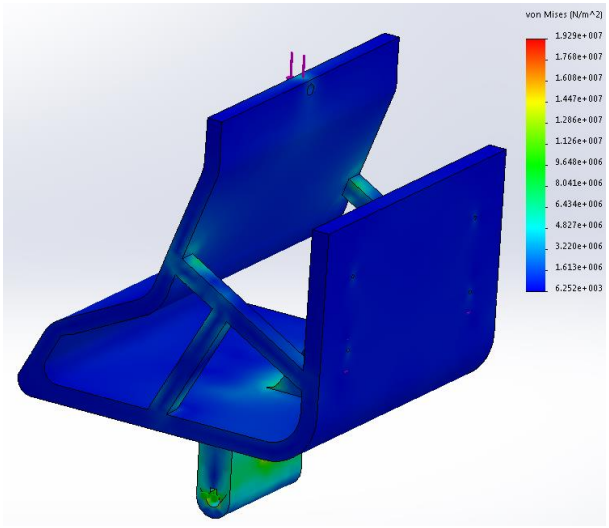

Figure 81 Stress plot for final head top design.

The maximum stress in this case is just above half the yield strength, showing that the material will be ok under normal operating conditions.

The displacement for this remains almost the same as the previous iteration. However, the entire of the vertical sections now move together, ensuring the camera always follows the end effector. The highest stress concentration is around the connection hole at the bottom, suggesting that this may not be the most realistic solution. It is still only around 60% of the yield stress and so should not be an issue, although this is an issue that can be addressed in future project groups.

6.3 End Effector

The choice of end effector sets the upper limit on what the arm on Atlas can do. There is a large variety of end effectors for a variety of different purposes; grippers of different shapes and sizes, tools for specific uses (drills, spray heads, welding) and vacuum cups.

When designing the appropriate end effector, the objective was to grip and hold small objects that can be carried and placed by the arm. It was concluded that a two-pronged end effector, formed from aluminium sheet, with rubber at the gripping end, would ensure hold onto slippery parts.

Figures 82 below shows the initial sketches of a two-pronged end-effector that lead to the final design.

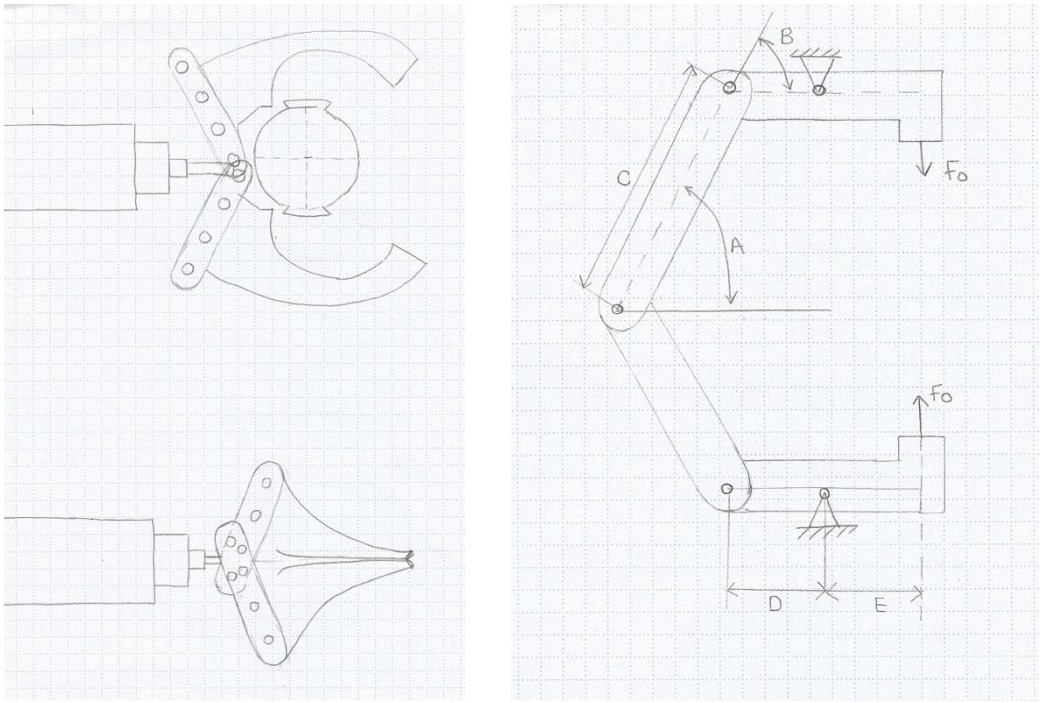

Figure 82 Sketches showing shape considerations of end effector

6.4 Final Arm Design

The final arm design can be seen in *Figure 83* all redesigned RP parts can be seen in blue. The only part not included in this report is the cover for the motor on the base, which is not structural and was simply remade to fit the colour scheme of the rest of the robot. The end effectors are not included due to difficulty modelling the mounting on the actuator, but in reality this is already made and so is not of issue.

The 2008 Legacy arm would need major repair if it was to be made to work. The main changes are to the 3D printed head of the robot which has been modified due to the use of new parts. There has also been a light weighting process on the base of the robot and a modification to the base joint to the bottom pair of aluminium tubes in order to make manufacture quicker and easier, and so cheaper, making the arm as a whole easier to repair and replacement of parts cheaper.

The change of the tubes from carbon fibre to aluminium has increased the overall weight of the arm, but it has meant that the tubes have been made much easier to replace as they are cheaper and quicker to order and manufacture. For Technical drawings of all these parts see 17.0 Technical Drawings.

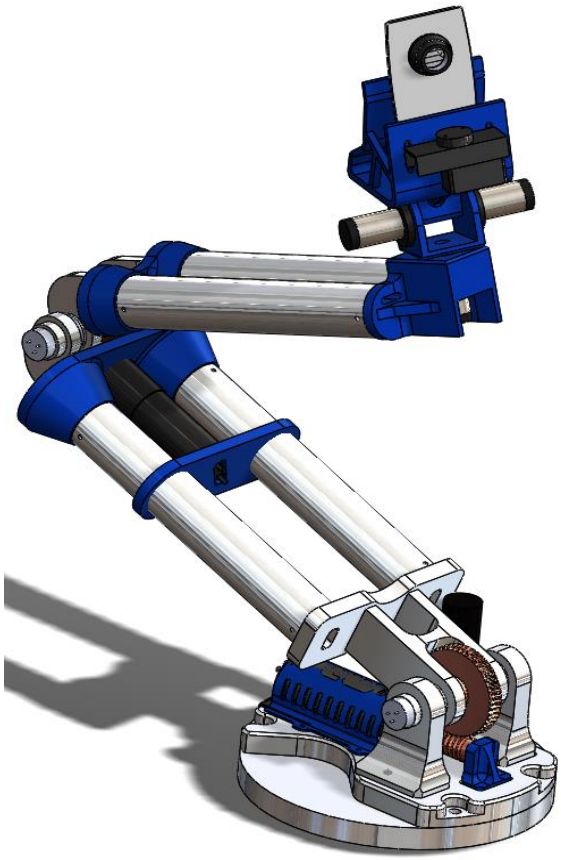

Figure 83 image of Assembled arm, including camera, end effector actuator and all driving

6.5 Manufacture

Once design for all parts was completed, they were sent off to the technicians for final scrutinisation before manufacture. It was recommended that all connections be modified in order to allow for the best possible fit between parts.

For example, the cylindrical faces connecting the 3D printed parts to the aluminium tubing should be made 2mm wider in diameter, and all recesses in the base part be made smaller by 1mm on all faces. This is to allow all parts to be hand finished to ensure proper fit between parts. As well as this, all 3D printed holes were to be made just 2mm radius since the manufacturing process is not able to make precise holes at that size. These will again be hand drilled once the part has been made. Once these changes were made, manufacture could begin.

As mentioned above, all blue parts in *Figure 83* were to be 3D printed. This process was chosen as it allows for the manufacture of complex parts in a quick time frame, while recent advances have allowed for increasingly complex designs and for lighter and stronger material to be used (Wellington, 2013). It also allows for thin sections to be made precisely down to a thickness of 3mm, which is ideal for some of the designs seen, that have a thickness of merely 5mm in places.

As has been stated all holes were hand drilled from positions defined by 2mm rough holes. No holes were designed to be tapped due to the difficulty in doing this with 3D printed material, and so all holes were designed so that they could be screwed to aluminium parts that contained tapped holes.

All aluminium parts were computer milled to their near finished rough shape from blanks of material. This method was chosen as the parts are not particularly complex in manufacturing terms and so this method allowed quick and accurate production of parts. These were then hand finished to ensure proper fit of all parts. All holes were computer drilled to their rough size and then all that required tapping to screw parts into where required.

7.0 Dynamic Tensioning Springs.

The aim of the springs in the dynamic tensioning system is to maintain the tracks at a near constant tension in order to ensure tracks don't slip or become dislodged under rough ground and climbing conditions Therefore, it is important to ensure that the springs are stiff enough to push the weight of the tracks out, while being able to compress when the tracks tighten significantly so that the tracks don't get damaged. The current design is a static tensioning system, although it was designed with the possibility of adding a dynamic system to it when there was an opportunity to do so.

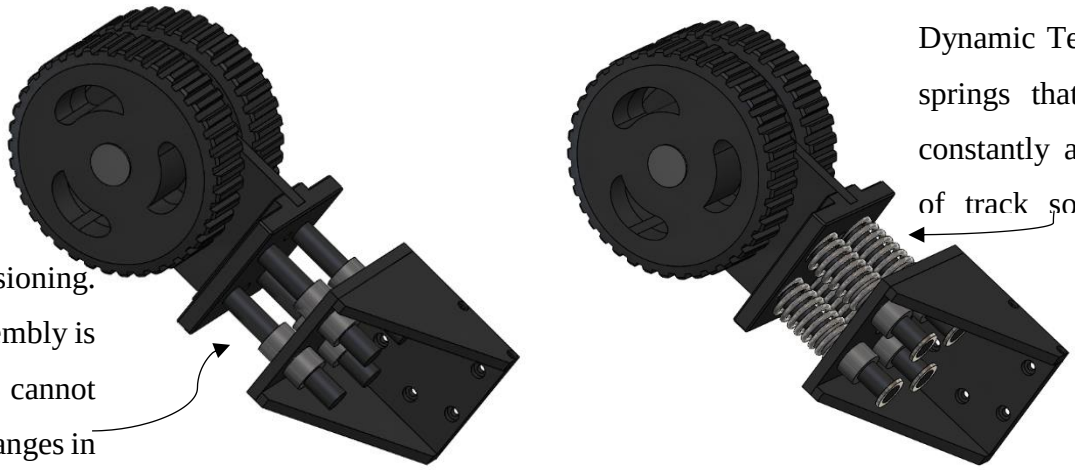

Figure 84 Explanation of Static (left) and Dynamic (right) tensioning systems

From a variety of springs physical experiments were conducted to determine which would be most appropriate for use in the tensioning system. This involved fitting springs to the tensioning system and performing drop tests, as well as fitting it to the robot in order to test its size and ability to hold the tracks in position.

Spring Identified as what wanted:

Outer Diameter (mm) D	25.5
Inner Diameter (mm)	20
Wire Diameter (mm) d	3
Un-extended Length (mm) L	100
Max Compression (mm) approx.	50

Table 3 Properties of ideal spring required for tensioning system.

Spring Index, C: $C = \frac{D}{d} = \frac{25.5}{3} = 8.5$

Spring Constant, k: $k = \frac{dG}{8C^3N}$

G=80x10^9 for steel N-Number of turns=12

So k=4070 N/m=4.07N/mm

This is total spring constant, so will need 4 springs

Want spring around 1-1.3 N/mm constant

Chosen spring must have stress at maximum extension of below around 650Mpa to allow safety margin.

In summary want spring that satisfies:

- Constant around 1 N/mm
- Un-extended Length around 100mm
- Can compress by around 50mm
- Has a max stress at 50mm compression below 650Mpa
- Inner diameter greater than 20mm to fit around tensioning system part

Closest spring found to specifications from available sources is:

Outside Diameter	27mm
Wire Diameter	2mm
Free Length	135mm
Minimum Working Length	31mm
Load at Minimum Working Length	127.49N
Material	Steel Alloy
Spring Rate	1.23N/mm
Ends	Closed (Square)/Ground

Table 4 Properties of selected spring (RS Components, 2018).

Testing at max extension (50mm) for stress

$\tau_{max} = \frac{8FD}{\pi d^3} K_b$ where $K_b = \frac{4C+2}{4C-3}$

So $\tau_{max} = 613.8$MPa

So the springs will be a good fit for use in the dynamic suspension of the robot. They have an appropriate size to fit on the suspension and are long enough with a high enough spring constant to resist the weight of the tracks, while also being able to stretch and compress in order to accommodate changes in the state of the track.

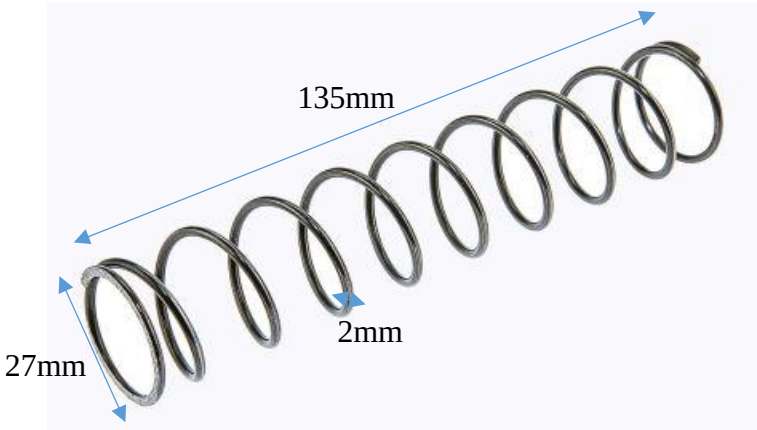

Figure 85 Image of spring to be used for dynamic tensioning with dimensions (RS Components, 2018)

.

8.0 Electronic System Design

The design for the electronic and electrical system of the robot consists of 4 essential parts. The base station, the power supply, the instrumentation and motor control and the camera system, see *Figure 86*

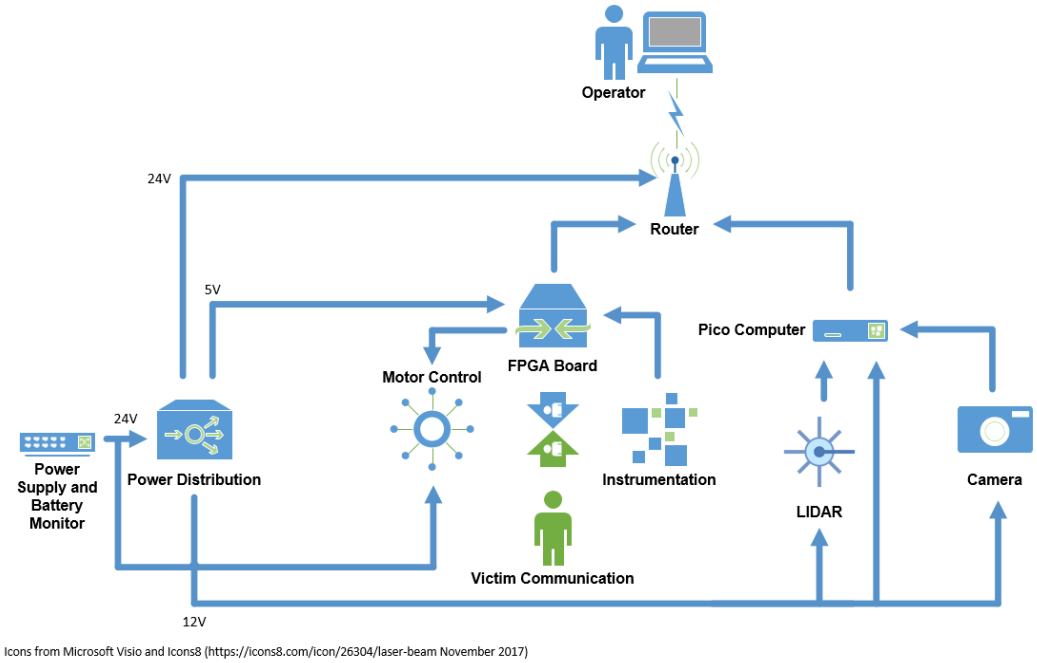

Figure 86 Electronic System Diagram

The operator communicates with the robot via a wireless link from a base station computer. An onboard wireless router receives the signal from the base station and transmits it to the peripherals through wired ethernet connections as shown in *Figure 86*.

A goal is to operate the robot of a single power supply, consisting of ~24 V Lithium Polymer batteries, the choice fell to this type of batteries due to their high energy density (Owens, 1992) and their availability because of a purchase from a previous iteration of this project. The batteries need to be able to provide high currents if required, since the chosen DC motors may require peak currents in excess of 80 A. Due to this, the batteries will, via an emergency-off button, connect to two copper bus bars, because of their high current carrying capability. These bus bars will then deliver power directly to the motor controllers and the power distribution board described in the next section.

9.0 PCB Designs

9.1 Power Distribution Board

Three different direct current (DC) Voltages are required to operate all parts of the robot, 24 V for the motor controllers, motors and the Wireless-LAN Router, 12 V for the Pico computer and motor controller logic, LIDAR and Camera and 5 V to the FPGA board and other instrumentation.

To obtain 12 V and 5 V from the 24 V supply it is necessary to design a printed circuit board with components that generate and safely distribute these. Because of this, two isolated DC-to-DC converters with sufficient output current ratings were chosen. In *Figure 87* these are marked as "A1" and "A2". Isolation provides essential protection from current spikes that may, in an exemplary embodiment, arise when the motor controllers draw instantaneous peak currents. This should also eliminate the need for protective fuses in this part of the electronic system.

For cost reasons, the motor controllers to be used are the AX3500 by RoboteQ (Digilent, 2016). These were purchased by a previous project group some years ago. However, the instruction manual outlines the requirement for an emergency power supply to the controllers' logic circuitry should power from the main batteries be cut off at any time. For this reason, the system depicted in *Figure 88* and *Figure 89* was designed, simulated according to *Figure 90* and implemented on the power distribution board according to *Figure 87*. The circuit consists of a reference voltage from a shunt regulator that is fed into a comparator. Should the output voltage from the two DC-to-DC converters fall below this threshold, the comparators switch transistors Q1 and Q2 on and continue to supply 12 V and 5 V from a smaller back-up battery. To ensure the comparator output remains high, transistors Q4 and Q5 effectively disconnect the converter outputs from the attached components. This system will also allow communication with the robot when the main power supply is off. Chosen components are labelled in the Figures below. The shunt regulators incorporating DZ1 and DZ2 (TZX5V1B-TR) were designed to provide a low current voltage reference of 5.1V for the Comparators. They run off a 5 µA current, which requires 1.4 MΩ resistors for R3 and R4.

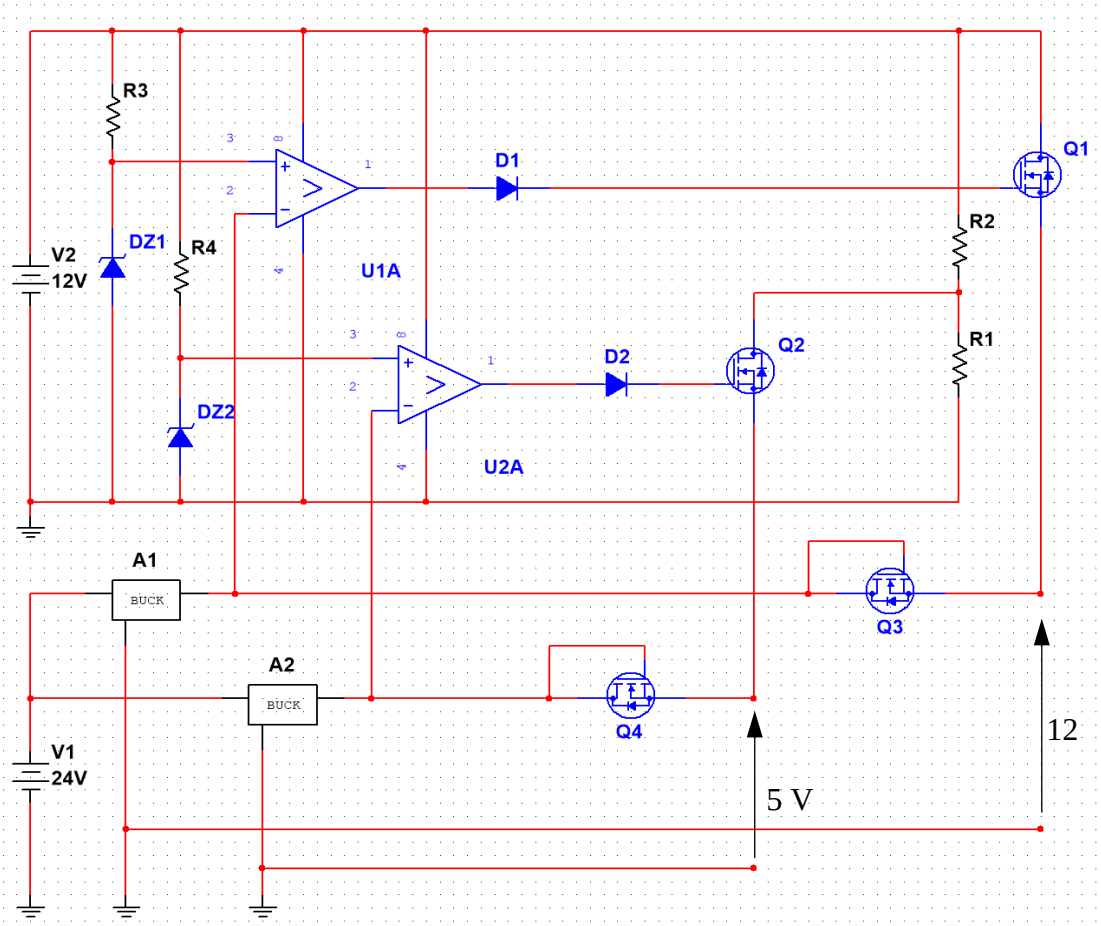

Figure 87 Schematic of Power Distribution Schematic with Emergency Power Supply

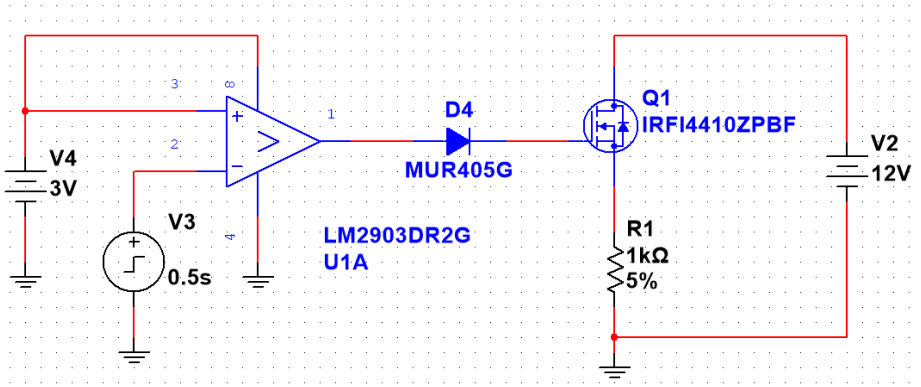

Figure 88 Comparator Simulation Circuit

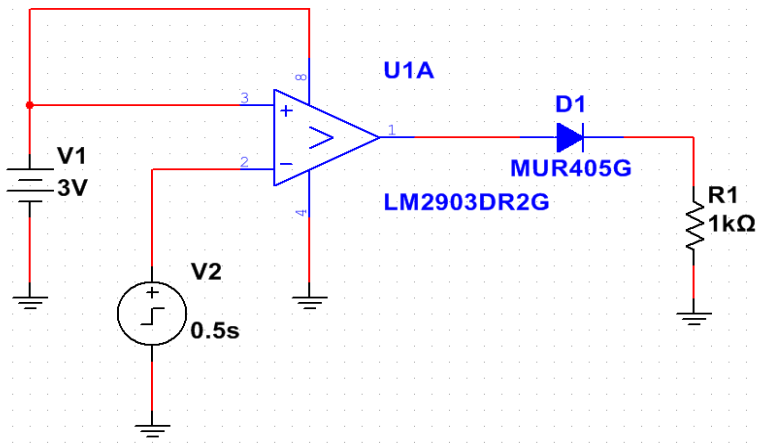

Figure 89 Simulation Schematic of Comparator Behaviour

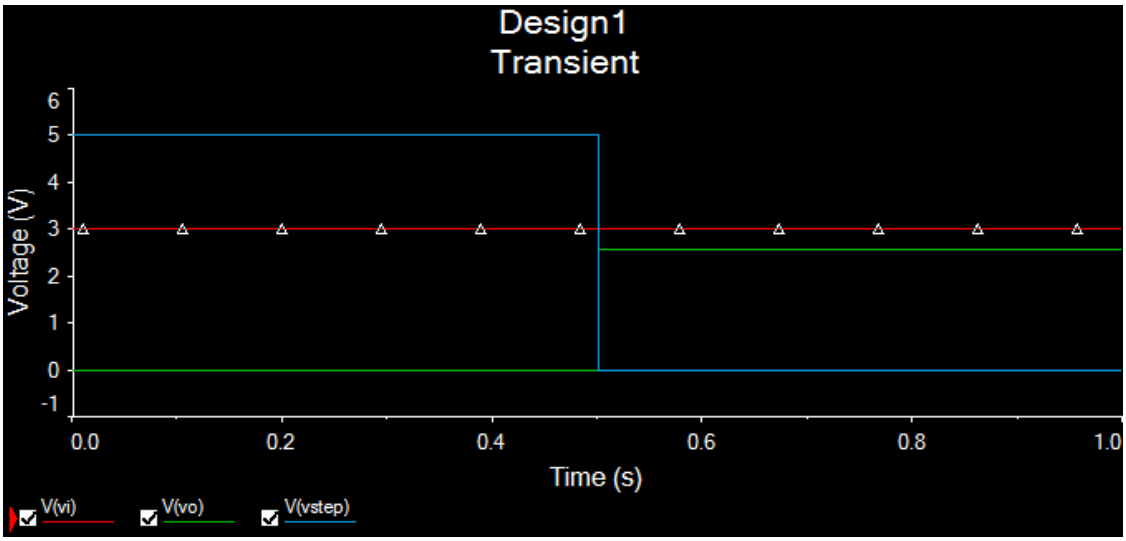

Figure 90 Simulation Result of Comparator Behaviour

The designed PCB is shown in *Figure 91*. For ease of timely manufacture and soldering in the School of Engineering and increased safety this, as well as all other boards designed this year, is a single copper layer solution utilising through hole components only. In addition to this, a Ground Plate was used to ease connections and to avoid interference from the rather long tracks. Dead copper was removed to avoid formation of unwanted antennas. The component Micro1 on the board provides space for the addition of an Arduino Micro microcontroller. Its use here is the monitoring of the supplied voltages through downscaling shunt regulators, which will aid in troubleshooting the system should failure occur. Future project iterations will further be able to utilise this device for enhanced power supply control mechanisms, potentially building on this PCB design by, for example, attempting a solution with multiple copper layers and surface mount components.

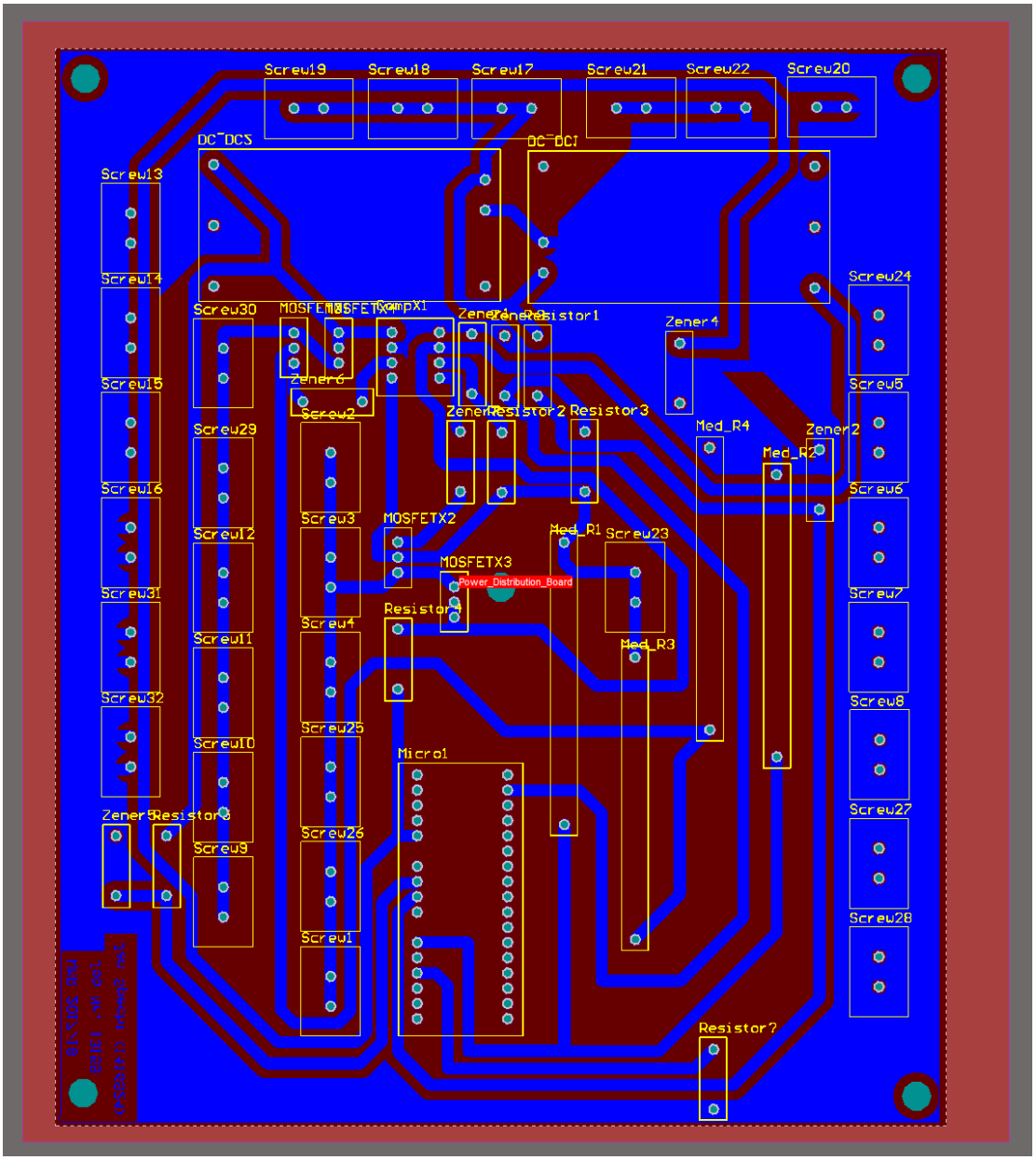

Figure 91 Power Distribution Board Footprint (15 cm × 18 cm)

9.2 Motor Control Interface Board

The robot tracks require two different motor controls. One for the main tracks, where mainly speed control is a requirement and one for the motors in the flippers, where position control is more crucial. Due to their price, motor position measurement will be achieved through Hall Effect encoders, whilst the motor control is carried out through a PWM output from the FPGA board, controllable from the base station.

The chosen motor controllers are, as mentioned above, the AX3500 by RoboteQ, due to budgetary restrictions. These will be run in what the instruction manual describes as the "Analog Input Mode" (RoboteQ, 2007). Here the motor controller receives an input voltage between 0 (for maximum reverse speed) and 5 V (for maximum forward speed) from a DB-15 style RS-

232 connector and a similar input from the motor encoders. A challenge arising here is that the chosen FPGA platform can only provide digital PWM signals of about 3 to 3.3 V magnitude, at frequencies up to 450 MHz (Digilent, 2016), as can the encoders, but at lower frequencies. This problem is overcome by integration of the PWM wave through a non-inverting low-pass filter with a gain of 1.5, as laid out in *Figure 92*.

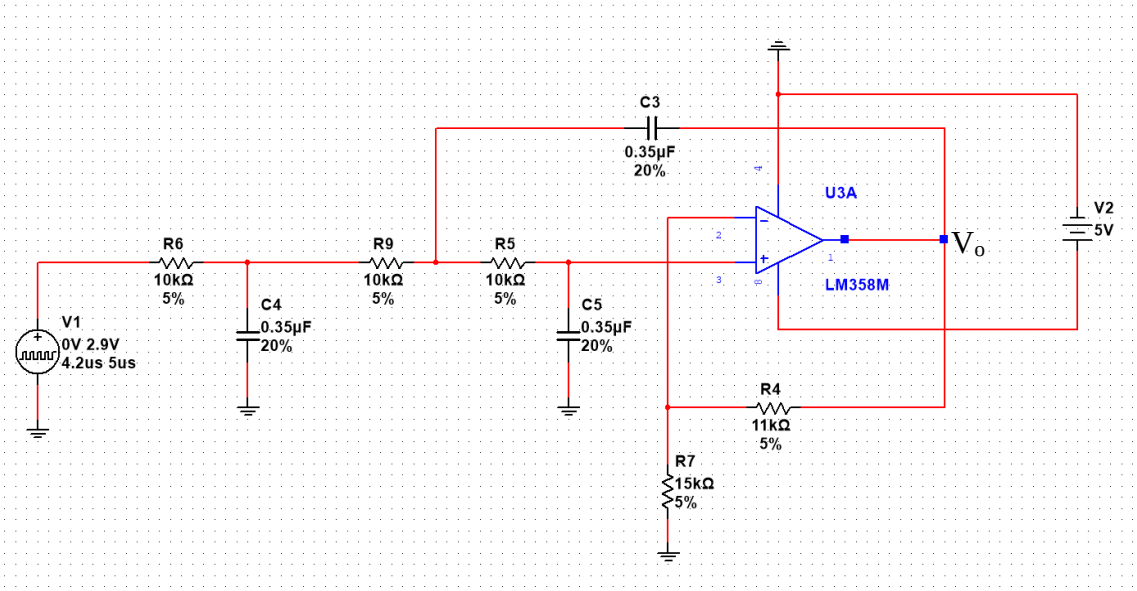

Figure 92 3rd Order Low-Pass Filter with a Gain of 1.5 and a Cut-off frequency of 200 MHz Simulation Circuit

This circuit has a cut-off frequency of 200 MHz and was simulated at different PWM frequencies up to an order of magnitude below that. This can be seen in *Figure 93*, where the input PWM wave (red) has a frequency of 200 kHz and a duty cycle of 98 percent, giving a continuous (green) output of $0.98 \times 1.5 \times 2.9\,V \approx 4.26\,V$.

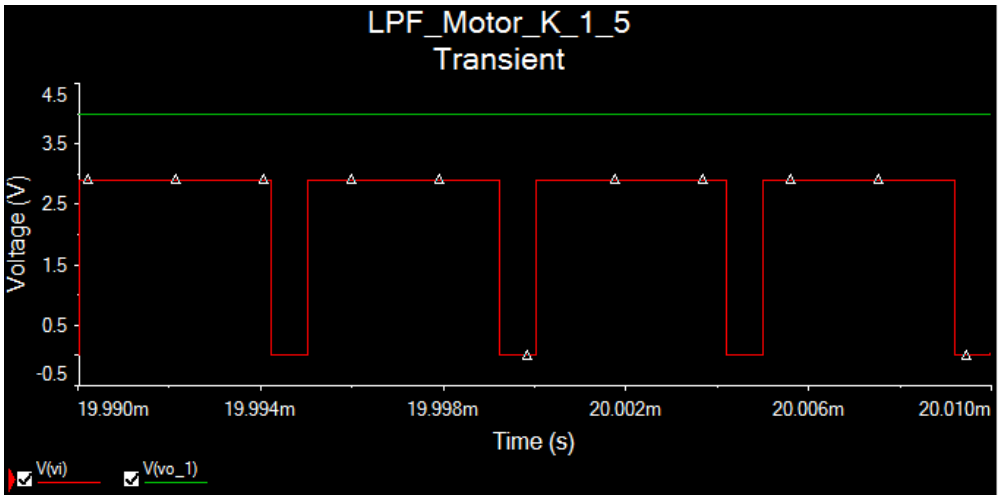

Figure 93 Simulation result of square wave integrator

In the next step a PCB was designed with similar design considerations to the power distribution board regarding the layering, the PCB footprint for this is depicted in *Figure 94*.

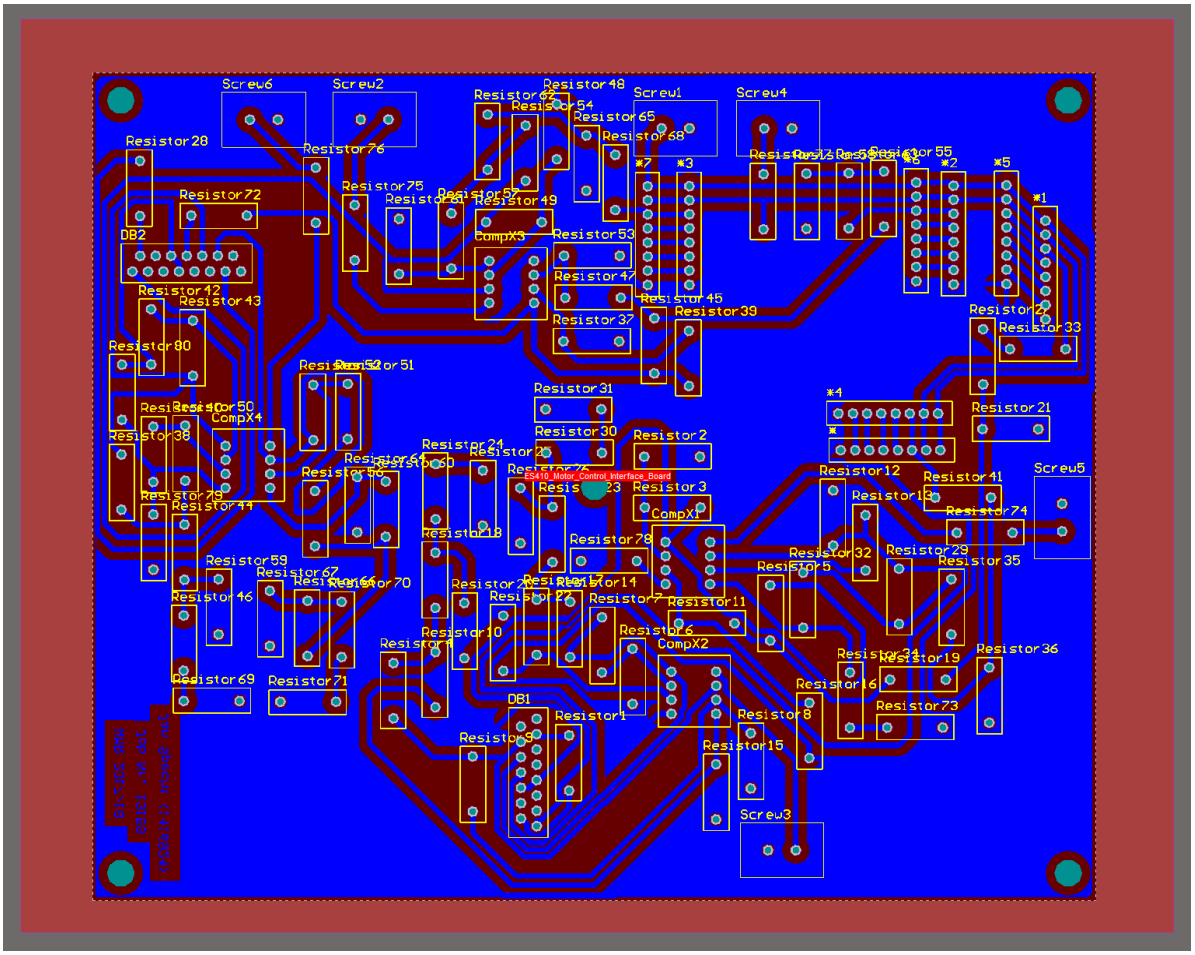

Figure 94 Motor Control Interface Board Footprint (15 cm × 18 cm)

This PCB is capable of delivering encoder and motor control signals to two AX3500 motor controllers, controlling up to 4 motors, whilst also feeding back the encoder signal as a 16-digit binary number (RoboteQ, 2007). The robot arm also requires control for six to eight motors, however some of these can be controlled of the same PWM signal. As the motor controllers for the arm are also AX3500 models, the same PCB will be used here.

9.3 Battery Management System

For safety reasons it is essential to monitor the individual cells of the Lithium Polymer batteries (Widayat et al., 2015). The key challenge here is the design of the BMS for high current spikes and potentially high continuous currents. A cost-effective solution for this issue is provided by the Battery Management PCB in *Figure 95*. This scales all cell voltages into a zero to five-volt range by using voltage dividers (with sufficiently high resistances for current protection). These voltages are the measured using an Arduino Micro microcontroller. Should the voltage of any

cell fall below a certain threshold, a signal is sent to a Gate-Drive IC, which controls the gates of two high-current n-type MOSFETs with insulated heat sinks and switches them off, whilst turning an LED on. The drain and source of these MOSFETs is connected directly to a cable capable of supporting the current drawn from the battery at all times, since this current is too high for a standard PCB. The battery management system is powered from a separate USB power supply.

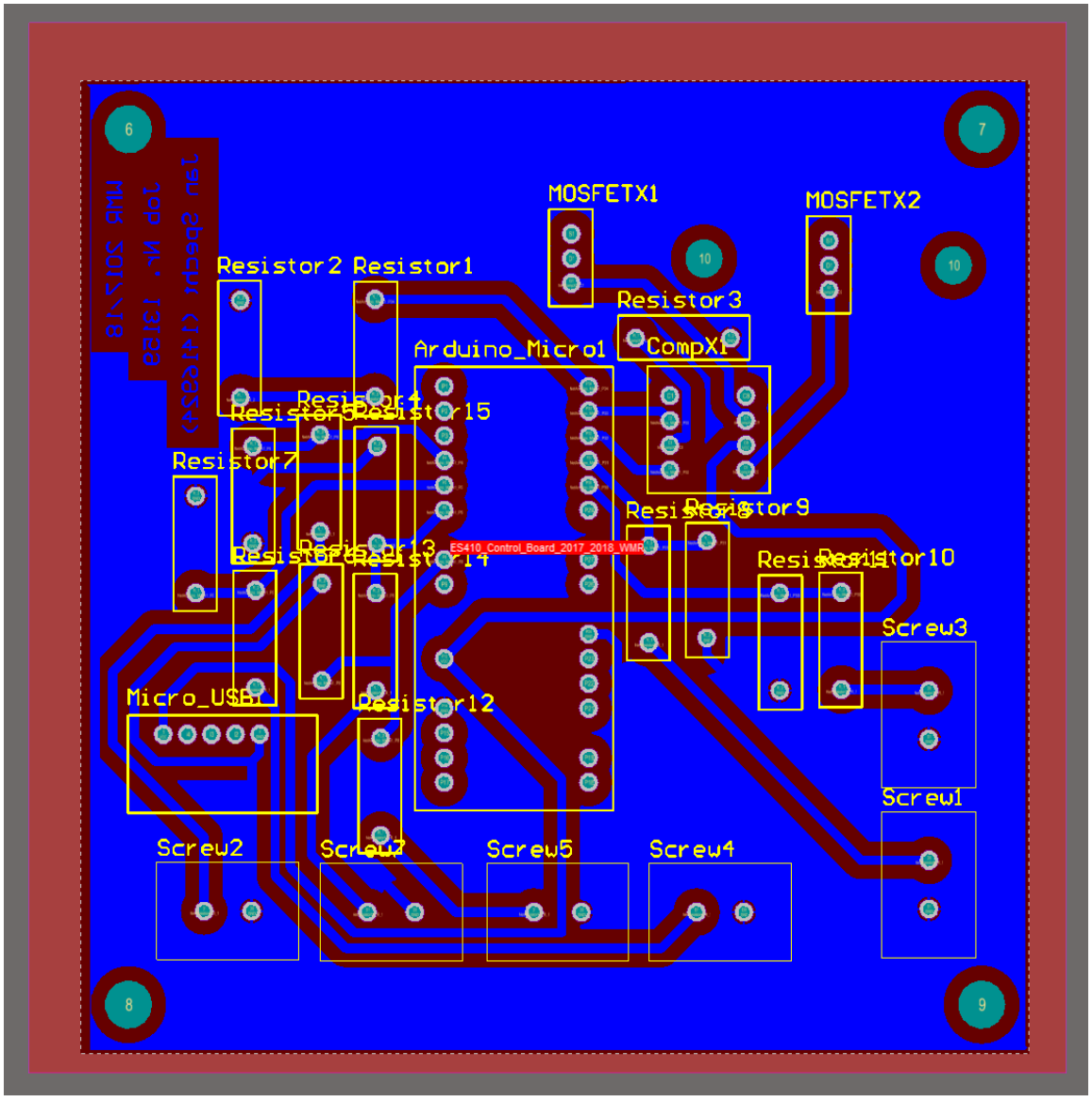

Figure 95 Battery Management System Board Footprint (10 cm × 10 cm)

9.4 Instrumentation Board

The robot is equipped with an electrochemical CO_2 sensor, which requires calibration. The sensor, purchased in a previous project iteration, is mounted onto a breakout board that is screwed onto the instrumentation PCB depicted in *Figure 96*. The output from the breakout board can be read from an analogue, as well as a digital output. The analogue output is further fed into an Analogue-to-Digital converter IC on the instrumentation PCB, to provide an additional option. Furthermore, the board has an integrated temperature sensor, with a digital I2C or SPI output. Connections for a digital MEMS microphone breakout board are also included. It was decided to have the microphone mounted onto a breakout board, since this will facilitate close connection to the robot's outside for better reception of voice signals. Due to the robot's size the space taken up by the PCB designs was not a primary design consideration several additional pin holes, as well as the possibility to connect an additional Arduino Micro were added. These can be exploited to add additional sensing, communication or control capabilities to the robot, for example it may come to be of benefit to have a microcontroller close to the arm, when wiring its motor controllers.

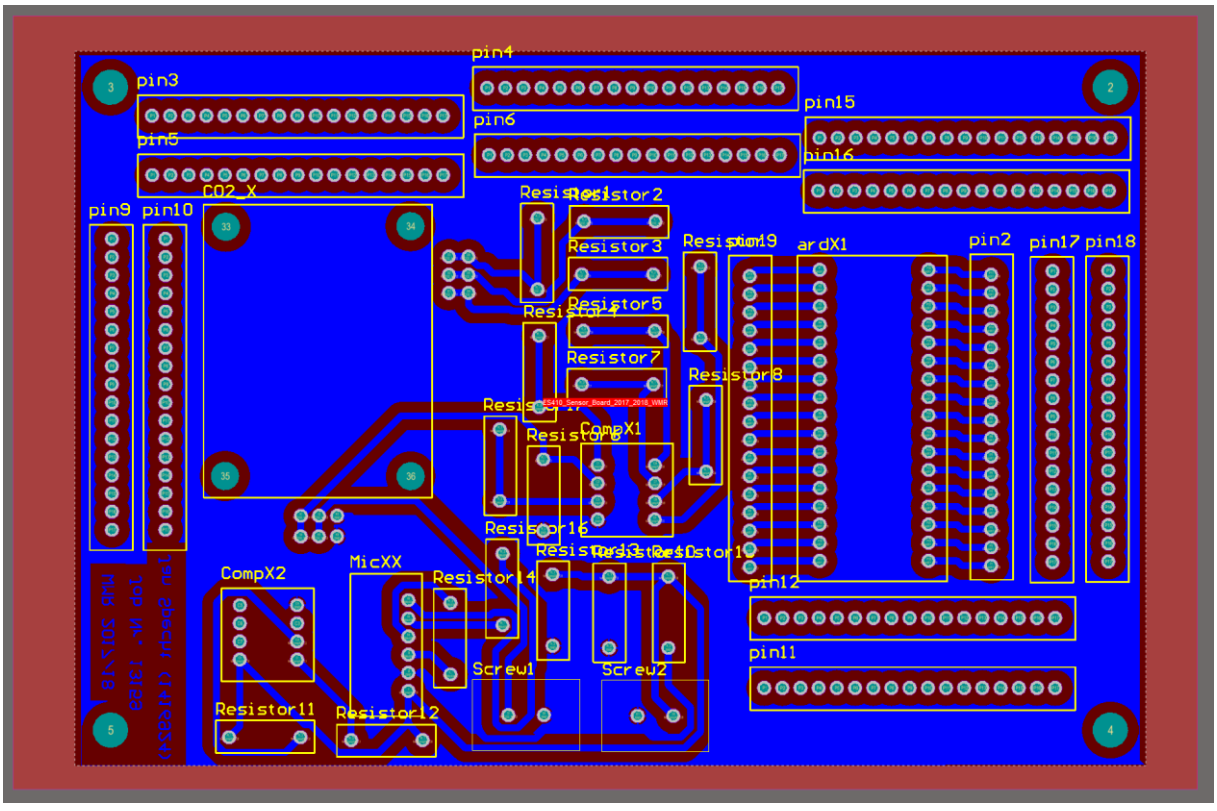

Figure 96 Instrumentation Board Footprint (15 cm × 10 cm)

The instrumentation PCB will be mounted onto the top of the robot and all connections to the FPGA board will be made through wires. This will simplify disconnection if needed, as well as potential re-use of components in future years.

10.0 3D Infrastructure

10.1 Electronics Tray

Due to the volume of electronic parts that are being produced and need to be mounted this year the need arose for an easy way of storing and accessing the boards. The initial concept was to screw the boards together using the corner fixings to keep them secure, however this would make it difficult to access one board at a time without unscrewing them all. This is important as during the competition teams need to be able to access the electronics to assess and determine the root cause of any issues in a short space of time, so ease and simplicity is essential.

Figure 97. Initial concept for electronics tray

Figure 97 shows the initial concept for the electronics tray, the shelving encompasses the idea to have the electronics tray capable of interchange and so be very multifunctional and adaptable by future project groups. The electronics tray will be 3D printed to make the most of the technologies available within the WMG facilities.

The electronics that need to be encased have been manufactured and their sizes are shown in the table below.

Battery Management System x 2	100 x 100 mm
FPGA	180 x 150 mm
Power Regulation Board x 2	150 x 180 mm

This shows that the initial idea of a single size box would not be the most practical solution with such a large difference in board size. It was discussed that the electronics would heat up and so forced ventilation would be required. *Figure 98* shows the concept for the tray with space on either side to fit two fans.

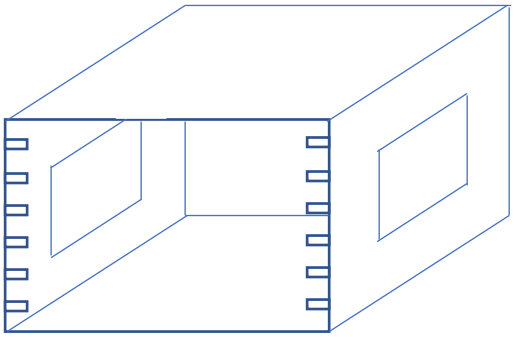

Figure 98. Hand sketch of electronics tray with fans

The fans were to be placed on either side of the box to allow for air to be drawn across to induce cooling on the electronic components. *Figure 99* shows the available space inside the robots main shell. This space will also need to house the batteries, and so to maximise space and allow accessibility the electronics will be placed on the upper shelf and the batteries within the lower section.

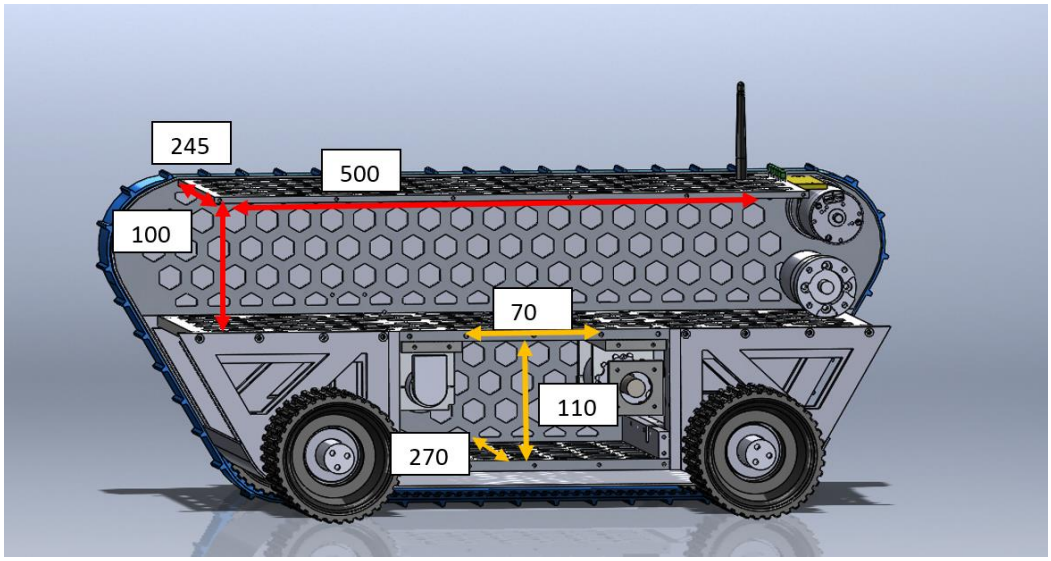

Figure 99. Internal dimensions of the mechanical chassis

Figure 99 shows the internal dimensions of the upper shelf to be 100mm in height, this is an issue as the current fans, Mouser San Ace 120 Low Power Consumption Fan, are 120 x 120 mm. This caused the design to alter again, *Figure 100*, with the fans being placed above and below the electronics box. This placement would cause further redesign of the mechanical chassis as exposed cut outs will be required to stop the fans from overheating, and so the idea of fan placement became another issue.

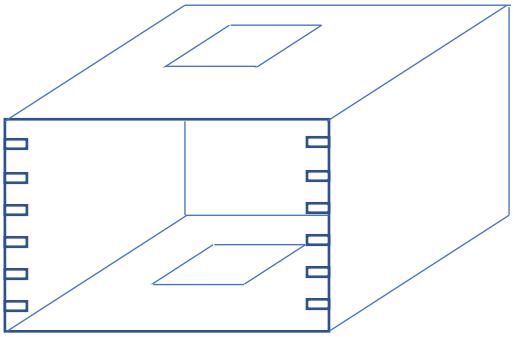

Figure 100. Tray with top/bottom fan location

As discussed in the cladding section it was decided the fans would be mounted in the external cladding either side of the bottom shelf to force air around the battery section on the lower shelf of the chassis. Therefore the fans no longer needed to be accounted for within the tray design.

Each board needs 3cm clearance to allow for wires and all fixings to be attached. This accompanied by the two different sizings of the boards means two trays are required. The same design with cut outs along each edge will be implemented into both to allow for the boards to be easily accessible with wiring from components elsewhere in the chassis. The trays will be closed at one end only with the end closest to the front of the robot being open to allow for easy access as this is where the opening in the external cladding is. There is a slot along each shelf output allowing the boards to be placed within these, this will limit any vertical movement that may occur as the robot moves. A lid is not practical in these cases due to the limited space inside the chassis. Therefore it was decided on a turning pin at the end to prevent the boards from sliding out whilst also taking up the minimum amount of space.

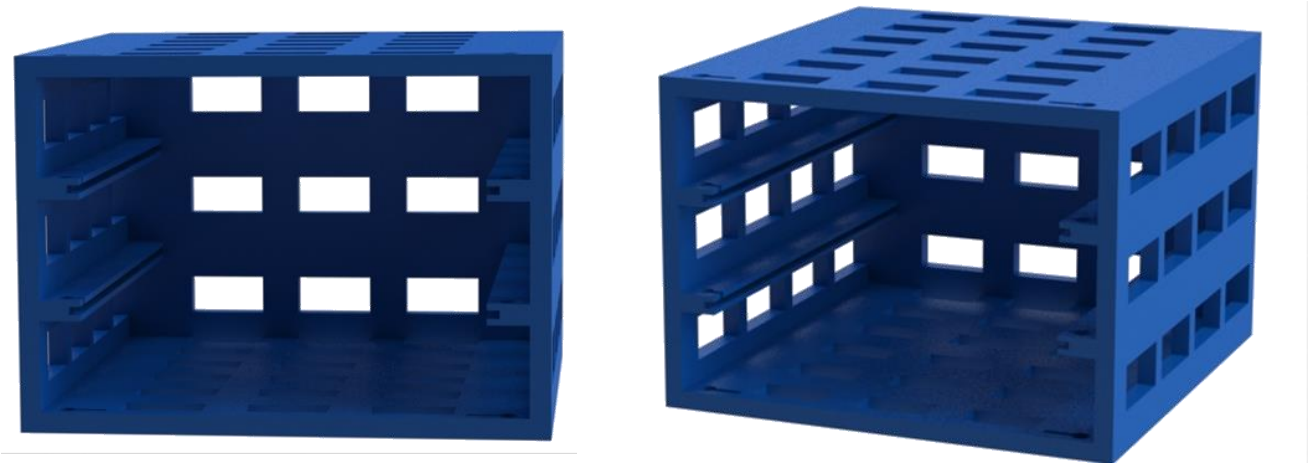

Figure 101. Renders of the 100 x 100 mm electronics tray

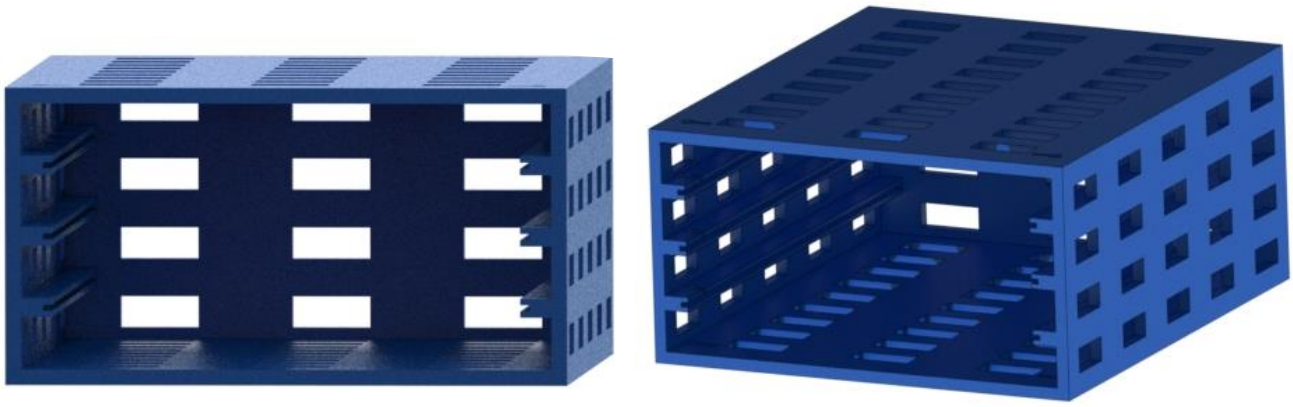

Figure 103. Renders of the 180 x150 mm electronics tray SolidWorks model

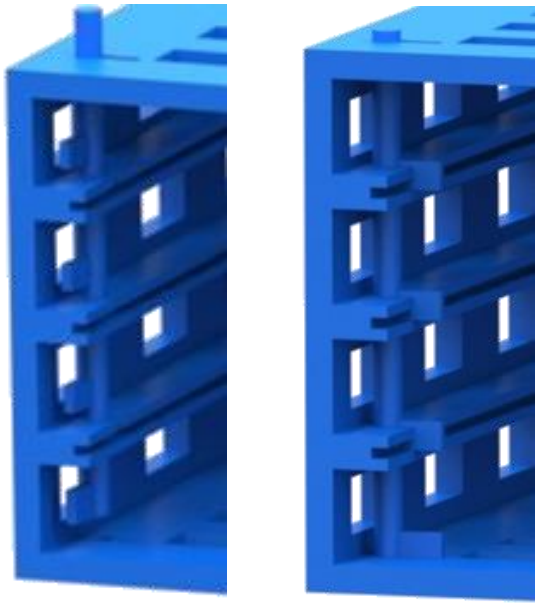

Figure 102. Close up render showing the key rotating to lock and free the boards' position

Figure 101 and *Figure 103* show the finalised designs for the two electronic boxes, to fit the respective boards in. *Figure 102* shows how the key slot works to hold the boards in, it can rotate to free the boards and lock in place. For technical drawings of all these parts see 17.0 Technical Drawings.

10.2 Sensor Box

The only functioning sensor on the Atlas robot from the 16/17 team was the LIDAR and this was just bolted on top of the cladding. This year a focus for the electrical sub-team has been to design and make all the internal electronics and sensors. Atlas is primarily a search and rescue robot, this requires sensors to provide basic functionality. The sensors include a CO_2 sensor, microphone and camera capable of providing visuals back to the base computer. These all need to be controlled and due to their position on the outside of the robots shell the PCB board controlling these is to be placed externally.

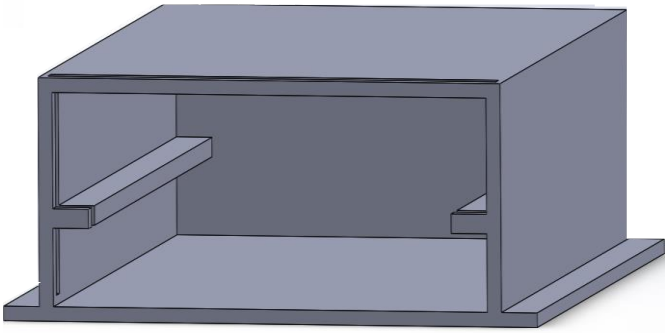

Figure 104. Initial SolidWorks model of the sensor box

The sensor board is physically 100 x 150 mm but it will also require clearance to allow for wiring of 30 mm so the initial design, *Figure 104*, was created**.** The tray is enclosed by a sliding screen as it will be exposed to the elements, the material will be 3D printed again.

After further analysis, the design was improved to allow for the selected CO_2 sensor to protrude from the top of the box, from the circular hole on the roof. The design has a cut out shown near the open end to allow for a sliding edge to be added to seal the box but still let it be accessible. The holes cut out in the base of the box allow for the wiring and connections to enter the box without causing any unnecessary exposure to the elements, especially when considering the environments the robot will be entering. The slot along the shelf allows the board to slide in stopping any vertical movement which slopes may cause.

Figure 105. Renders of final design for the sensor box, colour change for visibility

This design in Figure 105 is the final design, see 17.0 Technical Drawings for drawings

10. 3 Bus Bar Box

A bus bar, made from copper has been bought and will be placed along the centre of the robot. The purpose of this is to conduct the high current along and to be connected to the electronic parts. Due to the nature of this it should be encased to protect it from discharging onto the chassis. A bus bar box will be created, needing a removable lid for access and holes on each side to allow for connections to be made.

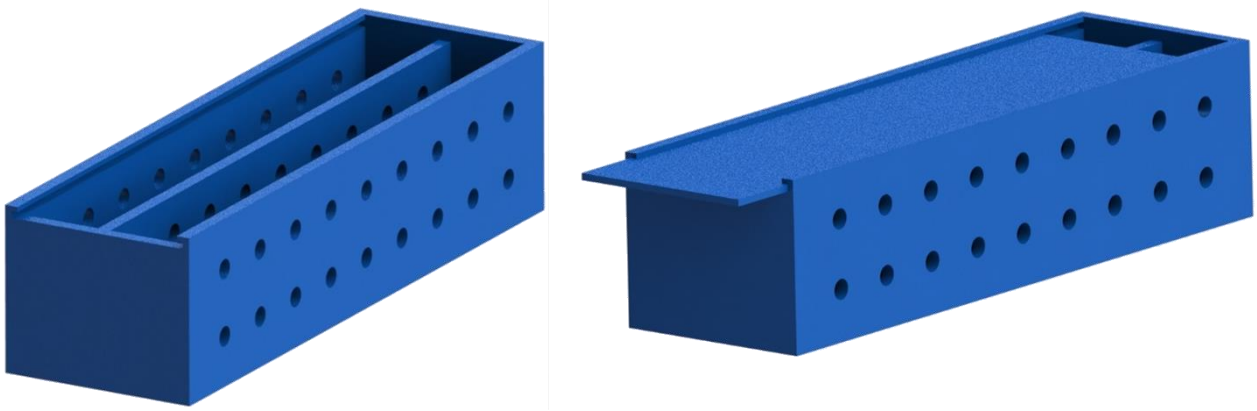

Figure 107. Renders of complete bus bar box showing sliding lid

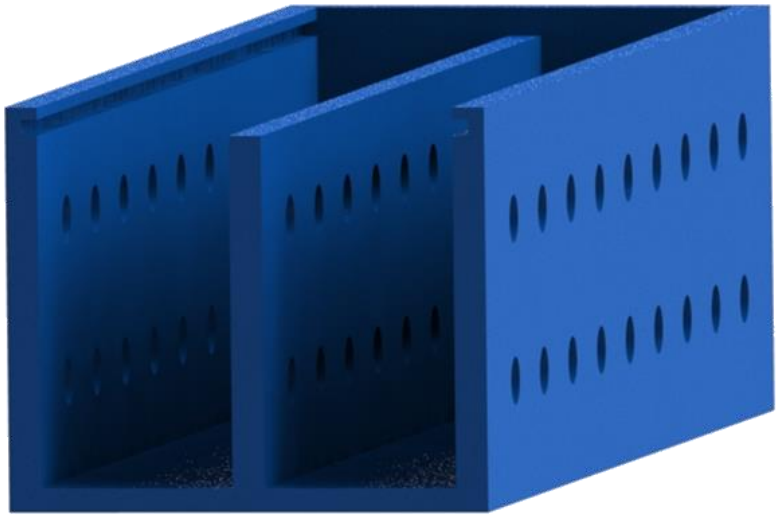

Figure 106. Section through box showing central split and holes

All three of these trays will be 3D printed in WMG the .igs files have been sent to the technicians and checked that they are ready to be produced. 3D printing was chosen as the parts can be made quickly and robustly in house. This was chosen as it is strong enough whilst being light and sturdy.

11.0 Field-Programmable Gate Array Board

11.1 FPGA System Design

It was decided to control the motors from a Field-Programmable Gate Array (FPGA) Board, namely the Nexys 4 DDR board by Digilent, since FPGAs are very flexible devices, capable of running multiple instructions and modules simultaneously, as opposed to microcontrollers, like Arduino devices, which generally execute commands consecutively. Another reason for this decision is that this project is likely to be continued in future years and since "ES3B2 Digital Systems Design" is a core third year Electronic Engineering module where students are taught Verilog with the Nexys 4 DDR board, it is believed that using the same board for the fourth-year project will simplify project handover. Furthermore, the chosen FPGA board already has a triple axis accelerometer for speed monitoring and safety of the electronic system, a micro-SD card slot for simple data storage, an ethernet port, an analogue-to-digital converter, a 3.5 mm audio output port allowing playback of audio signals, a thermometer for internal robot temperature monitoring, as well as a number of general purpose I/Os.

11.2 FPGA Modules

The system design on the FPGA is made up of four main modules, executing simultaneously. The "Top Module" serves as the connection between the input from the wireless signal and the instrumentation and motors, see *Figure 108*.

The "Wifi Module" takes the input from the Ethernet port through a "Microblaze" server and distributes it to the other modules as needed.

The "Sensor Module" takes six inputs. T1 is the register used to store the measurements taken with the temperature sensor on the instrumentation board, CO2 stores the CO_2 measurements and S1 the signal from the microphone. Furthermore, S2 is the sound signal sent to a speaker connected to the FPGA board's 3.5 mm audio port. The on-board sensors, connected to T2 (temperature) and A2 (acceleration) are used to monitor the internal system temperature and security. All readings are fed back to the operator through the wireless router connected to the FPGA board's ethernet port.

The "Motor Control Module" receives signals for each motor that is to be driven. Depending on these inputs, PWM waves are generated simultaneously for each motor. These will then be integrated as outlined above. The encoder values received from the motor controllers are sent to the operator, who interprets them and decides how the drive mode is to be altered accordingly.

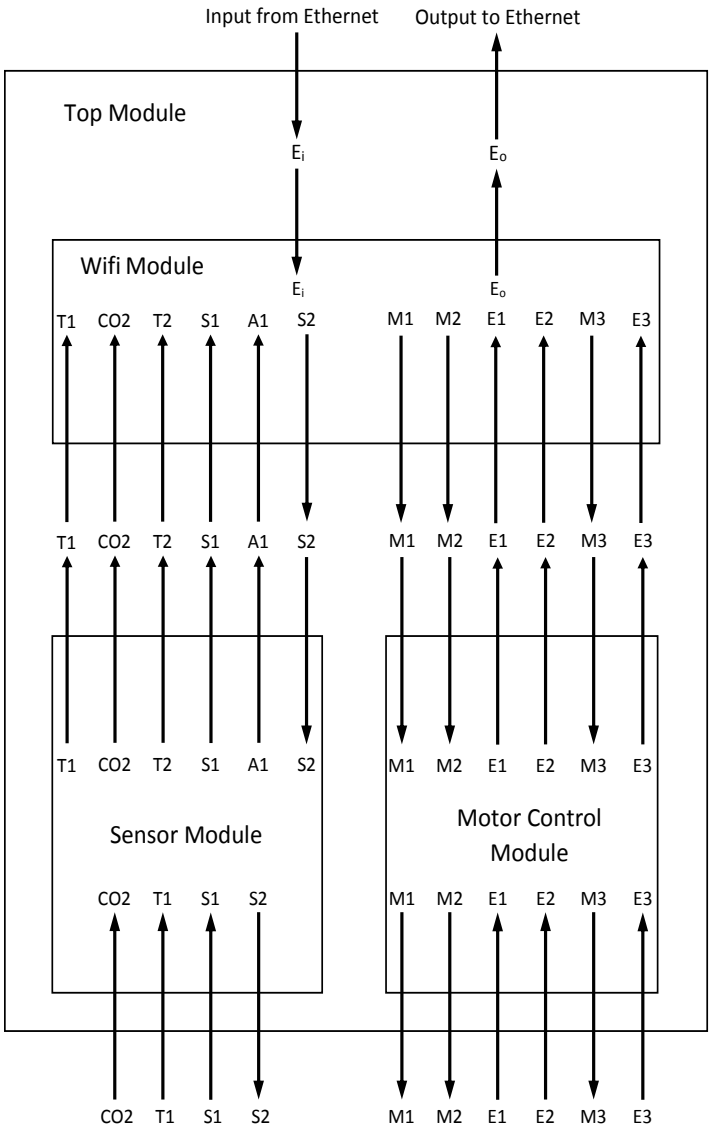

Figure 108 Block Diagram of FPGA Modules

11.3 Ambient Temperature Considerations

Since the robot is a search and rescue robot, it is supposed to be operable in extreme environments and thus sometimes extreme temperature conditions. It is well known that batteries tend to have varying performance, depending on ambient temperature conditions. This gives further importance to an already existing trade-off between battery life and robot weight. Generally, it would be possible to find a solution to maintain constant battery temperature, but this would often either utilise battery power, add additional weight or incur significant cost for additional components. The weight considerations alone essentially disqualify this solution, due to the strict limits set by the RoboCup competition the robot is designed for.

Given the constraints above, the decision was made to develop a battery-life preservation algorithm. A general outline of this is shown in *Figure 109*. The temperature inside the robot is

presumed to be the ambient temperature of the batteries. Thus, the internal temperature measurement from the temperature sensor on the Nexsy4 DDR board is used to compare the internal temperature to predetermined threshold temperatures deviating from an ambient temperature range beyond which battery life begins to suffer. Should the temperature be outside this range, the battery-life preservation mechanism will switch on. The motor control signal will then be decreased, leading to a decreasing motor torque and thus current drawn from the batteries, which will, on the one hand, slow the robot down, but prevent the battery from running out uncontrolledly.

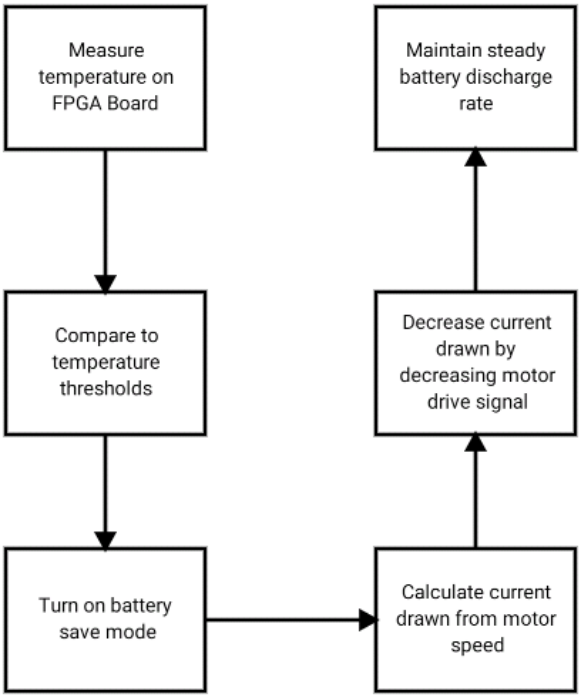

Figure 109 Block Diagram of Battery Life Preservation System

11.4 Pico-computer Software

The pico-computer will primarily control high data rate sensors and will thus primarily complete data processing and transmission functions. These are a Xsens MTI inertial measuring unit (IMU), a Hokuyo UTM-30LX LIDAR and potentially a thermal camera.

Figure 4 below shows a flow chart of the pico-computer software. The software will contain a mixture of new bespoke code as well as community produced code libraries. The following code packages will be adapted to facilitate the fast and robust development of the pico-computer software:

- Initialisation – robot_upstart (Purvis, 2016).
- IMU– xsens_driver (Colas, 2016).
- LIDAR management and processing – hector_mapping (Kohlbrecher, 2016).
- QR code detection – axis_camera (Gariepy, 2015) and visp_auto_tracker (Novotny, 2016).

These packages were chosen in terms of functionality, popularity and with regards to whether they are actively supported by the ROS community. Popularity was used as a proxy metric for code library robustness as it shows that other robotics practitioners have successfully utilised it.

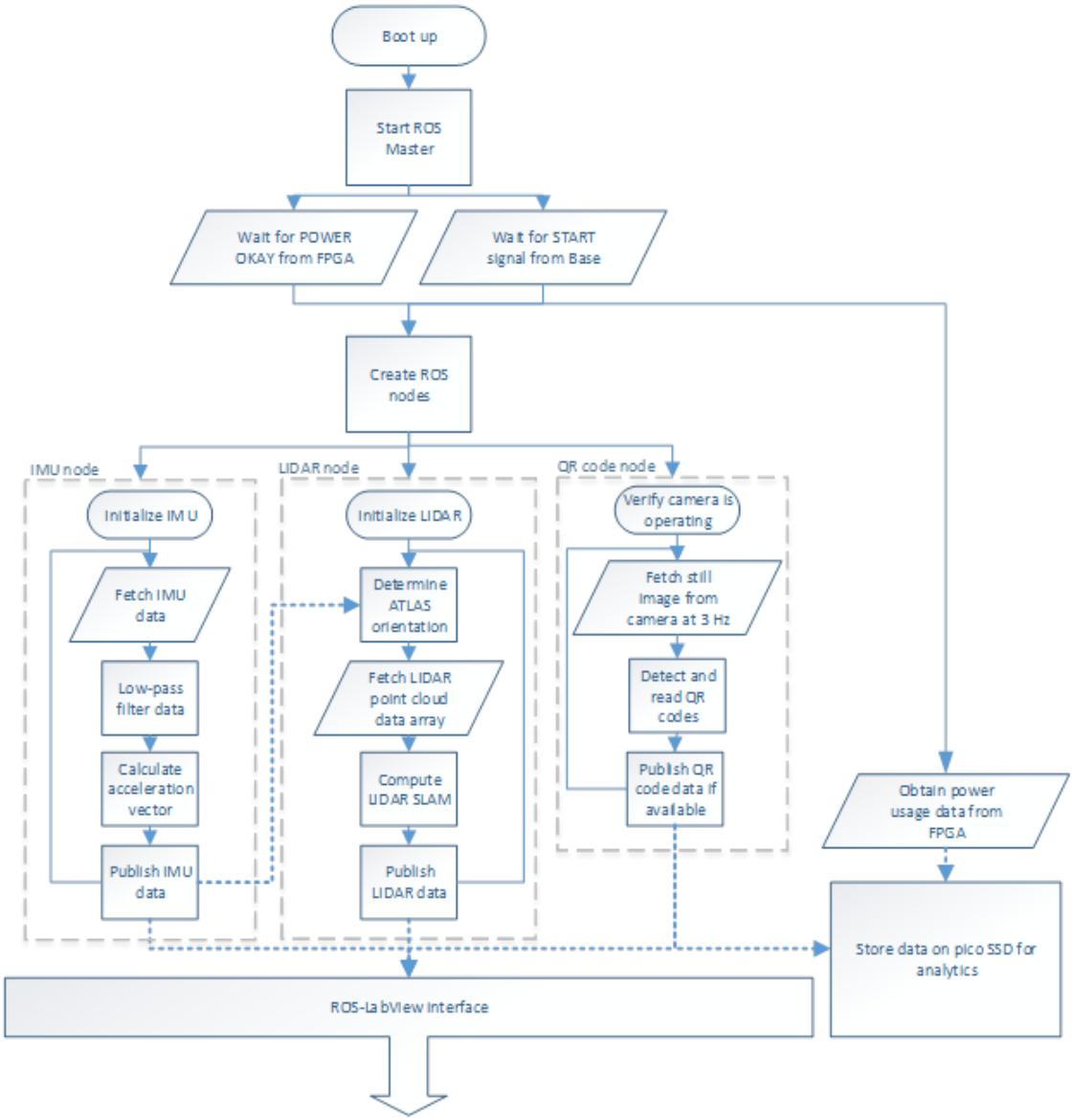

Figure 110 Flowchart of the pico-computer software.

The pico-computer software is made up of 3 sections: the start-up sequence, the data collection nodes and the ROS-LabView interface.

The start-up sequence will be executed automatically upon pico-computer boot up. First the ROS Master is launched and configured, after which the pico-computer goes into standby mode until it receives a conformation signal from the base station.

Next the pico-software executes three ROS nodes that fulfil the main requirements of the pico-computer system. These nodes execute in parallel and manage the interfacing of the pico-computer and the sensors. They also manage the processing of the data from these sensors which they then publish onto the required topics. Next, at the base-station, the ROS-LabView interface decodes the sensor data transmitted on ROS topics into data formats that are accessible to the base-station software. Concurrently, data from the pico-computer sensors and battery usage data obtained from the FPGA, are stored onto the pico-computer SSD (solid state drive). This data is stored, so that in-case of a system failure, diagnostics may be run to identify the cause of the failure.

The IMU node helps determine the orientation of Atlas by measuring the downwards pointing gravitational acceleration vector. First raw acceleration data is obtained from the IMU; this data will likely be contaminated by high frequency vibrations due to the motion of the robot. Next the data is digitally low-pass filtered, which removes some of the vibration induced accelerations. Finally the acceleration vector can be calculated which can be used to find the direction gravity is pointing. The IMU data feeds into the LIDAR node. The UTM-30LX LIDAR can record measurements in a 2D plane, it requires orientation data from the IMU so it knows what plain it is measuring in. The IMU data will be used to create a 2D map of Atlases environment using simultaneous localization and mapping (SLAM) which will aid an operator in understanding the layout of the robots surroundings. The 'QR code' node will be obtaining still images from the Axis camera at a low frame rate of 3 Hz. A low frame rate is used to conserve communications bandwidth. It will then run a QR code detection algorithm on the images and if available it will publish the QR code data in the form of a string. This task is completed to fulfil the requirements of the RoboCup Rescue League competition.

.

12.0 Camera System

The robot's on-board camera is the primary instrument through which an operator can assess the robot's surroundings. Ideally the on-board camera provides an operator a high-quality image of a wide view angle of its surroundings at a high speed.

The chosen camera is the Axis M1054, see *Figure 111*.

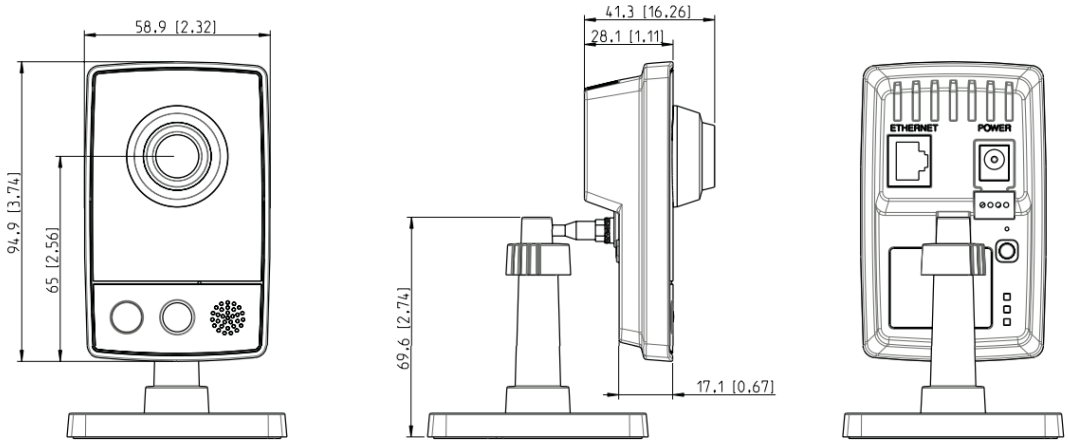

Figure 111 Axis M1054 Canera (Axis Communications AB., 2014)

This camera was bought by a group in previous years, which is the main reason for its choice. It allows for direct connection to the wireless router, has on-board compression and permits simple access to the live video stream. The camera stream will further be fed into the pico-computer, to enable the robot to detect QR codes as per the competition guidelines.

13.0 Communications System:

As shown in *Figure 110* the robot will be controlled by a remote operator. This can be accomplished by using either a wireless or a wired communications link between the robot and the base station. Because of the increased robot mobility of wireless communications, it was decided to operate the robot via a wireless communications link. Wired communications could potentially simplify power supply to the robot, but since Lithium Polymer batteries were already available for use this was not a key decision factor.

Because of this a crude estimate of transmission rate requirements was made according to *Table 5*, based on common data rates for any components that require data transmissions of some form and assuming all of these components require continuous network communications.

Data source	**Bandwidth (Mbps)**
Front camera	5.00
Rear camera	5.00
LIDAR	2.00
Microphone	0.20
IMU	0.02
Motor controls	0.05
Motor encoders	0.05
Temperature & CO2 Sensors	0.01
Total	**12.10**

Table 5 Estimation of the bandwidth required for the Atlas communication system (Google LLC, 2018) (Hokuyo Automatic co. LTD. 2012) (Labbe, 2017) (Keller, 2012)

As can be seen from *Table 5*, communications will require roughly a 12 Mbps data rate, to ensure smooth communications it was decided that transmission should, at the very least, be capable of 20 Mbps communications. This is a data rate that can be supported by most current wireless Wi-Fi routers and PCs, but not by Bluetooth and whilst using cellular communications would offer an extended communication range the decision ultimately fell to Wi-Fi, due to its cost advantage.

The chosen wireless router is the D-Link DWR 118, since this is available to the group without need for purchase and fulfils range and data transmission rate requirements. The router will be

positioned just underneath the top cover of the robot, to allow antenna assembly outside its shell to avoid electromagnetic shielding. The WLAN network of Atlas will use the IEEE 802.11n standard which offers a good balance between network range and bandwidth (Abdelrahman, 2015).

As mentioned previously the robot is controlled through a Nexys4 DDR FPGA board, as well as an Axiomtek Pico-842 pico-computer purchased by a previous WMR group, since using a pico-computer simplifies the use of camera, IMU and LIDAR equipment through the availability of software drivers and libraries which the FPGA board cannot take advantage of to the same extent, since it does not readily support Robot-Operating-System. ROS is a largely open-source software environment that supports multiple programming languages and for which there are pre-made software libraries, which accelerate software development.

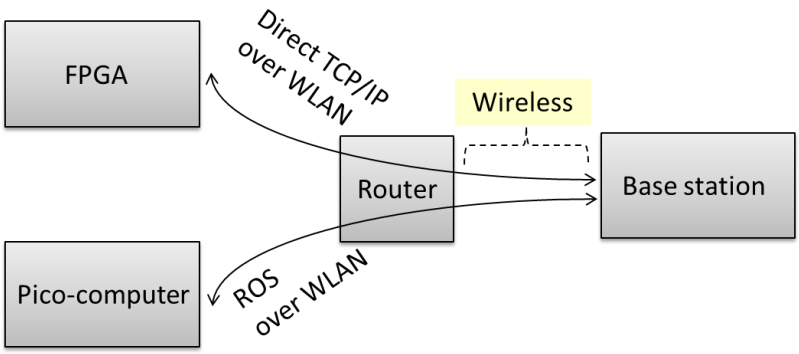

Figure 112. The final Atlas communications network

There are multiple options to establish wireless communication between the base station and the robot, the first being to interface both the FPGA board and the pico-computer directly in the WLAN network using TCP/IP, as shown in *Figure 112*. This solution has the benefit that it incorporates a 'direct' route between the two ends of the communication system making the communications link to each component the fastest possible in this implementation, however due to the nature of FPGA boards this is also the most design intensive. As the pico-computer already features an operating system, Ubuntu Linux 16.04 in this case, establishing a communications link is not difficult and to simplify the same to the FPGA board a "Microblaze" processor will be implemented on it, which allows for simplified access to the ethernet PHY on the Nexys4 DDR board and programming of the communications link in C, even though the majority of operations will still be set up through a Verilog design.

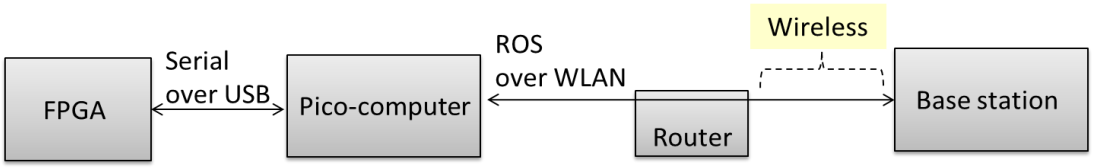

Figure 113. Suggestion for the Atlas communications network. This network is simple to implement in software.

Another possible approach is to use the pico-computer as a communications relay to the FPGA. The base station would simply transmit a message to the pico-computer via ROS and the pico-computer would relay the data to the FPGA via USB. The benefit of this method is ease of implementation with respect to the method outlined in *Figure 113*. The disadvantage of this technique is the increased latency between the base station and the FPGA board. Furthermore, it would reduce system redundancy due to the resulting interdependence of the pico-computer and the FPGA-board. If a fault occurs on the pico-computer then not only the cameras, but also the motor controllers monitored through the FPGA will be affected. Additionally, using this link wastefully utilises the pico-computer's processing power thus lowering the capacity to which it can service other devices on the robot.

14.0 Base Computer

14.1 Design for Base Computer

The base station, through which an operator controls Atlas Legacy, will use LabVIEW 2017 running on Windows 7 to interface and control Atlas, and also to visualise important data. LabVIEW is utilised to generate an efficient graphical user interface for the robot, which will allow an operator to control the robot through teleoperation. The base-station computer is a portable Elite book 850 G3 6th generation laptop.

14.1.1 LabVIEW

LabVIEW is a platform used for system design and development. It runs off the graphical language G and is commonly used for data acquisition and instruction control, making it suitable for controlling a robot. In addition, LabVIEW provides the ability to create a graphical user interface (GUI) with ease. These features make LabVIEW an attractive choice for developing the base-station software.

14.1.2 LabVIEW Blocks.

The block in *Figure 114* shows how a LabVIEW block can be created. These can then be connected together to produce a system and run in loop in the GUI and main run. *Figure 114* shows the input and output wire and seen as sub- system vi.

Figure 114 LabVIEW Block

14.2 GUI – Graphical User interface

A GUI facilitates a intuitive visual way of interacting with complex data coming, to and from, the base station. A GUI, rather than a text based interface, is essential in directly operating a complex system such as Atlas. This is one of the reasons why LabVIEW was picked as it enables the easy creation of a GUI.

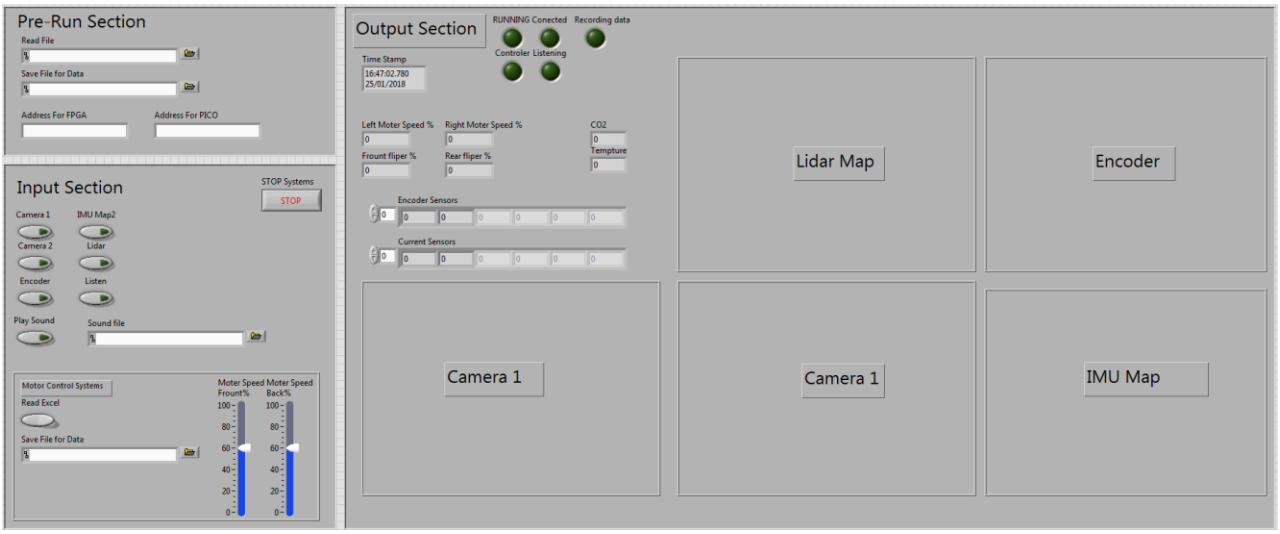

Figure 115 Image of the Graphical user interface.

Verilog

Table 6 shows the theory behind the connection system and control system for the robot and base computer.

Control systems.						
Theory						
Parts	Connections	Send Info	Receive info	Process info	GUI	Control code
Base	Base and Wi-Fi	Yes	Yes	Yes	Lab-VIEW	LabVIEW
PS3	Base	Yes	No	Yes	Lab-VIEW	DS3
FPGA	Wi-Fi Hub	Yes	Yes	Yes	Lab-VIEW	Verilog
Pico Com-puter	Wi-Fi Hub	Yes	Yes	Yes	Lab-VIEW	ROS
Wi-Fi Hub	FPGA and PC	Yes	Yes	No	Lab-VIEW	
Sensors						
CO2	FPGA	Yes	No	No	Lab-VIEW	Verilog
Tempter	FPGA	Yes	No	No	Lab-VIEW	Verilog
Lidar	Pico Computer	Yes	No	No	Lab-VIEW	ROS
IMU	Pico Computer	Yes	No	No	Lab-VIEW	ROS
Camera	Pico Computer	Yes	No	Yes	Lab-VIEW	ROS

Micro-phone	FPGA	Yes	No	No	Lab-VIEW	Verilog
Speaker	FPGA	Yes	No	No	Lab-VIEW	Verilog
Current sensors	FPGA	Yes	No	No	LabVIEW	Verilog
Motor En-coders	FPGA	Yes	No	No	Lab-VIEW	Verilog
Control-lers						
Motor Control-lers	FPGA	No	Yes	No	Lab-VIEW	Verilog

Table 6 Show the controlling system for each items

14.3 Address systems

LabVIEW is used to create an address system to communicate with the FPGA; and enable the latter to interpret wireless transmissions appropriately. The design of this is shown in the table below.

Address Systems for FPGA				
To Motor	**Which Motor Controls**	**Direction/ Which motor**	**Amount (Hex)**	**Example**
M	1 to 4	a,A, b,B	0 – 5.0	M1a5.0
Sensors	**Which sensors**	**On/OFF/ Sin-gle**	**Sample Rate in ms**	
S	1 to 4	O,F, S	0 - 999	S1O100
Microphone	**Save for number**	**On/OFF**	**Sample Rate in ms**	
N	1	O,F	0 - 999	M1F000
Speaker	**Number**	**On/OFF**	**Sample Rate in ms**	
A	1 to 3	O,F	0 - 999	A1O050
Encoder	**Number**	**Read**	**Position**	
E	1 to 4	R	0-360	E1R120

Table 7 Address system for FPGA

14.4 Base Computer Block Diagram

This block diagram shows how all incoming and outgoing data will be processed. *Table 8* shows the breakdown of each system, where multiple steps can be done in the code. The block diagram is shown in *Figure 116.*

Red	User input
Green	Process for output
Orange	Process for input
Blue	Movement for information

Table 8 understanding the coding structure block drawing

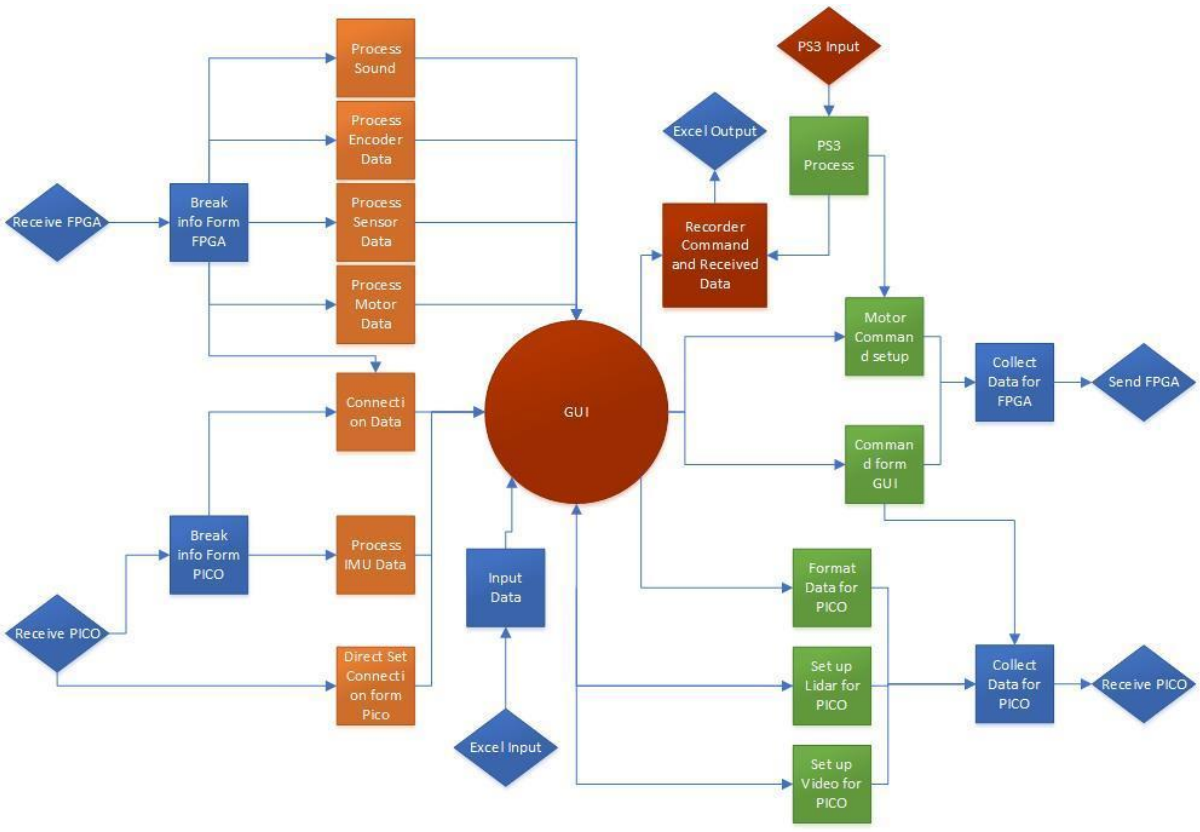

Figure 116 Block Diagram showing coding structure at Base Computer.

14.5 Base computer List of codes

The levels below show a breakdown of each sub section of code created and being created. *Table 9* shows the codes that are being developed and at what level they interact.

Level 1 – Human Interface

Level 2 – Machine interface or Outside LabVIEW.

Level 3 – No interface and with GUI input

Level 4 – No interface and without GUI input

Name	**Reason**	**Level**
Interfaces		
GUI	Human interfaces and display of information	1
PS4 interface	Set up interface with Ps4 controller	3
PS4 controller	Map the PS4 interface.	2
Motor Controllers		
Main motor control	Produce motor control code from PS4 controller	4
Flipper motor control	Produce motor control code from PS4 controller	4
Arm motor control	Produce motor control code from PS4 controller	4
Gripper motor control	Produce motor control code from PS4 controller	4
Tempter control motors	Produce motor control code from PS4 controller	4
Motor Control via Excel		
Read info from excel	Read values from the excel file	2
Process info from excel for controlling motor	Change value into motor code to send to FPGA	2
Save Data		
Process motor value	Turn the motor value to readable values	4
Save value to excel	Format and save the data to a csv	2
Encoders		
Read encoder	Receive the value of encoders form the FPGA	2

Processes encoder	Break up the encoder to the different values and process the data	4
Display the value encoders in graph and table.	Process and graph encoder data	3
Info Exchange		
Send FPGA	Send info and commands to FPGA	2
Read FPGA	Read info and decodes data from FPGA	2
Send pico	Send info and commands to pico	2
Read pico	Read info and decodes data from pico	2
Lidar		
Lidar control	Step up and control the lidar	3
Receiver lidar info	Get info from the pico	2
Process lidar values	Format the lidar data for display and dump into a .csv	4
Display lidar values.	Display the lidar data in a map	3
Camera		
Camera control	Step up and control the camera	2
Receiver video	Get information	2
Steam video	Set up stream info	3
Sound System		
Sound system control	Set up command system and control if sound operates	3
Load sound wave	Load the sound from a file	2
Send sound FPGA	Send sound wave to FPGA	2
Read microphones	Read the information form FPGA	2

Process microphones wave	Processing the information from microphones	4
Output sound wave at base station	Output from the speakers	3
Sensors		
Receiver Sensors	Receive information from the FPGA	2
Save sensors	Save the data and add to .csv file	
Display sensors	Display the sensor values	3
Others		
Command sender	Set up systems that can send commands from the base to the FPGA	2

Table 9 List code created by base computer

14.6 Code Structure

Repeating code

Having repeating code gives the ability to redo a loop and prioritise section refreshing, ie. A function can run for 100 loops whilst a secondary function of 10 steps will restart every 10 (0, 10, 20 etc). This allows for recurring functions to be executed at different rates. This process is demonstrated through the following steps:

- Produce a 100 loop function
- Function that does step of every x number
- This will then turn a case box on or off and then reset every 100 main loops

Basic structure

The basic structure of the code will be:

- Start-up code, setup the connection
- Run the repeating code section
- End the connection and send data with .csv for review later

There are two types of code that will be produced; primary and secondary.

Primary code → the primary code will be for the main motor and flipper control and basic PS4 control and connection to FPGA.

Secondary Code → the secondary code aims to control everything and show a full display of all functions possible for the robot.

Simultaneous Localization and Mapping (SLAM)

The SLAM system records the IMU data and Lidar, works out where current is flowing and the direction of movement can be mapped. From this a 3D map can be created of where the robot has gone, this then can be mapped on to the Lidar system producing a map of the environment and where the robot has been.

15.0 Testing and verification

In order to test and verify needed to create a system that will be able simulate and test the conditions the robot will go through during the RoboCup. Tests have also been designed to ensure all systems run as expected, and that any faults in design can be identified and resolved as soon as possible.

Testing will be done during the construction and operation phase of the project. The following plan will be printed off and placed in the workshop, with each action ticked off when completed.

15.1 Mechanical Testing subsystem testing

Testing Robot Arm

Steps	Inputs	Expected output	Achieved
1	Visual inspection of robotic arm parts.	Components match expected design and have no faults or damage.	
2	Measurement of all arm parts.	Components have correct dimensions.	
3	Assembly of parts.	Parts fit together as expected, all screws and bearings can be mounted as required.	
4	Testing of motors while mounted to arm.	Arm moves as expected and can be controlled as expected.	

Table 10 Robotic arm test

Testing the Battery mounting system.

Steps	Inputs	Expected output	Achieved
1	Visual inspection of battery mounting parts and changes.	Components match expected design and have no faults or damage.	
2	Measurement of all battery management parts and changes to parts.	Components have correct dimensions.	
3	Check the batteries fit correctly.	Battery fits within robot and is easily accessible within the robot.	
4	Mounting and assembly.	All parts can be successfully mounted and are safe in their mounting positions.	
5	Check electronic connections.	Electronic connections work and power board can be powered from battery through this.	
6	Quick removal testing in case of emergency.	Both battery cases can be removed by a single operator within 15 seconds.	

Table 11 Battery mounting test

Testing the Cladding

Steps	Inputs	Expected output	Achieved
1	Visual inspection of cladding parts.	Components match expected design and have no faults or damage.	
2	Check the holes and mounting cut-outs to ensure they align with body holes and battery mounting.	All parts align and allow cladding to be easily screwed into place.	
3	Checking battery mounting hinge and latch.	Latch and hinges work properly and can be opened efficiently.	

Table 12 Cladding test

Testing the Powertrain Design

Steps	Inputs	Expected output	Achieved
1	Visual inspection of powertrain parts.	Components match expected design and have no faults or damage.	
2	Measurement of all powertrain parts.	Components have correct dimensions.	
3	Checking fit and assembly of all parts.	Motors can be mounted and drive shaft aligns with bearings. Sprocket aligned with drive shaft sprocket.	
4	Check the mounting and fit of the powertrain assembly into the robot.	All screw points aligned and can be easily mounted.	
5	Breakable shaft test.	Shaft breaks at desired force to prevent damage to motor.	

Table 13 Powertrain design

Testing the Tensioning system

Steps	Inputs	Expected output	Achieved
1	Spring attachment to tensioning system.	Springs fit around connecting beams.	
2	Mounting test.	All parts can be easily mounted and tracks remain in place when tested.	
3	Slack testing	Tracks stay in place when going slack during operation, springs provide sufficient force and extension to keep tracks in place.	

Table 14 Tensioning Test

Testing the Sensors Box

Steps	Inputs	Expected output	Achieved
1	Visual inspection of sensor box parts.	Components match expected design and have no faults or damage.	
2	Measurement of sensor box parts.	Components have correct dimensions.	
3	Mounting of sensors.	Ensure all sensors fit within box as desired.	

Table 15 Sensors box test.

Testing the Electronics box

Steps	Inputs	Expected output	Achieved
1	Visual inspection of Electronics box parts	Components match expected design and have no faults or damage.	
2	Measurement of all battery management parts and changes	Components have correct dimensions.	
3	Mounting check.	Box is mounted in robot as expected.	
4	Connection and electronics mounting check.	All electronic components can be mounted as expected and all connections can be routed as required.	

Table 16 Electronics Box

Robot Construction

Steps	Inputs	Expected output	Achieved
1	All parts mounted correctly and in right place.	No parts left spare, all components are housed within robot as expected.	
2	All screw connections as desired.	No spare screws, all screws flush to surface.	
3	External mounting checks.	All external parts rigidly mounted, all screws flush to surface.	

Table 17 Construction Test

15.2 Electrical testing subsystems

Test – Testing PCB produced

Steps	Inputs	Expected output	Achieved
1	Motor control Interface Board, by visual inspection.	Board has been produced as per design, all components in place.	
2	Battery management system by visual inspection.	Board has been produced as per design, all components in place.	
3	Instrumentation board by visual inspection.	Board has been produced as per design, all components in place.	
4	Power distribution board by visual inspection.	Board has been produced as per design, all components in place.	
5	Motor control Interface Board, checking soldered points	All soldered points are clean	
6	Battery management system, checking soldered points.	All soldered points are clean	
7	Instrumentation board, checking soldered points.	All soldered points are clean	
8	Power distribution board, checking soldered points.	All soldered points are clean	
9	Motor control Interface Board, check all connections are passing current.	All wires and lines are connected.	
10	Battery management system, check all connections are passing current.	All wires and lines are connected.	
11	Instrumentation board, check all connections are passing current.	All wires and lines are connected.	
12	Power distribution board, check all connections are passing current.	All wires and lines are connected.	

13	Motor control Interface Board connected to FPGA.	Successful connection	
14	Battery management system, connected to FPGA	Successful connection	
15	Instrumentation board, connected to FPGA	Successful connection	
16	Power distribution board, connected to FPGA	Successful connection	
17	Motor control Interface Board, connection to external ports.	Clean connection.	
18	Battery management system connection to external ports.	Clean connection.	
19	Instrumentation board connection to external ports.	Clean connection.	
20	Power distribution board connection to external ports.	Clean connection.	

Table 18 PCB Produced Test

Testing the FPGA

Steps	**Inputs**	**Expected output**	**Achieved**
1	Visual inspection of FPGA	FPGA has no damage and all connections are as expected.	
2	Power supply to FPGA test.	FPGA is powered	
3	Plug in Computer	Interface can be programmed and produced successfully.	

Table 19 FPGA Test

Testing the Pico Computer

Steps	Inputs	Expected output	Achieved
1	Visual inspection of Pico Computer	Pico computer has no damage and is as expected.	
2	Power supply to Pico computer test.	Pico computer is powered.	
3	Plug in Computer	Interface can be programmed and produced successfully.	

Table 20 Pico Computer Test

Test Testing sensors, this computer $C0_2$, Tempter, Lidar

Steps	Inputs	Expected output	Achieved
1	Visual inspection of all sensors board	Board has no damaged and all parts are located and connected as desired.	
2	Test connection to each Sensor	All connections are working.	
3	Sensor response through instrumentation board.	Inputs to sensors provide desired output from boards.	

Table 21 sensors Boards Test

Testing Cameras

Steps	Inputs	Expected output	Achieved
1	Visual inspection of Two Cameras	Cameras have no damage and all connections are working.	
2	Cameras can be powered	Power light on Camera turns on.	
3	Cameras connected to Pico computer	Camera can send and receive signal.	
4	Camera connection to base computer.	Visual display shown on base computer.	

Table 22 Cameras Test

Testing Lidar

Steps	Inputs	Expected output	Achieved
1	Visual inspection of Lidar	Lidar have no damage and all connections are working.	
2	Lidar can be powered	Power light on Lidar turns on.	
3	Lidar connect to Pico computer.	Lidar can send and receive signal.	
4	Camera connection to base computer.	Visual display shown on base computer.	

Table 23 Lidar Test

Testing Wi-Fi systems

Steps	Inputs	Expected output	Achieved
1	Visual inspection of Wi-Fi router and board connection.	No visual damage to router and board is connected as desired.	
2	Wi-Fi router can be powered	Router power lights turn on.	
3	Wi-Fi is connected to Pico computer	Physical connection is working.	
4	Wi-Fi is connected to FPGA	Physical connection is working.	
5	Wi-Fi is connected to base Computer	Physical connection is working.	
6	PICO test signal to Wi-Fi	Received signal	
7	FPGA test signal to Wi-Fi	Received signal	
8	Base Computer test signal to Wi-Fi	Received signal	
9	PICO to FPGA signal sent	Connection Worked	
10	FPGA to Base Computer signal sent	Connection Worked	
11	PICO to Base Computer signal sent	Connection Worked	

12	Range test of Wi-Fi by moving the hub away from the base computer until connection is lost.	Record the distance achieved.	

Table 24 Wi-Fi Test

Testing the Microphone

Steps	Inputs	Expected output	Achieved
1	Visual inspection of Microphone.	No visual damage to microphone and board is connected as desired.	
2	Microphone can be powered	Power light on Microphone turns on.	
3	Microphone is connected to FPGA.	Connection works and sound can be recorded.	
4	Microphone is connected to FPGA and then to Base computer	Connection working and sound is output on base computer.	

Table 25 Microphone Test

Testing the Sound System

Steps	Inputs	Expected output	Achieved
1	Visual inspection of Speaker.	No visual damage to speakers and board is connected as desired.	
2	Speaker can be powered.	Power light on Speakers turns on.	
3	Speaker is connected to FPGA	Connection works and sound can be produced from the speaker.	
4	Speaker is connected to FPGA then to Base computer	Connection working and sound can be produced from speakers.	

Table 26 sound system Test

15.3 Robot system Test and verification.

Test Checking connections.

Steps	Inputs	Expected output	Achieved
1	Power Robot up	All power lights come on	
2	Send test signal to FPGA	Correct return signal value.	
3	Send test signal to Pico computer	Correct return signal value.	
4	Send test signal for Motor Control Check	Correct return signal value.	
5	Send test signal for encoder	Correct return signal value.	
6	Send test signal for sensors Check	Correct return signal value.	
7	Send test signal for Battery Check	Correct return signal value.	
8	Send test signal for Camera Check	Correct return signal value.	
9	Send test signal for Lidar Check	Correct return signal value.	
10	Send test signal for IMU Check	Correct return signal value.	
11	Send test Signal for Sound Check	Correct return signal value.	
12	Power Robot down	All power lights turn off	

Table 27 Connection Test

Motor test movements.

Steps	Inputs	Expected output	Achieved
1	Power Robot up	Power lights come on.	
2	Send test signal for Motor Control Check.	Correct return signal value.	
3	Left motor 25%, Right motor 25%	Movement of both tracks forward, both tracks at same speed.	
4	Left motor -25%, Right motor -25%	Movement of both tracks backwards, both tracks at same speed.	
5	Left motor 75%, Right motor 75%	Movement of both tracks forward, both tracks at same speed, faster than step 3.	
6	Left motor -75%, Right motor -75%	Movement of both tracks backwards, both tracks at same speed, faster than step 4	
7	Send forward movement Requirement at 100% Reverse	Movement of both tracks forward, both tracks at same speed, faster than step 5.	
8	Left motor -100%, Right motor -100%	Movement of both tracks backwards, both tracks at same speed, faster than step 6.	
9	Left motor 75%, Right motor 0%	Robot turns clockwise.	
10	Left motor 0%, Right motor 75%	Robot turns anticlockwise.	
11	Left motor 100%, Right motor -100%	Robot rotates clockwise on spot.	

12	Left motor -100%, Right motor 100%	Robot rotates anticlockwise on spot.	
13	Power Robot down	All power lights turn off	

Table 28 Main Motor Test

Test - Movement of flippers

Steps	Inputs	Expected output	Achieved
1	Power Robot up	All power light come on	
2	Send test signal for Motor Control Check	Return of correct signal value	
3	Front flippers up for 1 second	Movement of front flippers up	
4	Back flippers up for 1 second	Movement of front flippers up	
5	Front flipper down 1 second	Front flipper returns to start position, encoder gives same value as start of step 3.	
6	Back flipper down 1 second	Front flipper returns to start position, encoder gives same value as start of step 3.	
7	Both flipper up 1 second	Movement of both flippers up	
8	Both flipper down for 1 second	Both flippers returns to start position, encoder gives same value as start of step 7.	
9	Front flipper down until body is raised, then returned to starting position after 5 seconds.	Front of robot is raised up and then returned to start position. All movement mapped by encoders.	

10	Back flipper down until body is raised, then returned to starting position after 5 seconds.	Back of robot is raised up and then returned to start position. All movement mapped by encoders.	
11	Both flippers down until body is raised, then returned to starting position after 5 seconds.	Whole of robot is raised up and then returned to start position. All movement mapped by encoders.	
12	Power Robot down	All power lights turn off	

Table 29 Flippers Test

Test - Robotic Arm Movement.

Steps	**Inputs**	**Expected output**	**Achieved**
1	Power Robot up	All power lights come on	
2	Send test signal for Motor Control Check	Return of correct signal value	
3	Movement of rotating base through 360 degrees and then back to start position.	Arm rotates through full range and returns to original position.	
4	Movement of base joint from horizontal through 180 degrees and back to start position.	Arm can be moved through full 180 degrees of motion and returns to start position.	
5	Movement of elbow joint through 180 degrees and back to start position.	Elbow can be moved through full 180 degrees of motion and returns to start position.	
6	Rotation of head joint through 360 degrees and back to start position.	Head rotates through full 360 degrees of motion and returns to start position.	

7	Tipping head forward 90 degrees, backwards 180 degrees and then return to start position.	Head can be moved through full range and returns to original position.	
8	Open and close input to end effector.	Gripper closes and opens as required.	
9	Power Robot down	All power lights turn off	

Table 30 Arm Movement Test

Test – Recording movement

Steps	Inputs	Expected output	Achieved
1	Power Robot up	All power lights come on	
2	Send test signal for Motor Control Check	Return of correct signal value	
3	Turn on movement recording	Light showing the movement is being recorded.	
4	Start basic movement set, flippers and arm movements.	Basic movement is carried out as requested.	
5	Save data in excel format.	Check correct data has been recorded through time.	
6	Power robot down	All power lights turn off	

Table 31 Recording Test

Test – Reading recorded movement

Steps	Inputs	Expected output	Achieved
1	Power Robot up	All power lights come on	
2	Send test signal for Motor Control Check	Return of correct signal value	
3	Turn on Read movement recording of previously performed motions.	Light showing and robot performs requested movements.	
6	Power robot down	All power lights turn off	

Table 32 Reading Recording test

Testing - FPGA sensors

Steps	Inputs	Expected output	Achieved
1	Power Robot up	All power lights come on	
2	Send test signal to FPGA	Return of correct signal value	
3	Send test signal from sensors.	Return of correct signal value	
4	Test signal sent from FPGA to base computer.	Output values are displayed on base computer.	
5	Record values for 1 minute	List of output values produced across 1 minute.	
6	Test temperature sensor using hand to vary temperature.	List of values giving temperature at particular times.	
7	Test CO_2 sensor by breathing on it and measuring with time.	List of values giving a varying CO_2 value with time, correlating to breathing times.	
8	Output from internal temperature sensor to while robot is stationary and moving.	List of values giving variation of temperature with time to show difference in working conditions and stationary.	

9	Power Robot down	All power lights turn off.	
10	Analyse graphs of data produced.	Give an idea of any potential issues with any of the sensors.	

Table 33 FPGA sensors Test

Test – Pico computer sensors

Steps	Inputs	Expected output	Achieved
1	Power Robot up	All power lights come on	
2	Send test signal to PICO	Return of correct signal value	
3	Send test signal for Camera Check	Return of correct signal value	
4	Send test signal for Lidar Check	Return of correct signal value	
5	Send test signal for IMU Check	Return of correct signal value	
6	Turn on Camera	Video feed displayed on base computer.	
7	Turn on Lidar	Visual feed displayed on base computer.	
8	Turn on IMU	Display on base computer, check data produced to ensure it is correct.	
9	Export Lidar and IMU data to excel.	Data file with outputs over time.	
10	Power Robot down	All power lights turn off.	

Table 34 PICO sensors Test

Test – the IMU and check the SLAM recording system

Steps	Inputs	Expected output	Achieved
1	Power Robot up	All power lights come on	
2	Send test signal to PICO	Return of correct signal value	
3	Send test signal for IMU Check	Return of correct signal value	
4	Turn on IMU	IMU data being received.	
5	Turn on SLAM Recoding system.	Check data is being record	
7	Control inputs to the robot.	Robot will start to move.	
8	Save data to Excel	Data file is produced with output to time.	
9	Power Robot down	All power lights turn off.	
10	Look at the recorded data	Check data corresponds to reality.	

Table 35 IMU and SLAM Test

Test – Lidar System and outputs.

Steps	Inputs	Expected output	Achieved
1	Power Robot up	All power lights come on	
2	Send test signal to Pico computer	Return of correct signal value	
3	Send test signal for Lidar	Return of correct signal value	
4	Turn On Lidar	Lidar data being received.	
5	Movement inputs to robot along test course.	Lidar output displayed on base computer, data logged.	
6	Save data to Excel	Data file is produced with output to time.	
7	Power Robot down	All power lights turn off.	

8	Look at the record data	Check data corresponds to reality.	

Table 36 Lidar Test

Test - Sound output

Steps	Inputs	Expected output	Achieved
1	Power Robot up	All power lights come on	
2	Send test signal to FPGA	Return of correct signal value	
3	Turn on speaker	Speaker power light turns on	
4	Send sound input to speaker	Sound output from speaker.	
5	Power Robot down	All power lights turn off.	

Table 37 Sound Output Test

Test - Microphones

Steps	Inputs	Expected output	Achieved
1	Power Robot up	All power lights come on	
2	Send test signal to FPGA	Return of correct signal value	
3	Turn on Microphones	Speaker power light turns on	
4	Sound input to microphone, speech test signal.	Sound is being played back through base computer.	
5	Save soundwave data to Excel	Data file is produced with output to time.	
6	Power Robot down	All power lights turn off.	

Table 38 Microphones Test

15.4 Testing for Competition

These are high level test to ensure that the robot meets the RoboCup competition requirements.

Testing Mobility

Steps	Inputs	Expected output	Achieved
1	Power Robot up	All power lights come on	
2	Send test signal to all Items in robot	Return of correct signal values	
3	Run the robot over a flat smooth terrain	Successful	
4	Turn on point left and right	Successful through 360 degrees in both directions.	
5	Run the robot over carpet	Successful	
6	Run the robot over gravel	Successful	
7	Go up flight of stairs	Successful	
8	Go down flight of stairs	Successful	
9	Power robot down	All power lights turn off.	

Table 39 Mobility Test

Testing Sensing

Steps	Inputs	Expected output	Achieved
1	Power Robot up	All power lights come on	
2	Send test signal to All Item in robot	Return of correct signal values	
3	Turn on Lidar, Camera, IMU	Display of all items on base computer.	
4	Produce static map of test area	Successful	
5	Test course to produce moving map	Produced successfully from Lidar	

6	Scan a QR Code.	Successful reading of QR code.	
7	Listen to verbal input.	Sound wave produced and audio output from base computer.	
8	Recreate verbal input through speaker.	Sound output from robot speaker.	
9	CO_2 input to sensor.	Successful recording of data.	
10	Power down Robot	All power lights turn off.	

Table 40 Full Sensing Test

Testing Dexterity

Steps	**Inputs**	**Expected output**	**Achieved**
1	Power Robot up	All power lights come on	
2	Send test signal to All Item in robot	Return of correct signal values	
3	Test all movements of arm through full range of motions.	All motions successfully performed.	
4	Open a push door with a robotic arm	Arm can open door.	
5	Open a handled door with a robotic arm.	End effector can move handle and arm can open door.	
6	Pick up a small wooden block and manipulate	Pick up, move and then replace in box	
7	Power down Robot	All power lights turn off.	

Table 41 Dexterity Test

16.0 References

Aalco, n.d. *Aluminium Alloy 6061 T6 Extrusion.* [Online]
Available at: : http://www.aalco.co.uk/datasheets/Aluminium-Alloy-6061-T6-Extrusions_145.ashx
[Accessed 2 February 2018].

Abdelrahman R., Mustafa A., and Osman A. *A comparison between ieee 802.11a, b, g, n and ac standards.* 17-5 pp. 26–29, s.l. : IOSR Journal of Computer Engineering (IOSR-JCSE), 2015.

Anon., n.d. *Carbon Fibre Fasteners Image.* [Online]
Available at: https://system.eu2.netsuite.com/core/media/media.nl?id=99662&c=3937524&h=bd8b956bcf184c80c227 [Accessed 9th February 2018].

Axis Communications AB. AXIS M1054 Network Camera Data Sheet. [Online] 2014. [Cited: 01 02 2018.] https://www.axis.com/files/datasheet/ds_m1054_1480593_en_1608.pdf.

B. Owens, "Rechargeable lithium polymer electrolyte batteries - IEEE Conference

Publication";, Ieeexplore.ieee.org, 1992. [Online]. Available:

http://ieeexplore.ieee.org/document/282028/. [Accessed: 28- Jan- 2018].

F., Colas. xsens_driver. [Online] 2016. [Cited: 01 02 2018.] http://wiki.ros.org/xsens_driver.

Digilent, Nexys4 DDR™ FPGA Board Reference Manual, 3rd ed. Pullman: Digilent, 2016.

R., Gariepy. axis_camera. [Online] 2015. [Cited: 01 02 2018.] http://wiki.ros.org/axis_camera.

Google LLC. Recommended upload encoding settings. Video codec: H.264. [Online] 2018. [Cited: 01 02 2018.] https://support.google.com/youtube/answer/1722171?hl=en-GB.

Hokuyo Automatic co. LTD. Scanning Laser Range Finder UTM-30LX/LN Specification. [Online] 2012. [Cited: 01 02 2018.] https://www.robotshop.com/media/files/pdf/hok-06-sepcs.pdf.

D., Keller. UNDERSTANDING AUDIO DATA COMPRESSION. [Online] 2012. [Cited: 01 02 2018.] https://www.uaudio.com/blog/understanding-audio-data-compression/.

Kohlbrecher S. hector_mapping. [Online] 2016. [Cited: 01 02 2018.] http://wiki.ros.org/hector_mapping.

Maxon Motors. a, n.d. *Planetary Gearhead GP 52 C Specifications.* [Online]
Available at:
https://www.maxonmotor.com/maxon/view/product/gear/planetary/gp52/223111
[Accessed 30th January 2018].

Matweb, n.d. *Carbon Fibre Material Properties.* [Online]
Available at:
http://www.matweb.com/search/datasheet.aspx?matguid=0a2c4758da1a4e45a7b0750924cf3ce2&ckck=1
[Accessed 2 February 2018].

Maxon Motors. b, n.d. *A-max 22 Ø22 mm, Graphite Brushes, 6 Watt, with terminals.* [Online] Available at:
https://www.maxonmotor.co.uk/maxon/view/product/motor/dcmotor/amax/amax22/110167
[Accessed 12 December 2017].

F., Novotny. visp_auto_tracker. [Online] 2016. [Cited: 01 02 2018.] http://wiki.ros.org/visp_auto_tracker.

M., Purvis. robot_upstart. [Online] 2016. [Cited: 01 02 2018.] http://wiki.ros.org/robot_upstart.

RoboteQ, AX3500 - Dual Channel High Power Digital Motor Controller User's Manual.

RoboteQ, 2007.

RS Components, 2018. *RS Pro Steel Alloy Compression Spring, 135mm x 27mm, 1.23N/mm.* [Online]
Available at: https://uk.rs-online.com/web/p/compression-springs/0121292/

Rushford, E., 2017. *ES4A1 Advanced Robotics Lecture resources.* [Online]
Available at:
https://warwick.ac.uk/fac/sci/eng/eso/modules/year4/es4a1/resources/problems_sheet_2.pdf
[Accessed 2018].

Wellington, M., 2013. *How 3D Printing Has Evolved in the Last 10 Years.* [Online] Available at: http://3dprinthq.com/how-3d-printing-has-evolved-in-the-last-10-years/ [Accessed 2 February 2018].

S. Widayat, L. Amifia, A. Cahyadi, O. Wahyunggoro and E. Loniza, "Lithium polymer battery modelling and fault detection design - IEEE Conference Publication", Ieeexplore.ieee.org, 2015.

[Online]. Available: http://ieeexplore.ieee.org/document/7496639/. [Accessed: 28- Jan- 2018].

17.0 Technical Drawings